TECHNISCHE UNIVERSITÄT WIEN

MEDIZINISCHE UNIVERSITÄT WIEN

Diplomarbeit

Stability of dynamic ^{1}H-observed deuterium metabolic imaging in a 3T MR scanner

zur Erlangung des akademischen Grades

Diplom-Ingenieur

im Rahmen des Studiums

Physikalische Energie- und Messtechnik

eingereicht von

Daniel Zeitz, BSc

Matrikelnummer 11701845

ausgeführt am Atominstitut
der Fakultät für Physik der Technischen Universität Wien
in Zusammenarbeit mit dem Hochfeld MR Zentrum, Zentrum für Medizinische Physik und Biomedizinische Technik, Medizinische Universität Wien

Betreuung:
Em.Univ.-Prof. Dipl.-Ing. Dr.techn. Gerald Badurek
Prof. Dipl.-Ing. Wolfgang Bogner, PhD
Priv.-Doz. Dipl.-Ing. Gilbert Hangel, PhD
Mitwirkung:
Ass.Prof. Dipl.-Ing. Dr. Karin Poljanc

Wien, 28.09.2022

Daniel Zeitz

Gerald Badurek

Statuatory Declaration

I herewith declare that I have composed the present thesis myself and without use of any other than the cited sources and aids. Sentences or parts of sentences quoted literally are marked as such; other references with regard to the statement and scope are indicated by full details of the publications concerned. The thesis in the same or similar form has not been submitted to any examination body and has not been published. This thesis was not yet, even in part, used in another examination or as a course performance. Furthermore I declare that the submitted written (bound) copies of the present thesis and the version submitted on a data carrier are consistent with each other in contents.

Place, Date: Signature:

Acknowledgments

Throughout the writing process of this thesis I have been very fortunate to receive a great deal of support, from the colleagues at the Institute, the supervisors at the Technical University and my friends and family. I want to thank all of you who supported me while I was working on this master thesis.

I want to thank my supervisors at the High Field Magnetic Resonance Centre Prof. Wolfgang Bogner and Gilbert Hangel. You were always open for discussions, questions or feedback and your invaluable expertise and experience in the field helped me so much for accomplishing this thesis.

I would also like to thank the other members of the research group at the Institute. It was a pleasure working with you! In particular I want to thank you, Fabian, for patiently bringing me closer to the concepts and methods of MR data reconstruction, and for always taking the time for my questions. I also want to thank you, Dario, for initially arousing my interest in MRSI and introducing me to working with the environment at the Institute.

I would also like to thank you, Prof. Badurek for the kind supervision from the Technical University's side, for the proof reading of the master thesis as well as the project thesis. I also want to thank you, Dr. Poljanc, for assisting with the supervision.

Further, I would like to say thanks to my friends, who were always there for cheering me up and distracting me during not so pleasant, stressful times and when things did not work out as planned.

Lastly a big thank you to my family for the support at home. I could not have done it without you.

Contents

Kurzfassung

Im Rahmen dieser Arbeit wurde die Stabilität einer bildgebenden Magnetresonanzspektroskopie (MRSI) Messsequenz in einem 3T MRT bewertet. Die Relevanz der Stabilität dieser Sequenz kommt von ihrer Anwendung im Rahmen von Deuterium Metabolic Imaging (DMI), einer dynamischen Methode, welche den Glukose Metabolismus im Gehirn lokalisieren und quantifizieren kann. Eine der Grundvoraussetzungen für DMI ist eine hohe zeitliche und räumliche Stabilität, da die Dauer der Messsequenz relativ lange ist.

Die Messungen fanden in einem 3T MRT (Siemens Healthcare) am Hochfeldmagnetresonanzzentrum der Medizinischen Universität Wien statt. Die MRSI Sequenz in Kombination mit räumlicher Kodierung durch konzentrische Ringtrajektorien ermöglicht die 3D Darstellung von Konzentrationen einzelner Stoffwechselprodukte im Gehirn. Dabei wurden die Konzentrationen von NAA+NAAG (tNAA) als Referenzsignal mit konstanter Konzentration in allen Bereichen des Gehirns, sowie Glutamin + Glutamat, zusammengefasst zu Glx, analysiert. Zuerst wurde die Messsequenz an 5 gesunden Probanden mehrmals hintereinander angewandt, wobei die Reproduzierbarkeit der gemessenen Daten mit der Zeit evaluiert werden konnte. Die normale Fluktuation der Messdaten bei einer konstanten Konzentration wurde mithilfe des Variationskoeffizienten quantifiziert. Anschließend wurde für DMI ein deuteriertes Glukosepräparat verabreicht, welches rasch im Gehirn verstoffwechselt wird. Die Deuteriumkerne werden im Verlauf des Glukosestoffwechsels an Glx übertragen, da die chemischen Reaktionen durch die Präsenz von Deuterium nicht beeinflusst werden. Die Deuteriumkerne ersetzen die Wasserstoffkerne in der Glx4-Gruppe, wodurch die Resonanzfrequenz von Glx4 verändert wird. Jedoch kann mit Wasserstoff(^{1}H)-Magnetresonanzspektroskopie (MRS) kein Deuterium (^{2}H) detektiert werden. Da mit der Zeit mehr deuterierte Glukose zu Glx verstoffwechselt wird, wird mit der Zeit das Resonanzsignal der deuterierten Gruppe in Glx, also Glx4, in ^{1}H-MRS schwächer. Diese Abnahme mit der Zeit kann dann mithilfe einer linearen Funktion quantifiziert werden.

In den Referenzmessungen wurde der Variationskoeffizient für Glx4/Glx/tNAA gemittelt über das ganze Volumen bestimmt, und beträgt 4.54/3.92/3.13%. Nach Einnahme des deuterierten Glukose Präparats konnte eine deutliche Abnahme der gemessenen Glx4 Konzentrationen über die Dauer der Messungen beobachtet werden. Die Abnahme gegenüber den Startkonzentrationen ist im Mittel aller Probanden nach einer Stunde 10.13% in WM und 14.18% in GM. Zudem konnte ein simuliertes Laktat Signal quantifiziert und bildgebend dargestellt werden. Dabei wurden sowohl eine konstante, als auch eine abnehmende Laktatkonzentration simuliert. Dies sollte die Fähigkeit der Messsequenz, zwischen oxidativem und nicht-

oxidativem Glukose Stoffwechsel im Gehirn zu unterscheiden, beurteilen. Anhand der Ergebnisse kann man sagen, dass die Stabilität der Sequenz ausreicht, um in 3T für dynamisches DMI implementiert zu werden, da eine klare Abnahme der Glx4 Konzentrationen sowie ein Kontrast zwischen WM und GM erkennbar war.

Abstract

In this thesis, the stability of a magnetic resonance spectroscopic imaging (MRSI) sequence in a 3 Tesla (T) magnetic resonance (MR) scanner was evaluated. The importance of the stability of the MRSI sequence comes from its application in a novel dynamic imaging method using deuterium (^{2}H)-labeled metabolites in hydrogen (^{1}H) magnetic resonance spectroscopy (MRS). Due to long scanning times, one of the main requirements for the implementation of this dynamic method, in particular with field strengths of 3T, is a very high spatial and temporal stability of the underlying MRSI measurement sequence.

The measurements were made at the High Field Magnetic Resonance Centre of the Medical University of Vienna in a 3T MR scanner. An MRSI sequence combined with concentric ring trajectory spatial encoding was used to obtain concentration maps of different metabolites. In a first run, 5 subjects were repeateadly scanned in a measurement session with the same MRSI sequence in order to evaluate its stability. The consistency of the results was mainly quantified with the coefficient of variation (CV). The metabolites, whose concentrations were taken for the analysis, are NAA+NAAG (tNAA) as a constant reference signal and Glutamine (Gln) and Glutamate (Glu) because of their role in the glucose metabolism in the brain. Then, 5 subjects were given a deuterated [6,6'-$^2H_2$]-glucose substrate which was quickly metabolized in the brain. The ^{2}H nuclei in glucose are passed on to the metabolic follow-up products, namely to Gln and Glu which are combined as Glx. While ^{2}H nuclei cannot be detected directly via ^{1}H-MRS, the drop in ^{1}H-MRS detectable signal, when a ^{1}H nucleus in Glx is replaced by a ^{2}H nucleus, can be detected as an indirect measure. The ^{2}H-labeled group in Glx is called Glx4, and its decay was then quantified using a linear fit function.

Assuming constant concentrations in the reference measurements, the CV for Glx4/Glx/tNAA is 4.5/3.9/3.1% averaged over the full volume of interest. After ingestion of the deuterated glucose substrate, a clear decline of Glx4 concentrations was observed in all subjects, with the concentration decrease after an hour being on average 10.13% in White Matter (WM) and 14.18% in Grey Matter (GM). Thus concentration decay of ^{2}H-labeled Glx as well as a contrast between WM and GM was clearly distinguishable throughout the brain. Further, a simulated Lactate signal with constant and with decaying signal strength could be identified. This should probe the MRSI sequences ability of distinguishing between oxidative and non-oxidative glucose metabolism in the brain. Given these results, the stability of the 3D-FID-MRSI sequence is sufficient for the application in dynamic DMI with ^{1}H-MRS in a 3T scanner.

Abbreviations

ATP	Adenosine triphosphate
CV	Coefficient of variation
CRT	Concentric ring trajectory
DMI	Deuterium metabolic imaging
FDG	Fluorodeoxyglucose
FFT	Fast fourier transform
FID	Free induction decay
FLAIR	Fluid-attenuated inversion recovery
FWHM	Full width at half maximum
Glu	Glutamate
Gln	Glutamine
Glx	Glu + Gln
GM	Grey matter
Lac	Lactate
MRI	Magnetic resonance imaging
MRS	Magnetic resonance spectroscopy
MRSI	Magnetic resonance spectroscopic imaging
MUSICAL	Multichannel spectroscopic data combined by matching image calibration data
NAA	N-acetylaspartate
NAAG	N-acetylaspartylglutamate
NMR	Nuclear magnetic resonance
OVS	Outer volume suppression
PET	Positron emission tomography
RF	Radiofrequency
SNR	Signal-to-noise-ratio
SVS	Single voxel spectroscopy
TE	Echo time

tNAA	NAA + NAAG
TR	Repetition time
vNAV	Volume navigator
VOI	Volume of interest
WET	Water suppression enhanced through T1 effects
WM	White matter

Chapter 1

Introduction

Magnetic resonance imaging (MRI) is commonly used in clinical applications to non-invasively represent different types of tissue in the brain. Often combined with other tomographic methods, such as positron emission tomography (PET), to gain further information on metabolic processses, it is used to detect visible anomalies in the tissue caused by various disorders. Magnetic resonance spectroscopy (MRS) is a routinely used diagnostic method based on nuclear magnetic resonance (NMR) which can identify different biochemicals in a small volume of space called a voxel in the tissue.

These chemicals involved in metabolic processes in the brain are called metabolites and peaks in the NMR spectrum can be associated with metabolites as every chemical structure has a characteristic NMR spectrum. By combining the image obtained through MRI with the NMR spectrum at the corresponding location, diagnosis of certain metabolic disorders or diseases can be confirmed, as certain pathological conditions show clear indications in the NMR spectrum[1, 2]. This method is called single-voxel-spectropscopy (SVS) and can give additional information on the biochemical properties of the tissue. However, while SVS offers high spectral resolution, it is limited to a single voxel, i.e. only a small volume in the brain.

An extension of SVS that covers a larger volume of the brain is called multi-voxel-spectroscopy and involves spatial encoding of the signals through magnetic gradients. It is the basic principle of magnetic resonance spectroscopic imaging (MRSI), the method that this thesis is concerned with. Low resolution MRSI is nowadays already used in clinical applications, however high resolution MRSI sequences require ultra-high field (UHF) strengths and thus 7 Tesla (T) magnetic resonance scanners, long scanning times and external processing of the acquired data. As the strength of the signal in NMR is directly linked to the magnetic field strength, data acquired through MRSI sequences in 7T scanners have a higher signal-to-noise-ratio (SNR) and

thus inherently higher spatial and spectral resolution than 3T scanners, but 7T scanners are not as commonly found in clinics.

Optimized signal acquisition patterns vastly reduce the necessary scanning time, which allows the sequence to acquire signals with a higher spectral bandwidth that in turn leads to a higher spectral resolution, compensating the lack of UHF. The higher the spectral bandwidth of the signal, i.e. the more data points are used to describe an NMR spectrum, the more individual peaks can be distinguished in the spectrum. UHF allow for more dispersion between resonance peaks, thus revealing smaller multiplet signals, which are not visible in NMR spectra acquired in a lower magnetic field as resonance signals close to each other would merge to a broader peak. This is a problem that we encounter especially for metabolites such as Glutamine (Gln), Glutamate (Glu), or Lactate(Lac), that are strongly affected by a phenomenon called J-coupling which leads to their resonance signal splitting up in multiplets. Nuclei in a molecule with different magnetic moments share electrons in chemical bonds. This interaction is called scalar coupling or J-coupling. As electrons have a non-zero spin, the Pauli principle forbids certain spin-states for electrons in the chemical bonds, which results in energetically different nucleus-electron spin state combinations with corresponding resonance frequencies which are independent of the external magnetic field and on the order of magnitude of a few Hz. The proton resonance frequency is 300 MHz in a 7T field, the multiplet signals induced through J-coupling are thus very close to each other as they are just a few Hz apart. As a consequence, an increased amount of data points and a high spectral bandwidth are required to achieve a sufficiently high spectral resolution for the detection of these J-coupled metabolites in an NMR spectrum acquired in 3T magnetic fields.

The consistent detection of these metabolites in the NMR spectrum is highly important as they are all products of the metabolic cycle of glucose. Anomalies in the glucose metabolism in the brain are a key indicator for a brain tumor, because one of the characteristics of tumor tissue is a highly increased glucose uptake as well as the metabolism of glucose into lactate. After ingestion of a deuterated glucose substrate, a method based on MRSI can be used to label and track deuterated glucose molecules as well as their metabolic follow-up products in ^{1}H-MRS. The use of a 3D-FID-MRSI sequence in 3T ^{1}H-MRS for imaging of deuterium-labeled metabolites was mentioned in a previous study[3]. For simplicity, the method will be referred to as deuterium metabolic imaging (DMI), even though it does not use ^{2}H-MRS to acquire resonance signals from deuterium nuclei like in previous studies[4] but instead tracks deuterated signals indirectly in ^{1}H-MRS.

The importance of the stability of the underlying MRSI sequence comes from the key requirement for dynamic methods, which is a very high spatial and temporal stability as the measurement sequence has to be repeateadly used. This method could already successfully locate and identify metabolic processes in 7T but as 3T scanners are more widely available, dynamic MRSI methods implemented in 3T scanners can potentially increase their application in clinical studies. The goal of this thesis is to show that the dynamic DMI method using ^{1}H-MRS in 3T can consistently quantify and visualize metabolite concentrations, to produce high resolution maps that can be used to locate and identify metabolic anomalies in the brain.

Chapter 2

Theoretical Background

2.1 Nuclear magnetic resonance spectroscopy

2.1.1 Nuclear magnetic resonance

The physical phenomenon behind MRS is called nuclear magnetic resonance and will be described in the following section. Since we are working with Hydrogen spectroscopy we will only consider protons but the following principles also describe the behaviour of neutrons and nuclei composed of protons and neutrons such as Deuterium. Any charged particle with non-zero angular momentum (intrinsic or orbital) has a magnetic dipole moment $\vec{\mu}$

$$\vec{\mu} = \frac{g\mu_N}{\hbar}\vec{I} = \gamma\vec{I} \tag{2.1}$$

that is related to the angular momentum $\vec{I}$ through the gyromagnetic ratio $\gamma = \frac{g\mu_N}{\hbar}$. The g-factor g is a proportionality constant relating the magnetic moment with the angular momentum of a nucleon and depends on its inner structure. It is thus different for protons and neutrons, as they are not elementary particles but represent bound states of three quarks carrying either +2/3 ('up'-quark) or -1/3 ('down'-quark) elementary electric charge e. The nuclear magneton $\mu_N = \frac{e\hbar}{2m_p}$ with the elementary charge e and the proton mass m_p, is the natural unit for the magnetic dipole moment of a nucleon. The gyromagnetic ratio of the proton is $\gamma_p = 2.675 \times 10^8 \frac{rad}{Ts}$ [5].

In an external magnetic field $\vec{B}$ applied along the z-axis, the magnetic moment $\vec{\mu}$, inducing itself a local magnetic field, will start interacting with $\vec{B}$ and feel a torque which is described by

$$\frac{d\vec{\mu}}{dt} = \vec{\mu} \times \gamma\vec{B}. \tag{2.2}$$

The solution of (2.2) shows that the magnetic moment $\vec{\mu}$ and thus the proton will start precessing around the axis of $\vec{B}$ in a phenomenon called Larmor precession. The angular precession frequency is referred to as the Larmor frequency and is defined as

$$\omega_0 = \gamma|\vec{B}|. \tag{2.3}$$

We find that at 3T the resonance frequency of the proton is 127.74 MHz, which is in the radiofrequency range.

For a proton in $\vec{B}$, the magnetic moment $\vec{\mu}$ in direction of the magnetic field axis, μ_z, is quantized because the angular momentum $\vec{I}$ can only have certain discrete values along the z-axis, namely $I_z = m_z\hbar$ with m_z being the magnetic (or orientation) quantum number. Since (2.1) relates I_z with μ_z and the potential energy of a magnetic moment in a magnetic field is $E = -\vec{\mu} \cdot \vec{B}$, the discrete energy levels for a magnetic moment in $\vec{B}$ become

$$E_{m_z} = -\mu_z B_z = -\gamma I_z B_z = -\gamma m_z \hbar B_z. \tag{2.4}$$

Since m_z can only take integer values, the energy levels of a nucleon split up in an external magnetic field with the difference between two neighbouring energy states being

$$\Delta E = \gamma\hbar B. \tag{2.5}$$

This splitting up of energy states in an external field is called the Zeeman effect. For a proton, the transition between two energy states is possible when the nearby electromagnetic field has a frequency corresponding to the protons resonance frequency, i.e. its Larmor frequency (2.3). This changes periodically the orientation of the magnetic moment and thus the induced magnetic field around the proton, which in turn induces a measurable current in a receiver coil. The quantization of the magnetic moment along the z-axis depends on multiple factors, however also in the ground state where the orbital angular momentum is zero, the non-zero spin angular momentum of a proton with spin s = 1/2 will still cause an energy level splitting into spin-up and spin-down states. This was verified by the Stern-Gerlach-Experiment in 1922. Henry Purcell and Felix Bloch independently of each other experimentally demonstrated this phenomenon, called nuclear magnetic resonance (NMR), in 1945 by measuring the change of the induced current in a receiver coil after excitation of a nucleus. For their discovery and their advancements they were awarded jointly the Nobel prize in physics in 1952.

Bloch equations

In the brain, matter in a $1\times1\times1$ mm^3 volume contains around 6×10^{19} protons[1]. The sum of all the spins of all the protons will be combined to yield a macroscopic magnetization

$$\vec{M} = \sum_i \vec{\mu_i}. \tag{2.6}$$

In a magnetic field

$$B(\vec{t}) = \begin{pmatrix} B_1 \cos(\omega t) \\ B_1 \sin(\omega t) \\ B_0 \end{pmatrix}, \tag{2.7}$$

the magnetization $\vec{M}$ will experience a torque described by

$$\frac{d\vec{M(t)}}{dt} = \vec{M(t)} \times \gamma \vec{B(t)}. \tag{2.8}$$

This system of equations is similar to (2.2) with the magnetic moment $\vec{\mu}$ replaced by the magnetization vector $\vec{M}$. This torque induces a complicated spiral trajectory of $\vec{M}$ in the stationary frame of reference which is why solving the coupled differential equations (2.8) is easier after a change of reference frame into a (rotating) laboratory frame in phase with $\vec{B_1}$, as it reduces (2.8) to a static problem. The equations solving (2.8) are called the Bloch equations (2.9)-(2.11) and describe the behaviour of the magnetization sphere $\vec{M}(M_x, M_y, M_z)$ of a large number of spins with relaxation times T_1 and T_2 and an equilibrium magnetization M_0 under the influence of a magnetic field $\vec{B}(B_x, B_y, B_z)$ in a static homogeneous magnetic field in z-direction, B_0:

$$\frac{M_x(t)}{dt} = \gamma(\vec{M}(t) \times \vec{B}(t))_x - \frac{M_x(t)}{T_2}, \tag{2.9}$$

$$\frac{M_y(t)}{dt} = \gamma(\vec{M}(t) \times \vec{B}(t))_y - \frac{M_y(t)}{T_2}, \tag{2.10}$$

$$\frac{M_z(t)}{dt} = \gamma(\vec{M}(t) \times \vec{B}(t))_z - \frac{M_z(t) - M_0}{T_1}. \tag{2.11}$$

These equations were first postulated by Felix Bloch in 1946 and include the effects of spin-spin relaxation, characterised by T_2, and spin-lattice relaxation, characterised by T_1. The two relaxation effects as well as the FID will be explained in the next sections.

Longitudinal relaxation

Without the presence of an external field, the proton spins are randomly orientated in all spatial directions and do not induce a measurable magnetization, as oppositely faced magnetic moments cancel each other out.

An external magnetic field B_0 applied in the z-direction, i.e. $\vec{B} = \begin{pmatrix} 0 \\ 0 \\ B_0 \end{pmatrix}$, will cause a precession of the magnetic moments $\vec{\mu}$ and thus of the magnetization $\vec{M}$ with the Larmor frequency around the axis of B_0. As the potential energy of a magnetic moment $\vec{\mu}$ in a magnetic field B_0 is minimal when $\vec{\mu}$ and B_0 are oriented parallel to each other, the spins will slightly favor the parallel orientation to the axis of B_0 as it is the energetically favorable orientation. Since the spins will be biased towards an orientation along B_0, they give rise to a small magnetization in the direction of B_0 that increases over time according to

$$M_z(t) = M_0(1 - e^{-\frac{t}{T1}}), \tag{2.12}$$

with T_1 being the longitudinal relaxation time. This process of building up magnetization in the direction of B_0 is called spin-lattice relaxation, since energy is transferred from the proton spins to the surrounding lattice in order to reach thermodynamic equilibrium. As the protons tend towards the state of thermodynamic equilibrium, the induced magnetization tends towards M_0, which is the thermodynamic equilibrium magnetization, given by

$$M_0 = \frac{N\gamma_p^2\hbar^2 B_0}{4k_B T}, \tag{2.13}$$

where N is the number of protons, $k_B = 1.38 \times 10^{-23}$ is the Boltzmann constant [5], and T is the absolute temperature in Kelvin[1].

The magnetization M_z defines the strength of the resonance signal that will be measured in an NMR experiment. The thermodynamic equilibrium magnetization M_0 is relatively small and not directly detectable while in the direction of B_0. Hence it will be necessary to rotate the magnetization $\vec{M}$ into the transversal plane. The magnetization M_z building up over time is sketched in Fig. 2.1 on the right.

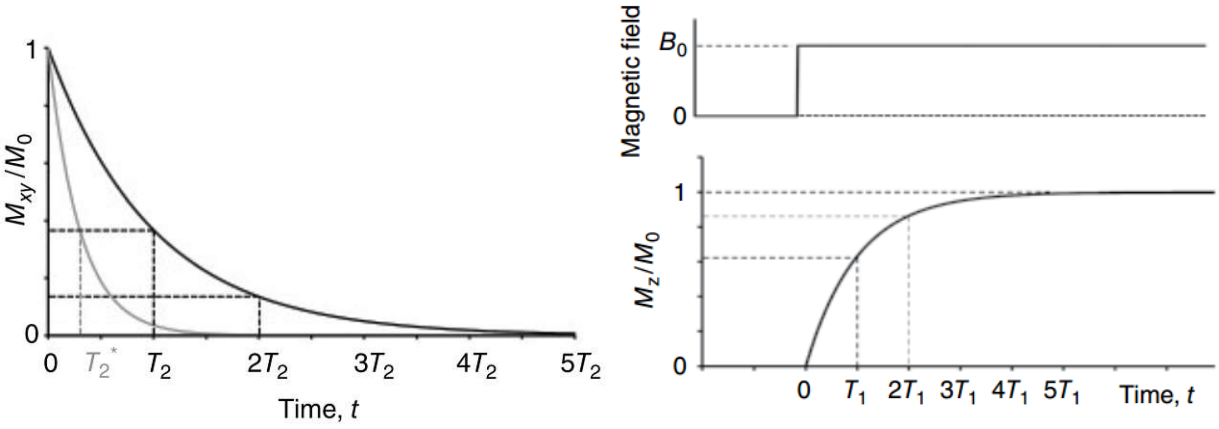

Figure 2.1: Left: T_2 (black) vs T_2^* (grey) decay after excitation in the transversal plane. Right: Magnetization M_z built up through spin-lattice relaxation after the external magnetic field B_0 is turned on[1].

Transversal relaxation

A high frequency external magnetic field $\vec{B_1}$ with a frequency matching the Larmor frequency of the protons solving (2.9)-(2.11), can temporarily deflect the entire magnetization sphere from the z-direction into the transversal plane by an angle α which is called the flip angle, by adding a small torque at every Larmor rotation. The flip angle depends on the magnetic field strength B_1 as well as the duration of the RF pulse Δt and is given by :

$$\alpha = \gamma B_1 \Delta t \tag{2.14}$$

As the Larmor frequency of the proton is in the range of radiofrequencies, $\vec{B_1}$ is called a radiofrequency (RF) pulse.

After the RF pulse, the magnetization in the transversal plane $M_{xy}(0)$ will be non-zero and thus detectable, as all the spins that were in phase in z-direction will be in phase in the transversal plane, while the rest of the spins in the magnetization sphere are still randomly distributed. Random energetic exchanges between nearby spins through molecular tumbling and Brownian motion will cause the spins to dephase after a short time, causing a loss of macroscopic magnetization in the transversal plane. This decay of magnetization is called the spin-spin relaxation and is described by

$$M_{xy} = M_{xy}(0) e^{\frac{-t}{T_2}}, \tag{2.15}$$

with T_2 being the transversal relaxation time, which is a lot shorter (10 - 300 ms) than T_1 (500

- 3000 ms).

As these interactions between spins are random and happen independently of the local magnetic field, spin-spin relaxation can be described by an exponential decay. However, in real matter there are also inevitable local inhomogeneities in the magnetic field, especially in the region of the frontal cortex as well as in the border region of the skull. This is due to the different magnetic susceptibilities of water in the brain and air in the nasal cavity.

Depending on their location in space, spins will not have the same Larmor frequency which causes an additional loss of phase coherence. The additional decay caused by these temporarily constant inhomogeneities is not exponential as it is not random but position dependent and leads to stronger dephasing at certain points than at others. Both effects are combined in literature through another relaxation constant T_2^*, which describes the actual measured decay of magnetization of matter after an excitation in the transversal plane. The voltage induced by this decaying magnetization in the receiver coil is called the free induction decay (FID). Both T_2 and T_2^* decay can be seen in Fig. 2.1 on the left.

2.1.2 Magnetic Resonance Spectroscopy

After technical advancements during the 1950's, allowing for the use of pulsed high frequency magnetic fields $\vec{B}_1$, it was possible to actually measure the FID of the nuclei. The molecules in the brain are complex chemical structures, where same hydrogen atoms have different resonance frequencies depending on the group they're in. This is due to the chemical shift

$$\delta = \frac{\nu - \nu_{ref}}{\nu}, \tag{2.16}$$

which was discovered in 1950 by W.G.Proctor and F.C.Yu. Neighboring atoms can shield the whole group by locally inducing a permanent magnetic field, which means that the local environment of a nucleus can influence its resonance frequency. Different chemical groups shift the resonance peaks in a spectrum with respect to a reference nucleus such as ^1H with a Larmor frequency ν_{ref}. Thus each chemical structure has a characteristic resonance spectrum, as the ^1H nuclei in each group have different resonance frequencies.

This spectrum can be obtained by measuring the FID and applying a Fourier transform to the signal, which splits up the time-dependent signal into the resonance frequencies of the chemical groups that contribute to the signal. This principle is called magnetic resonance spectroscopy (MRS) and allowed for the distinction of different groups in a molecule and for the

identification of a certain molecule in a spectrum measured in real matter. Through MRS, we can identify the chemical components that are responsible for a certain FID signal. It took about 20 more years to develop another method called Magnetic Resonance Imaging (MRI) allowing for the localization of the signal.

2.1.3 J-coupling

There is another effect that causes resonance peaks to split into several smaller resonance peaks which is due to the interaction of nearby nuclei with each other through electrons in their chemical bonds. This splitting up of resonance peaks is called J-coupling or scalar coupling and is independent of the magnetic field, thus it is given in Hz. This is an effect that can only be explained through quantum mechanics, as it involves the spin of the involved particles. Isolated atoms, nuclear spin and their surrounding electrons spin will always choose the energetically favorable antiparallel orientation as they have the freedom to choose the energetically lowest state. In chemical bonds however, because of the Pauli exclusion principles that does not allow two identical quantum states in the same place, the electrons with spin $s = 1/2$ will be forced into an antiparallel orientation. The nucleus can be in any state and as the electron's spins are locked in a certain orientation, a nuclear spin and its electrons spin can thus be in a energetically higher parallel orientation or in an energetically lower antiparallel orientation, depending on the state of the nucleus. Thus there are two possible states for the atom with different resonance frequencies. The more nuclei are involved, the more states will be allowed and thus resonances can be split up into more smaller resonances. Scalar coupling is independent from the external magnetic field and is given in Hz. A more detailed description of J-coupling can be found in [1].

2.2 Magnetic Resonance Imaging

Based on MRS, P. Mansfield and P.C. Lauterbur developed MRI during the 70's, for which they received the shared Nobel Prize in physiology and medicine in 2003. The idea of MRI is the encoding of measured FID signals with spatial information. The data acquisition takes place after a series of magnetic gradient fields in combination with RF pulses prepare and encode the FID.

2.2.1 Main components of the MR scanner

The most important and most expensive part of the MR scanner is the superconducting magnet that is wound around the scanner tube and can produce a magnetic field of multiple T. It is the largest and outermost part of the MR scanner. Between this superconducting magnet inducing the magnetic field B_0 and the patients table are multiple coils required for the measurement sequence. The high frequency RF pulses or B_1 fields are generated by the RF coils. The shimming coils are required for the generation of additional magnetic fields that homogenize the magnetic field B_0 in the VOI. The gradient coils induce the magnetic field gradients that are required for the localisation of the signal for imaging.

Shimming

The scanner field B_0 is locally inherently inhomogeneous as it interacts with the local field of the matter in the brain, so it is difficult to precisely locate the signals as local variations in the magnetic field will deviate the phase and frequency encoded location of the signal from its actual position. Even small deviations of the magnetic field can cause unwanted shifts in the resonance frequency.

A standard procedure to counteract this problem during the measurement sequence and to homogenize the field in the brain is 'shimming', where coils create magnetic fields, that can be approximated in the VOI using spherical harmonics, which, overlayed with the scanner field B_0, reduces the inherent inhomogeneities of the latter. This is a process that can be done automatically by programs pre-installed by the manufacturer or manually.

2.2.2 Encoding of spatial information in the signal

A magnetic field gradient G in any spatial direction, which is sketched in Fig. 2.2, will shift the resonance frequency ν of a nucleus depending on its location r according to

$$\nu(r) = \frac{\gamma}{2\pi} B_0 + \frac{\gamma}{2\pi} rG \tag{2.17}$$

and in the NMR spectrum, the chemical shift of the groups will depend on the strength of the magnetic field at its location, which is $B(r) = B_0 + rG$. The NMR spectra of the molecules present in the brain are characteristic, so from the measured spectrum with the applied gradient we can deduce how strong the gradient affects the signal and thus the position of the nuclei responsible for the signal in the gradient direction.

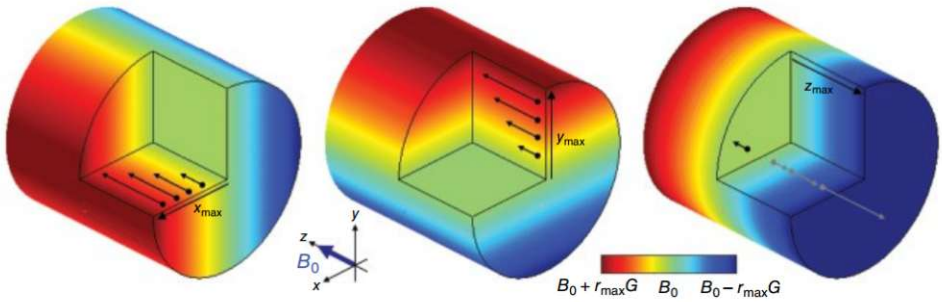

Figure 2.2: Applied magnetic field gradients G_x, G_y and G_z inside of the scanner tube [1].

In practice the three spatial dimensions x,y,z are encoded through frequency-encoding, phase-encoding and slice selection respectively.

Slice selection

A magnetic field gradient in the z-direction will shift the resonance frequency ν of the nuclei according to their position on the z-axis. An RF pulse with a specific frequency ν_{RF} will only excite the nuclei that have a matching resonance frequency. By combining an RF pulse with a magnetic field gradient, a slice can be selected in which all nuclei with a Larmor frequency within the bandwidth of the RF pulse will be excited while everything else on the z-axis will not be influenced by the RF pulse. This principle can be seen in Fig. 2.3.

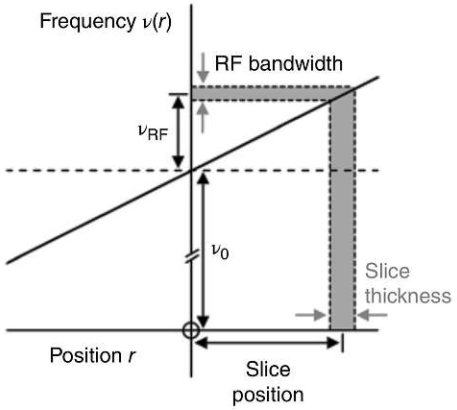

Figure 2.3: Principle of slice selection in the brain. The height of the slice is selected by the gradient strength and the frequency of the RF pulse and the width of the slice is determined by the bandwidth of the RF pulse[1].

After excitation, the measured signal can be identified with a location on the z-axis and thus to a slice of the brain. Exciting a single slice leaves two more spatial dimensions in the

transversal plane that have to be encoded in the signal. This 2D spatial information will be encoded in the frequency and in the phase of the signal.

Frequency encoding

A magnetic field gradient in the x direction will shift the resonance frequency of the nuclei depending on their position in the x direction according to (2.17). After excitation of the nuclei, the frequency encoding gradient is turned on which causes the FID to be position dependent. Subsequently measuring the FID, for instance through a spin echo, allows us to distinguish the signals based on their position on the x-axis. As the spectrum is obtained through a Fourier transform, the resonance frequency shift caused by the gradient will be transferred to the spectrum.

Phase encoding

The information on the last spatial dimension y will be stored through phase encoding. The location on the y axis is encoded in the phase of the signal with another magnetic gradient in the y axis, applied right after excitation and turned off before acquisition. Unlike for frequency encoding gradients, there is no additional, opposite gradient, so the induced phase shift can be measured in the acquired signal. This phase encoding gradient is linearly incremented for each measurement and will induce a phase shift for all the nuclei depending on their position in the gradient field. Every time the gradient strength increases, the nuclei will have a slightly different phase shift. By comparing how this phase shift varies for each signal in each measurement, the position of the signal on the y axis can be deduced.

2.2.3 FID signal acquisition

The FID of the magnetization sphere is an analog sinusoidal signal with a frequency $\Delta\nu$ that is induced in a receiver coil. The FID is governed by the $T2^*$-decay which includes spin-spin and spin-lattice relaxation. While the effect of spin-lattice relaxation is irreversible as energy will spread into the thermodynamic system, spin-spin relaxation is reversible and can be undone by forming an echo. This FID signal is sampled by an analog-to-digital converter measuring the current at equidistant time points at least twice per period $\Delta T = \frac{1}{\Delta\nu}$. The time between two data points Δt corresponds to the inverse of the spectral bandwidth. The sampling of the FID signal is sketched in Fig. 2.4.

Applying a Fourier transform to this digitized signal results in a spectrum with a peak at every resonance frequency contributing to the signal. During the acquisition window, only

the spins that are in phase will lead to a measurable signal. While the spins are in phase right after excitation, it is technically not possible to instantly turn on the magnetic fields and thus sampling of the first data points would happen during time-varying magnetic fields, which would result in unwanted artifacts in the spectrum as there would be no consistent spatial encoding of the spectrum. Excluding these data points while the gradients ramp up, would result in a loss of data with the highest SNR. Further, prior to acquiring the data, it has to be encoded with the spatial information, which requires magnetic field gradients applied during the FID.

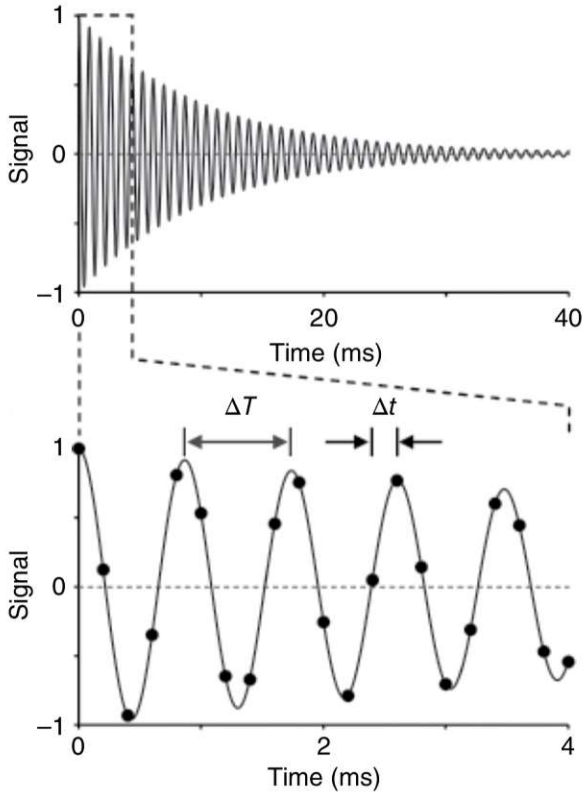

Figure 2.4: FID sampling at equidistant time points by the ADC. The sampling frequency Δt has to be at least twice as high as the period of the signal ΔT in order accurately sample the FID[1].

2.2.4 Spin-echo sequence

An effect that is then used to acquire the FID signal is a spin echo. By applying an RF pulse orientated anti-parallel to B_0 after the excitation pulse, the additional dephasing caused by the local magnetic field inhomogeneities can be reversed, bringing back the signal in the form of an echo, that is slightly weaker than at $t = 0$, which is due to the T_2 decay as can be seen in Fig. 2.1 on the left. Locally the magnetic field has maxima where spins dephase more rapidly. By

flipping the orientation of the spins with a refocusing RF pulse anti-parallel to $\vec{B_0}$ that is turned on for twice as long as the first excitation pulse, the effect of these local inhomogeneities can be undone. At local magnetic field maxima, where the spins experience the strongest dephasing, they will also rephase more rapidly after the refocusing pulse as the static inhomogeneities in the field will then have an inverse effect on the rephasing speed of the spins. After an echo time $t = T_E$ the spins will all be in phase again giving rise to a macrosopic magnentization called an echo, which is when the FID signal is acquired in the receiver coil. This effect can be seen in Fig. 2.5 on the left.

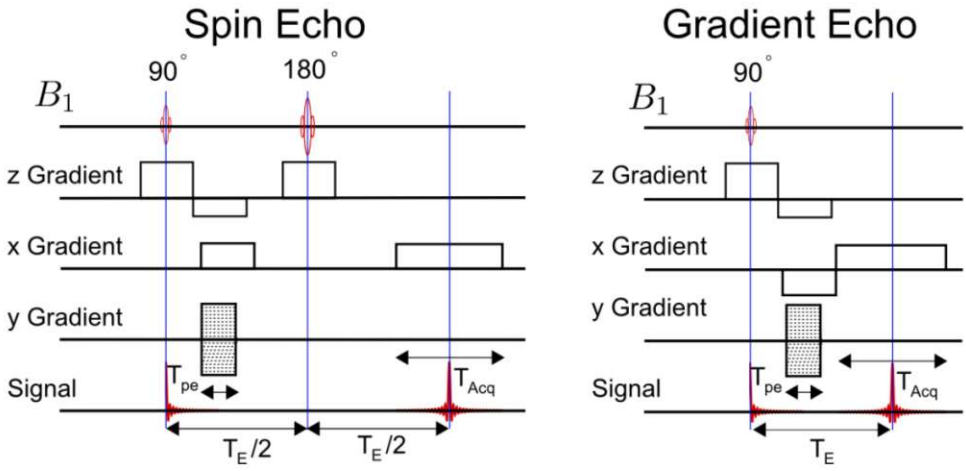

Figure 2.5: Principle of a spin-echo sequence and a gradient echo sequence in 3 dimensions, using slice selection with the z Gradient, frequency encoding with the x Gradient and phase encoding with the y Gradient. In both cases during the acquisition window of the signal T_{acq}, the x Gradient is turned on for frequency encoding. In the gradient echo sequence (GRE) it is responsible for the generation of the echo as their is no inversion pulse[6].

Another sequence that allows for additional encoding is the spin-echo with an additional phase- or frequency-encoding gradient during the $T2^*$ decay, which is called a gradient-echo sequence and can be schematically seen in Fig. 2.5 on the right. It offers the potential of encoding additional information in the FID during the sequence which can be brought back during the echo. The echo in a gradient echo sequence is brought back with another gradient while the echo in a spin-echo sequence is brought back with an inversion pulse.

2.2.5 T1- and T2-weighted measurement sequences

After the excitation pulse, the magnetization M_z is deflected into the transversal plane and will instantly start building up again through spin-lattice relaxation. The time until M_z is built

up sufficiently for another excitation pulse is called the repetition time T_R, which is usually a lot longer than the echo time T_E. A measurement sequence using short T_E and T_R is called T_1-weighted while long T_E and T_R characterize a T_2-weighted measurement sequence. T_1- and T_2-weighted MRI sequences put in contrast different types of tissue and both are nowadays standard for clinical application. While T_1-weighted sequences emphasize fat signals, T_2-weighted sequences are used to detect water signals such as the cerebrospinal fluid.

2.2.6 K-space

The FID data points acquired throughout the entire VOI are stored in k-space and their position can be described by the coordinates (k_x, k_y, k_z). In a slice of the brain, k_z is fixed through slice selection and sampling of the FID signal takes place at specific points (k_x, k_y), which are chosen by the frequency and phase encoding gradients. A schematic representation of a 2D k-space can be seen in Fig. 2.6 on the right. The frequency encoded signals $f(\nu)$ typically correspond to a vector k_x in k-space while the strength of the phase encoding gradient defines a location in k-space k_y. In a way, varying magnetic field gradients can be used to move through points in k-space. The distance between each point in k-space is Δk. The field of view in local space is FOV = $\frac{2\pi}{\Delta k}$, which is the region in which the signals are acquired. The total number of voxels in local space defines the resolution N = N1 $\times$ N2 $\times$ N3 and each voxel has a theoretical size of $\Delta V = \frac{FOV}{N}$. However, the actual size of every voxel is different from ΔV as the Fourier transform does not conserve the voxels spatial proportions.

The measured time dependent signal s(k_x,k_y,k_z,t) is transformed into the spectrum in k-space F(k_x,k_y,k_z,ω) in the frequency domain with a spectral Fourier transform. As the signal is sampled at discrete time points, a discrete Fourier transform will also process the signal from the time domain to the frequency domain. Then, a 3D-spatial Fourier transform

$$f(\vec{r}, \omega) = \int_{-\infty}^{\infty} F(\vec{k}, \omega) e^{-i\vec{k}\vec{r}} d\vec{r} \tag{2.18}$$

yields the spectra f(x,y,z,ω) in image space. In practice this is done using a fast Fourier transform algorithm.

2.3 Magnetic resonance spectroscopic imaging

MRS and MRI are the basis for magnetic resonance spectroscopic imaging (MRSI) - which combines both spectroscopic methods and multi-voxel imaging methods to create multi-dimensional maps of the measured spectra. MRSI measurement data can be reconstructed to an image of

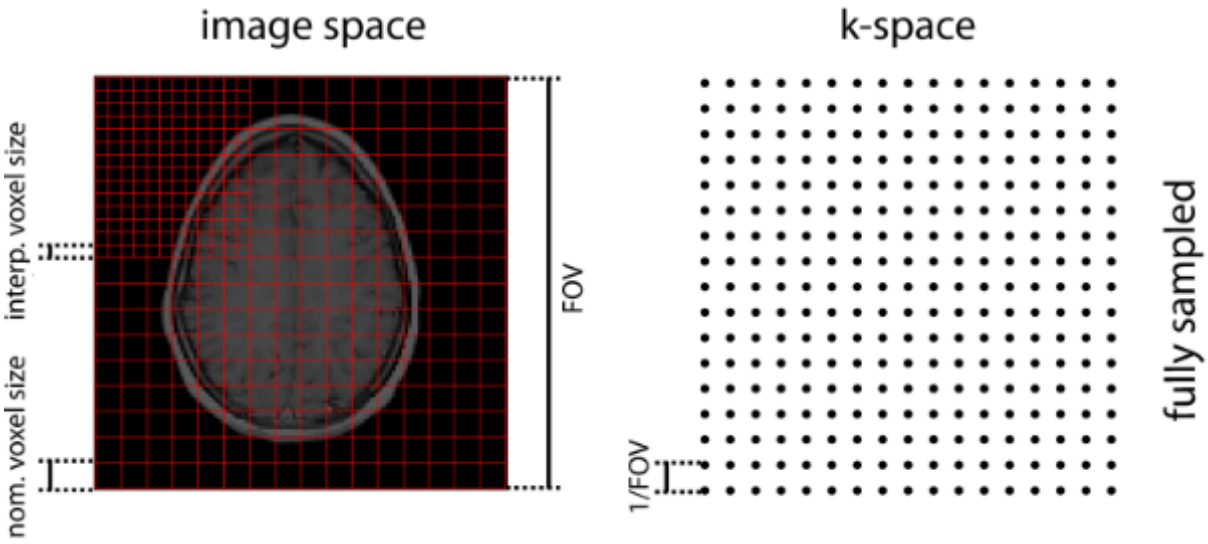

Figure 2.6: Image space (left) and k-space (right) of a slice in the brain[7]. At every point in k-space, the FID is measured and a fourier transform of the data set will result in the image on the left. By interpolating the data using zero-filling, the matrix size and thus the spatial resolution can be further increased. This process will be further explained in Section 3.2.

the brain that is both spatially and spectrally resolved. This means that for every voxel in the brain we obtain a spectrum that contains the information about the components present in the tissue. By varying the applied magnetic gradients before and during acquisition, i.e. through frequency- and phase-encoding, we can "navigate" through k-space and measure the FID signal at every point. Through a Fourier transform we can obtain the spectra points in k-space which can then be associated with voxels in real space (2.10). A more detailed description of MRSI can be found in [1].

2.3.1 Non-cartesian trajectories

In most clinical applications, k-space is transversed in a standard rectilinear line-by-line path, which has the advantage that the images are easy to reconstruct but scanning times are very long. However, the data can also be collected through non-cartesian trajectories, such as spiral or radial trajectories in k-space, which require more complicated algorithms to be reconstructed to an image but offer many advantages compared to cartesian trajectories. Next to requiring significantly reduced scanning times, they contain less unwanted artifacts from undersampling, are less affected by motion during acquisition and allow motion-correction algorithms, allow for ultra-short TE acquisitions, spectrally selective imaging and chemical shift[8].

The trajectory used to sample k-space for the measurements that were made for this thesis

are concentric ring trajectories (CRT), that have an increasing radius after every excitation, which is achieved by using sine and cosine modulated magnetic gradients. The number of orbits after each excitation corresponds to the spectral bandwidth. The FID of same points on these rings in k-space are measured and used to obtain the corresponding spectrum through Fourier transform. Then, after every other excitation pulse, the radius of the ring is increased until k-space is completely filled up. For high spectral bandwidths, this has many advantages as the self-rewinding property of CRTs are more SNR-efficient, faster, and less susceptible to gradient imperfections than other spatial-spectral encoding approaches[9]. This method is sketched in Fig. 2.7. This approach has been used before in studies using 3T MR scanners and has proven to be a reliable and efficient data acquisition pattern [10, 11]. While CRT encoding has been used in combination with a 3D-FID-MRSI sequence in previous studies in 7T and 3T, it has not been used in dynamic ^{1}H-DMI, which involves repeated measurements over a longer period of time. This approach requires thus high temporal and spatial reliability of the used encoding technique.

Further information on MRS and MRSI can be found in [7, 12, 13].

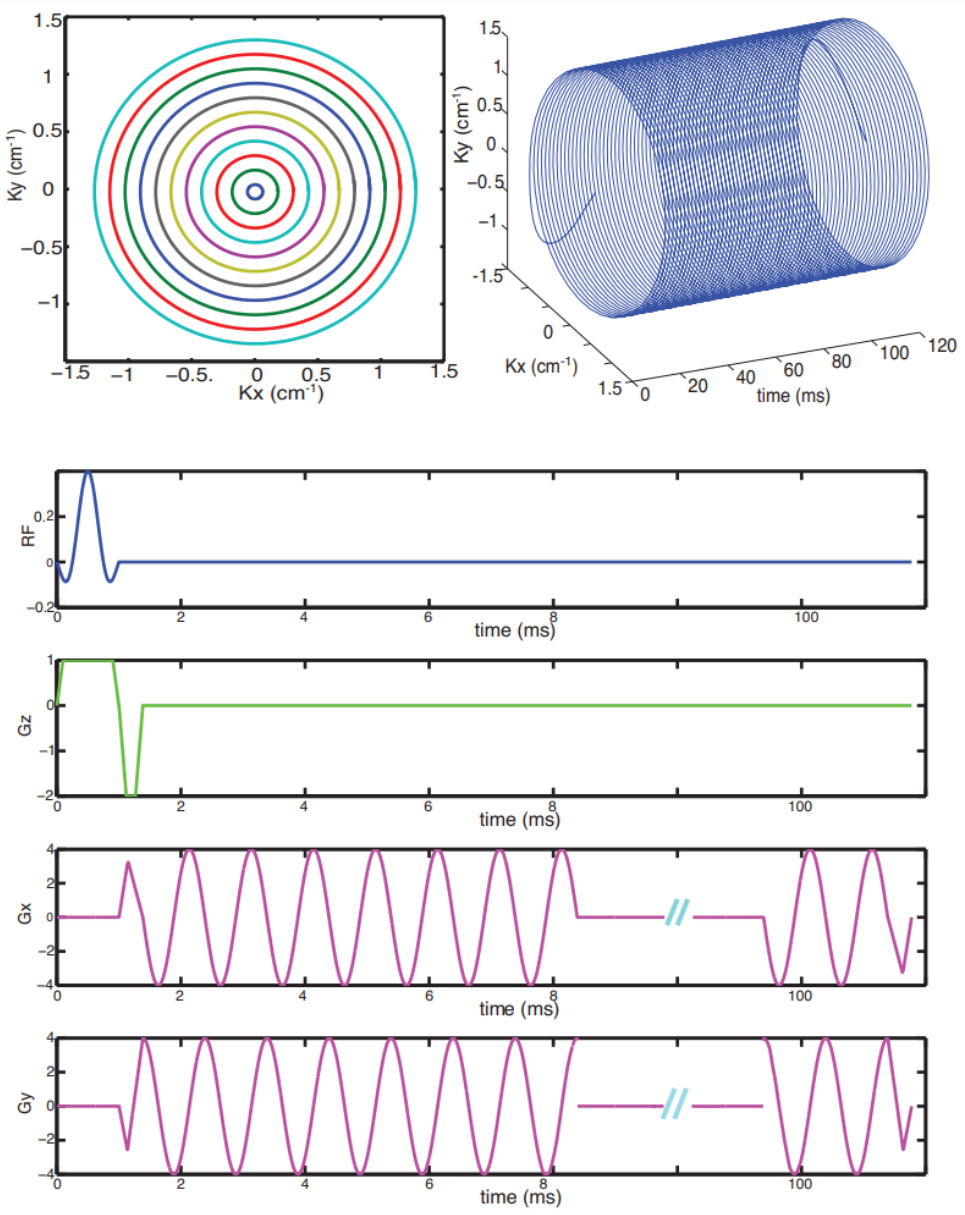

Figure 2.7: Principle of CRT encoding[14]: The upper left graph shows the trajectory in k-space, the different colors represent different radii that become increasingly large after every repetition TR. The upper right graph shows the trajectory in k-space over the duration of one excitation. The four lower graphs represent the magnetic fields induced by (top to bottom) the RF coil, the gradient coils G_x, G_y, G_z. While G_z is used for slice selection, G_x and G_y are used for the acquisition of the signal.

2.3.2 Metabolic maps

After having linked the acquired spectra to a voxel in the brain, a specialized software called LCModel[15] analyses each spectrum with a given basis containing the spectrum of a number

of metabolites and identifies the most fitting linear combination of these. One of these fit spectra can be seen in Fig. 2.8. The coefficients of this linear combination correspond to an amplitude, which means that a higher peak in the spectrum, i.e. a stronger signal of a certain metabolite correlates with its concentration in the voxel where the signal has been measured. However, this is not an absolute concentration, as there are other factors that decorrelate the extracted amplitude from the actual concentration. The reconstructed data have 4 dimensions, three spatial dimensions and one spectral dimension that contains the extracted concentration of the metabolites. Metabolic maps are a 2D slice of the 3D map containing the concentrations of a single metabolite in every voxel. High-resolution metabolic maps of Glu and Gln along with a T1-weighted image of the same slice can be seen in Fig. 2.8 [16].

As a non-deuterated reference molecule for the stability of the measurement sequence we use N-acetylaspartate (NAA) combined with N-acetylaspartatylglutamate (NAAG), as their sum, NAA+NAAG (tNAA), produces a large and constant signal both in white matter and in grey matter, which means that we can expect the amplitudes extracted from the spectrum to be very consistent over multiple measurements. Other metabolites that we are interested in are Glutamine (Gln) and Glutamate (Glu), two amino acids that are metabolic byproducts from glucose metabolism in the brain as well as Lactate. These and other metabolites involved in metabolic cycles in the brain will be further introduced in the following section.

2.3.3 Metabolites in a human brain

Molecules involved in metabolic cycles in the brain are called metabolites. These can be intermediary or end products of metabolism. While there are more chemical compounds involved in metabolic pathways, some important ones, represented in the spectrum in Fig. 2.9 will be briefly described in the following Section. All data on the following metabolites are taken from [1].

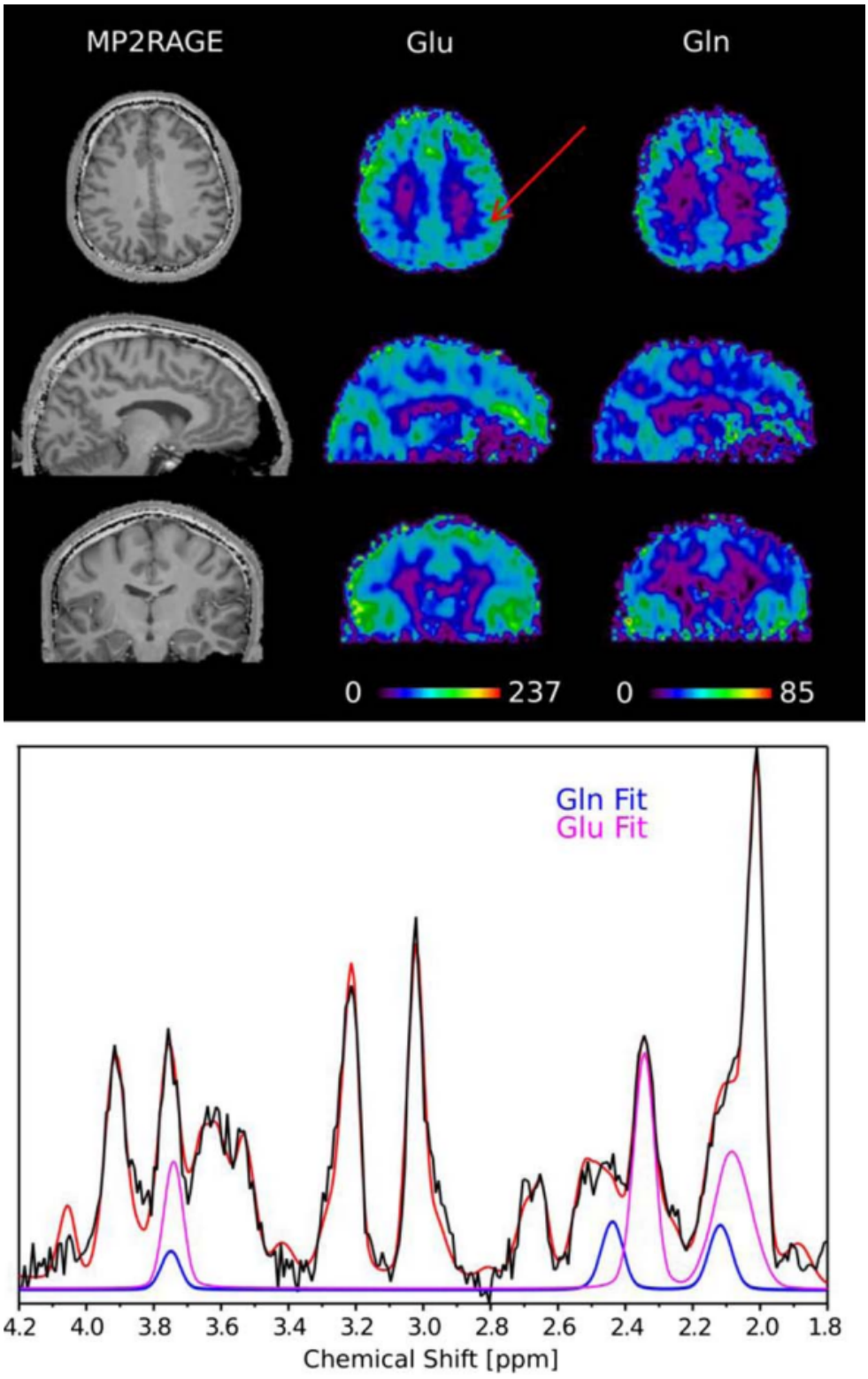

Figure 2.8: High resolution (80×80×47) T1-weighted maps obtained through MP2RAGE (left column), metabolic maps of Glu (middle column) and Gln (right column) of a healthy subject in 7T. The red arrow indicates the voxel where the spectrum below has been acquired. The metabolites in this spectrum were fitted using LCModel and the fit curves for Gln (blue) and Glu (pink) show the spectral separation between Gln and Glu resonances at 7T[16].

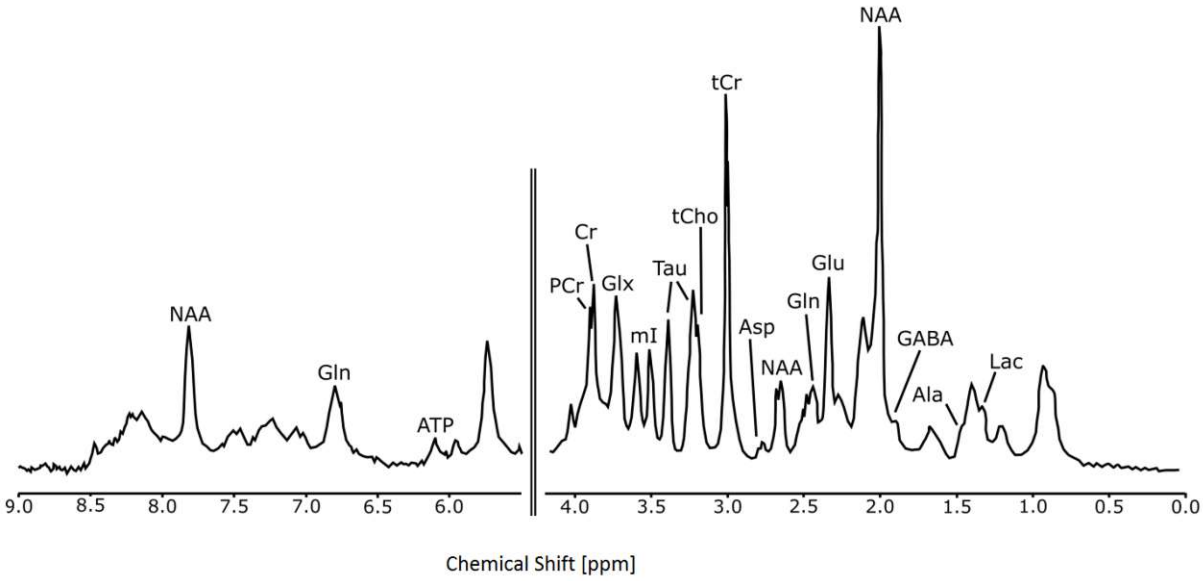

Figure 2.9: Commonly detected metabolites using ^1H-MRS in a voxel in a human brain [1].

Alanine (Ala)

Alanine is an amino acid that is closely linked to metabolic pathways such as glycolysis, gluconeogenesis and the TCA cycle. It is usually present in concentrations around 0.5 mM/L. Alanine shows a resonance signal has a doublet resonance at 1.47 ppm and a quartet resonance at 3.77 ppm.

Aspartic Acid (Asp)

Aspartate is an amino acid that acts as a excitatory neurotransmitter. Synthesized in the brain from glucose, its a key component of the transport of electrons through the mitochondrial inner membrane. It's usually present in the brain in concentrations around 1-2 mM/L. Aspartate has a pair of doublet-of-doublet resonance signals at 2.67 ppm and 2.80 ppm.

Total choline (tCho)

Total choline resonance signal at 3.2 ppm contains contributions from free choline (Cho), glycerophoshorylcholine (GPC), and phosphorylcholine (PC) and is next to NAA and tCr one of the most prominent resonance signals in the brain. High tCho signals can be observed in subjects with Alzheimer's disease, multiple sclerosis and cancer while low tCho concentrations are an indication for liver disease and stroke.

Total creatine (tCr)

Total creatine refers to the combined resonance signal of creatine(Cr) and phospocreatine(PCr). They have singlet resonance signals at around 3.03 ppm and 3.93 ppm. Total creatine plays a

major role in the energy metabolism of cells. Concentrations of creatine are usually around 4.5-6.0 mM/L and concentrations of phospocreatine are usually around 4.0-5.5 mM/L. Decreased levels of creatine have been observed during the chronic phase of pathological disorders such as tumors or strokes.

γ-aminobutyric acid (GABA)

γ-aminobutyric acid is an amino acid that acts as an inhibitory neutrotransmitter that is synthesized from glutamate. GABA has a quintet resonance signal at 1.89 ppm and triplet resonance signals at 2.28 ppm and at 3.0 ppm. All of its resonance signals overlap with stronger resonance signals, making it hard to detect without spectral editing methods. It is usually present in the brain in concentrations around 1 mM/L but altered levels of GABA can be observed in patients with several neurological or psychiatric disorders.

Glutamine (Gln)

Glutamine is an amino acid synthesized from Glutamate. It has a doublet-of-doublets resonance at 3.77 ppm as well as multiplet resonance signals between 2.12 ppm and 2.46 ppm. It plays an important role in intermediary metabolism in the brain and in the glutamate-glutamine neurotransmitter cycle. Its usual concentrations in the brain vary from 2-4 mM/L.

Glutamate (Glu)

Glutamate is an amino acid acting as the major excitatory neurotransmitter and as a direct precursor for GABA. Further, it is a relevant component in the synthesis of other metabolites, small peptides and proteins. It has a resonance signal appearing as doublet-of-doublets at 3.75 ppm and mulitplet resonance signals between 2.04 ppm and 2.35 ppm. It's present in concentrations between 8-12 mM/L.

Lactate (Lac)

Lactate is the end product of anaerobic glycolysis and is usually present in low concentrations of 0.5 mM/L in a healthy brain. However, lactate concentrations in the brain are increased in case of functional activation, restricted blood flow or in tumor tissue. A resonance signal in form of a doublet can be observed at 1.31 ppm and a quartet resonance can be observed at 4.10 ppm.

N-Acetyl Aspartate (NAA)

N-Acetyl Aspartate is after glutamate the second most conentrated metabolite in the brain. It has the most prominent resonance signal in ^1H-NMR spectra at 2.01 ppm. Further, there are

smaller doublet-of-doublets resonances at 2.49 ppm, 2.67 ppm and 4.38 ppm. NAA is used as a marker of neuronal density, as a decrease in NAA concentrations can be observed in disorders that are accompanied by neuronal loss. NAA is also used as a concentration marker, as it is relatively immune to acute metabolic disturbances such as ischemia or hypoxia. There are however differences in NAA concentrations in GM (8-11 mM/L) and WM (6-9 mM/L). In addition, N-acetyl aspartyl glutamate (NAAG) has a resonance signal that coincides with the NAA methyl peak at 2.01 ppm so often the sum of both (tNAA) is used as a reference concentration marker instead.

2.4 Brain Metabolism

The brain, being one of the most active and complex organs of the body, has to be constantly supplied with nutrients and energy. This energy is stored in a molecule called adenosine triphosphate (ATP), which is the molecule that all cells in the body require to function properly. In healthy tissue, glucose and oxygen are converted through aerobic respiration into ATP. More precisely, this conversion happens in the mitochondria of the cell through the citric acid cycle. Through glycolysis, glucose is broken down into pyruvic acid and the energy that is being freed in the process is then used to form ATP. The schematic metabolic cycle including other relevant enzymes can be seen in Fig. 2.10.

As this metabolic path happens aerobically, i.e. by using oxygen, it requires a constant supply of oxygen to the brain. Usually, when the cell's oxygen supply is not sufficient to sustain aerobic metabolism of glucose, the body switches to the less efficient anaerobic respiration, where the conversion of glucose into ATP happens without oxygen through the lactic acid cycle. In that case, lactate is metabolized as a byproduct. This happens in muscle tissue under heavy stress, i.e. during intensive physical activity. In this case, oxygen supply is not sufficient to sustain aerobic respiration and lactate is produced instead as the cells switch to anaerobic respiration. Lactate is responsible for the muscle soreness after physical activity.

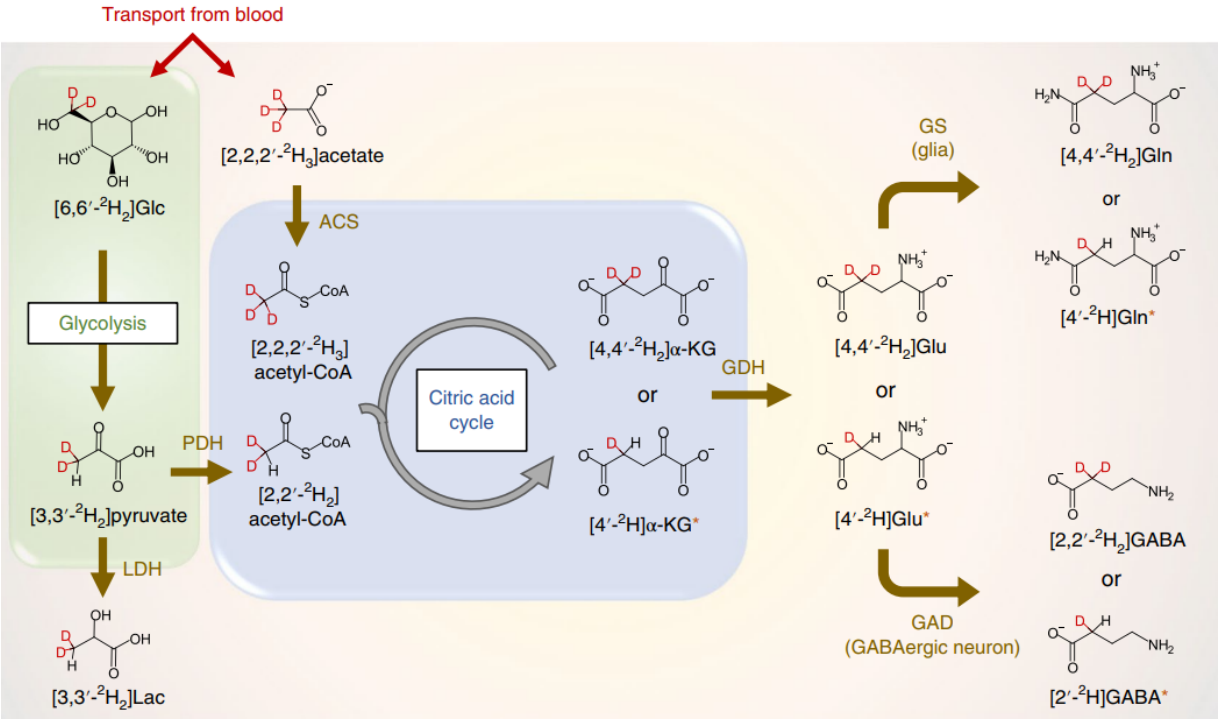

Figure 2.10: Schematic overview of the ^{2}H-labeled glucose metabolism in the brain[17]. The downstream metabolites have the substituted deuterium groups which can be seen in red. The oxidative conversion of Glucose requires the enzyme PDH which leads to the path towards the right side of the graph and thus to deuterated Glx, while the non-oxidative conversion of Glucose uses the enzyme LDH which instead leads to the production of deuterated Lac.

While it is normal in muscle tissue, it should never be the case in the brain. Instead, ATP is supposed to be generated exclusively through aerobic glycolysis in the citric acid cycle. A healthy brain, being one of the most perfused organs, is constantly supplied with sufficient oxygen to keep all brain cells functioning. However, in case that blood vessels are partially or completely blocked, preventing oxygen from reaching the brain cells, metabolism through aerobic respiration is not possible. In this case, lactate is present in significantly higher concentrations in the brain, for instance after having a stroke.

In tumor tissue, glucose is also metabolized through the lactic acid cycle, thus showing increased levels of lactate [18] even though the oxygen supply would be sufficient for aerobic respiration. This is called the Warburg effect and it is not yet known why this is the case[19]. Hence, glucose uptake in tumor tissue is also significantly higher than in healthy brain tissue. So, by identifying lactate in the brain and by analysing glucose uptake, we can locate cancer tissue. Nowadays in clinical applications, the standard method used to track glucose uptake in the brain is positron-emission-tomography(PET).

2.4.1 Positron emission tomography (PET)

In PET, a radiotracer is used to track glucose uptake. Most often, the hydroxyl group in glucose is substituted with a radionuclide fluorine-18, this radiotracer is called fluorodeoxyglucose (FDG). After injection of FDG in solution, the glucose will be distributed through the body, mostly however in the brain. This modified glucose has the property of accumulating in higher concentrations in tumor tissue than in normal brain tissue. Through $\beta+$ decay, positrons are emitted which react with electrons causing the annihilation of the two particles and the creation of two energetically equal photons, which are emitted simultaneously in opposite directions. If they are then simultaneously detected in opposing spots with the same energy, it can be deduced that they originate from the same annihilation event. Thus, it can be tracked where the annihilation has taken place and where FDG has accumulated. The key mechanism of PET can be seen in Fig. 2.11.

FDG uptake in the brain is similar to glucose, however FDG is metabolized differently than glucose. Also, the radioactive group is not transferred to the metabolic follow-up products such as glutamine, glutamate or lactate. While FDG can be used to quantify glucose consumption, it cannot track its further metabolism. Instead, to track in vivo glucose downstream metabolism we use a method called deuterium metabolic imaging.

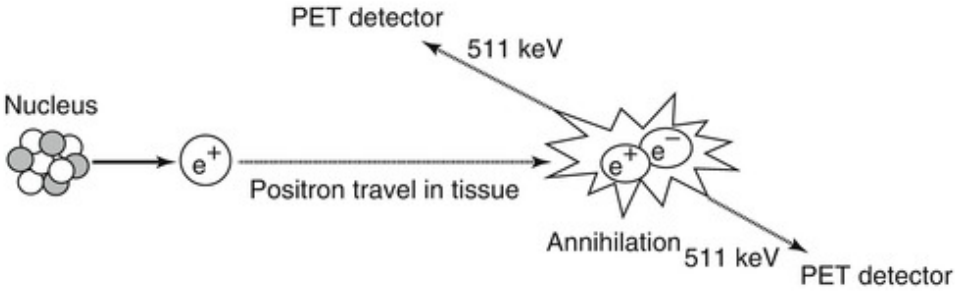

Figure 2.11: Schematic representation of the PET mechanism[20]. A nucleus of the radiotracer FDG, which accumulates in tumor tissue because of the increased glucose uptake, emits a positron which reacts with nearby electrons, causing the annihilation of the positron and the electron and the subsequent emission of 2 equally highly energetic photons in opposite directions. From the simultaneous detection of both photons we can track the location of the annihilation process and thus the position of the tumor tissue.

2.4.2 Deuterium metabolic imaging

With standard ^1H MRS, we can only directly detect the signal caused by hydrogen groups. However, deuterium has an additional neutron in its core and its gyromagnetic ratio and thus

its resonance frequency is significantly lower by a factor of about 6.5 than the one of a hydrogen nucleus and thus outside of the measured spectrum. Technically it is possible to directly detect the signal from deuterium groups, however a special deuterium coil is necessary to pick up their signal, which is by itself already very expensive, requires hardware and software modifications in the scanner as well as additional maintenance. Instead, the deuterium signal is captured indirectly in standard ^1H spectroscopy.

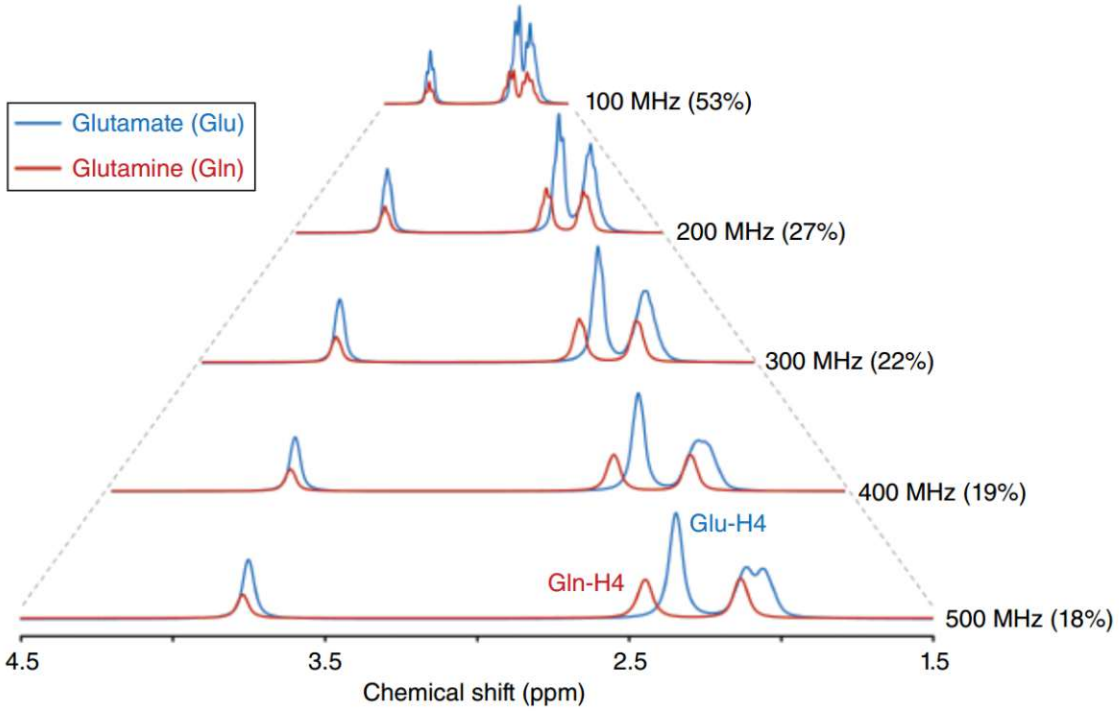

Figure 2.12: Comparison of Gln and Glu resonances for different magnetic field strengths. The percentage represents the overlap of the signals which decreases with increasing field strength, where proton resonance frequencies above 300 MHz represent field strengths of more than 7T[1].

After the ingestion of deuterated glucose, where a hydrogen atom was substituted with deuterium, deuterium will travel through the body and will mostly accumulate in the brain where it is metabolized into its follow up products. Deuterated glucose is chemically similar to glucose and is thus metabolized in the same way. As deuterated glucose replaces normal glucose, the glucose signal that can be picked up by the receiver coil is different, precisely it lacks the signal that originates from the deuterated group. As the presence of deuterium in the molecule changes the NMR spectrum, it allows us to label and track molecules that are deuterated. This labeling is also passed on to the metabolic follow-up products made from it because deuterium does not influence the chemical reactions and the metabolic behaviour. Af-

ter the ingestion of deuterated glucose, metabolic processes in the brain create among others deuterated glutamate and deuterated glutamine. Their NMR spectra are very similar and most of their peaks are just a few hundredths ppm apart as can be seen in Fig. 2.12[1]. With field strengths of 3T glutamate and glutamine have almost overlapping peaks because of their similar chemical structure and their increased bandwidth compared to similar measurements with 7T MR scanners, where they have clearly separated peaks for the methyl groups of glutamate at 2.04 ppm and 2.35 ppm, and of glutamine at 2.12 ppm and 2.46 ppm. While the chemical shift is independent of the field strength, neighboring peaks in the spectrum can be distinguished more easily at high magnetic fields B_0, because the full width at half maximum (FWHM) of signals decreases with increasing B_0. That is why for measurements in 3T MR scanners, the concentrations of glutamine and glutamate are combined to their sum, which is abreviated by Glx.

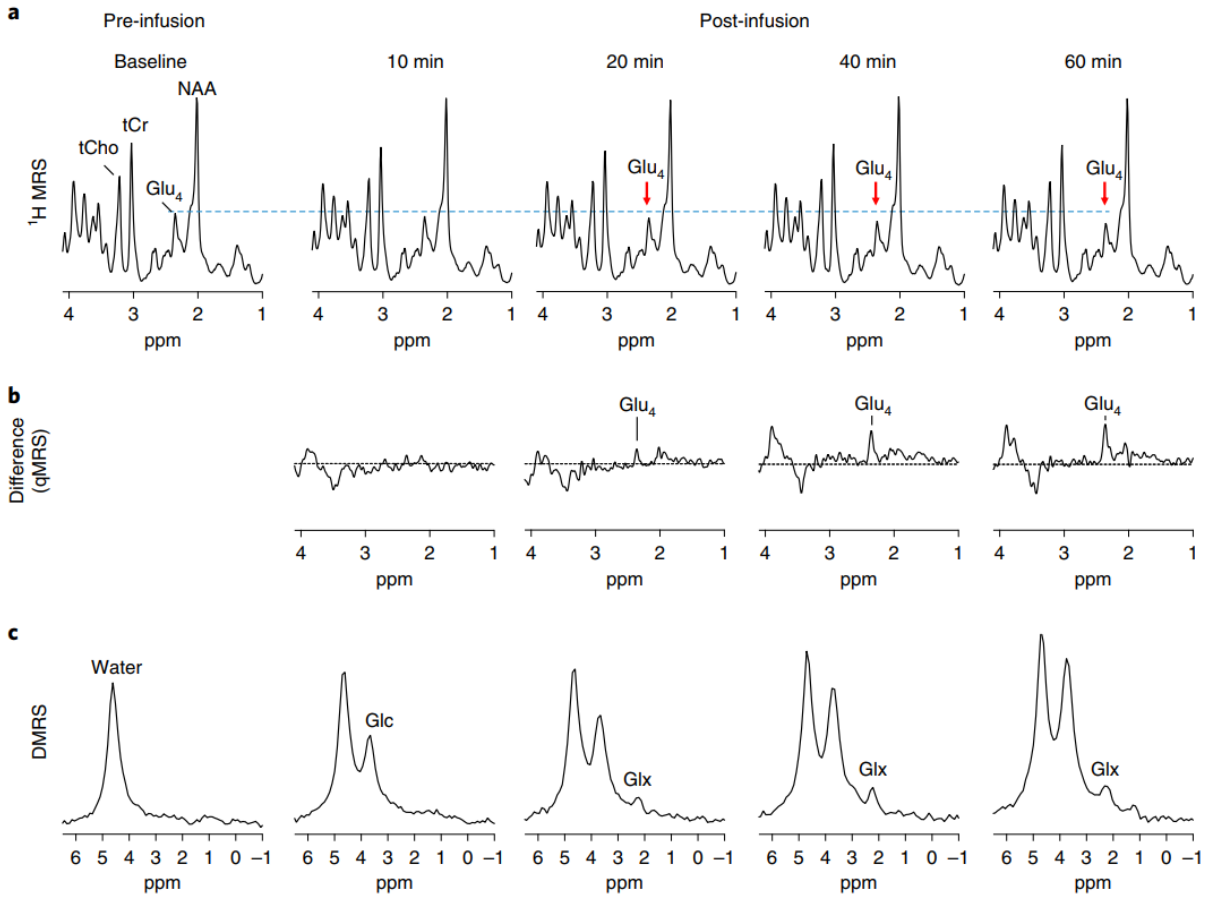

Figure 2.13: Resonance spectra measured with a) ^{1}H-MRS, b) ^{2}H-MRS and c) their difference spectra showing the evolution of the signals from the deuterated group in Glutamate Glu4. The signal becomes less strong in ^{1}H-MRS and simultaneously becomes stronger in ^{2}H-MRS[17].

As more Glx is deuterated, the measured signal caused by the deuterated group in Glx will decrease for each subsequent measurement, as the receiver coil cannot pick up the deuterium signal. In Fig. 2.13 we can see how the Glx4 resonance signal decreases in ^{1}H-MRS and simultaneously increases in ^{2}H-MRS (DMRS). This decrease will be proportional to the concentration of deuterated Glx and will quantify the metabolism of glucose into glutamine and glutamate. The NMR spectra of glutamate and glutamine are split up into two spectra with the hydrogen groups and with the deuterium group (Fig 3.2), which will be two different basis sets given as parameters for LCModel, which can then extract the amplitudes of the hydrogen groups and the deuterium group of Glx independently from the measured spectrum and create metabolic maps of both. This allows us to see how in a healthy brain glucose is metabolized into glutamate and glutamine. This is not the case in tumor tissue, where glucose is instead metabolized into lactate. The deuterium nuclei from glucose are also transmitted into lactate, which means that lactate will also have a deuterated group and will thus be trackable by using the same method. The NMR spectrum of lactate will be split up into an NMR spectrum with the deuterated group (Fig 3.2 (a,b)) and an NMR spectrum with the hydrogen groups (Fig 3.2 (c,d)). Then, given these two spectra as basis, LCModel can extrapolate lactate concentrations in the brain over multiple measurements and in regions where the deuterated lactate signals decrease, we can deduce that glucose is metabolized through the lactic acid cycle instead of the citric acid cycle[21].

Chapter 3

Methods

3.1 Measurement protocol

For this study, all measurement sessions have taken place in a 3T Prisma MR scanner (MAGNETOM, Siemens Healthcare) with a 64-channel head coil (Siemens Healthcare). Written consent from all healthy volunteers as well as a questionnaire to exclude abnormal medical conditions were obtained before the measurements.

The first part of the measurement protocol is a 3D T1-weighted MPRAGE (Magnetization Prepared Rapid Acquisition with Gradient Echoes) sequence, which will be used as a reference throughout the whole measurement process to position the MRSI volume. To reduce B_0 field inhomogeneities, first and second order shimming was applied over the VOI using the standard Siemens routines as well as manual shimming. A fluid-attenuated inversion recovery sequence (FLAIR), with very long repetition time T_R and echo time T_E, is sometimes used to identify cerebrospinal fluid and to suppress it by darkening it in the image. This further increases the resolution of the picture and emphasizes the difference between white and grey matter. Finally, the 3D-FID-MRSI sequence with an acquisition delay of 0.8 ms and a repetition time TR = 850 ms was used to acquire the data that was later reconstructed into the metabolic maps. The schematic composition of the MRSI sequence can be seen in Fig. 3.1.

During the MRSI sequence, a motion correction algorithm called volume Navigator (vNav) was simultaneously turned on to correct small motions of the head in real time. Every time the CRT radius is increased, a T1-weighted B_0 image is generated through a single-echo sequence and compared to the previous B_0 image. By identifying relative translational and rotational differences between consecutive B_0 images, the Navigator can correct small motions of the head and reposition the acquisition volume accordingly. The total navigator block including

acquisition and processing of the B_0 map and feedback to the MRSI sequence takes about 360 ms. Outer volume saturation bands (30mm) placed below the VOI were used to suppress unwanted signals from outside areas. Signals from all the coils were combined using iMUSICAL[22]. Water suppression was done using WET [23]. Finally the data is acquired during the readout using concentric ring trajectories.

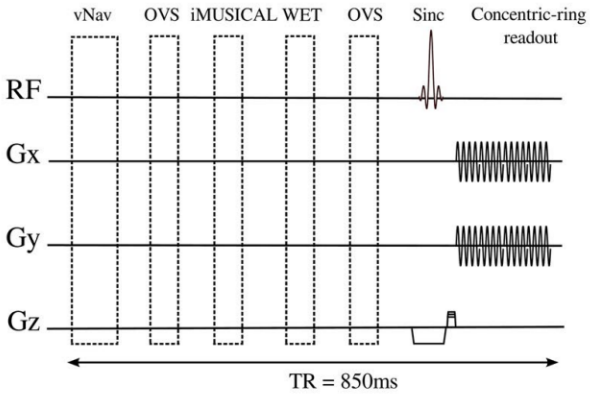

Figure 3.1: Schematic structure of the used 3D-FID-MRSI sequence with the key components of the MRSI sequence being the volume Navigator (vNav), outer volume suppression (OVS), the iMUSICAL coil combination pre scan and water suppression enhanced through T1 effects (WET)[9].

More detailed information about the used MRSI sequence as well as the Navigator can be found in [9].

3.2 Data Processing and Reconstruction

The raw data acquired by the MR scanner can't be directly used because the FID of each voxel is not acquired voxelwise but the FID of multiple voxels are acquired simultanously in an interlayed manner. As k-space is transversed in concentric rings, the acquisition pattern has to be taken into account to assign parts of the FID signal to their corresponding voxel. The raw acquired data is reconstructed in what's known as the processing pipeline, which was developed at the High Field Magnetic Resonance Centre and consists of a series of scripts based on BASH[24] and MATLAB[25].

Several intermediate steps process the raw time-dependent signal to a 4D map that associates a metabolic concentration to every voxel in the brain. First, the raw data are read into the pipeline along with data acquired by a T1-weighted sequence, a control file, a basis set and a number of options concerning various parameters required for the processing and the spec-

tral fitting. The T1-weighted images are used as a reference for the localisation of the voxels. The content of the control file includes among others the number and name of metabolites that will be extracted from the spectra as well as the chemical shift range, i.e. the frequency range in which signals will be fitted. The basis set contains the NMR spectrum of every metabolite listed in the control file, which will be used as a reference for the fitting process.

The next step is the pre-processing of the data, which includes among others the calculation of noise for SNR maps, the generation of a brain mask for the exclusion of signals outside of the brain and the suppression of water and lipid signals. The data are then reconstructed by using a method called MUSICAL (MUltichannel Spectroscopic data combined by matching Image Calibration Data)[22] which sums up the weighted signals from all 32 receiver coils. The data will then be resampled by adding a number of zeros to the spectrum, which can further increase the resolution of the spectrum and reduce unwanted artifacts after being Fourier-transformed[26]. This is done to the data prior to being processed and fitted by LCModel. Then the data will be transformed through a spectral FFT in the frequency domain and lastly a 3D spatial FFT will bring the data from k-space into local space, yielding a 4-dimensional tensor containing the location and the NMR spectrum of every voxel. In combination with the T1-weighted B_0 images, visual anomalies in the tissue can then be further investigated by analysing the NMR spectrum at the corresponding location.

3.3 LCModel spectral fitting

These frequency spectra for every voxel are the input for the fitting software LCModel. This software fits a linear combination of the metabolites given in the basis set to a given NMR spectrum in a spectral range from 1.8 ppm to 4.2 ppm. The basis used for Gln and Glu can be seen in Fig. 3.2. The resonance signals have been split up into the signal caused by the deuterated group of Gln (a) and Glu (b) as well as the corresponding non-deuterated groups signal right below. Additionally for the simulation of Lactate, the fitting range was extended from 8 ppm to 1 ppm with a gap between 7 ppm and 4.2 ppm to include the resonance signals of lactate at 1.31 ppm and a reference signal at 8 ppm. The measured NMR spectrum is the black curve in Fig. 3.3. and the fit spectrum is the red curve in Fig. 3.3. Some of the important metabolite peaks are represented in the spectrum. The linear coefficient of each metabolite represents its corresponding abundancy in the measured spectrum, which correlates with its concentration in the voxel. The used reference molecule for the chemical shift at $\delta = 0$ is sodium trimethylsilylpropanesulfonate (DSS), as it is soluble in water and has a strong and stable signal in most conditions.

Glucose metabolism was tracked by measuring and fitting the Glx4 signal (A.5+A.8) independently from the rest of the Glx spectrum. As the non-deuterated peaks produce a signal that stays relatively constant over time, they are separated from the deuterated peak's signal, which decreases over time. LCModel treats their signals as if they were different metabolites and can thus independently quantify the evolution of the Glx4 signal. From the fitted spectra, the concentration of a metabolite at every voxel can be extracted and assembled in a metabolic map containing the concentration of a metabolite at every voxel in a slice of the brain.

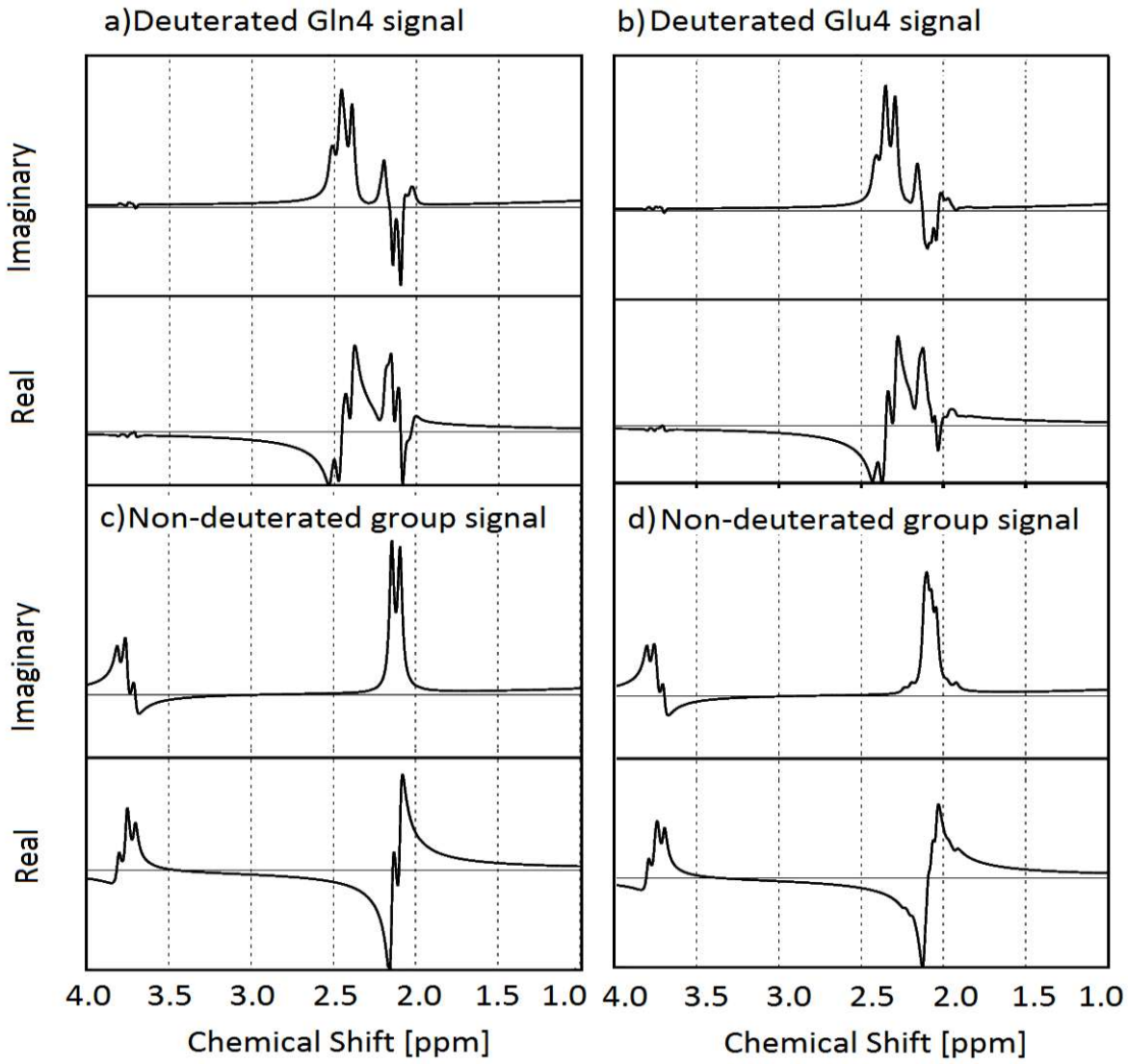

Figure 3.2: Basis spectra used for the detection of deuterated Glu and Gln. a) and b) represent the deuterated groups of Gln and Glu respectively where hydrogen is exchanged with deuterium, the combined signal of a) and b) is Glx4. c) and d) represent the remaining resonances caused by the non-deuterated groups of Gln and Glu respectively.

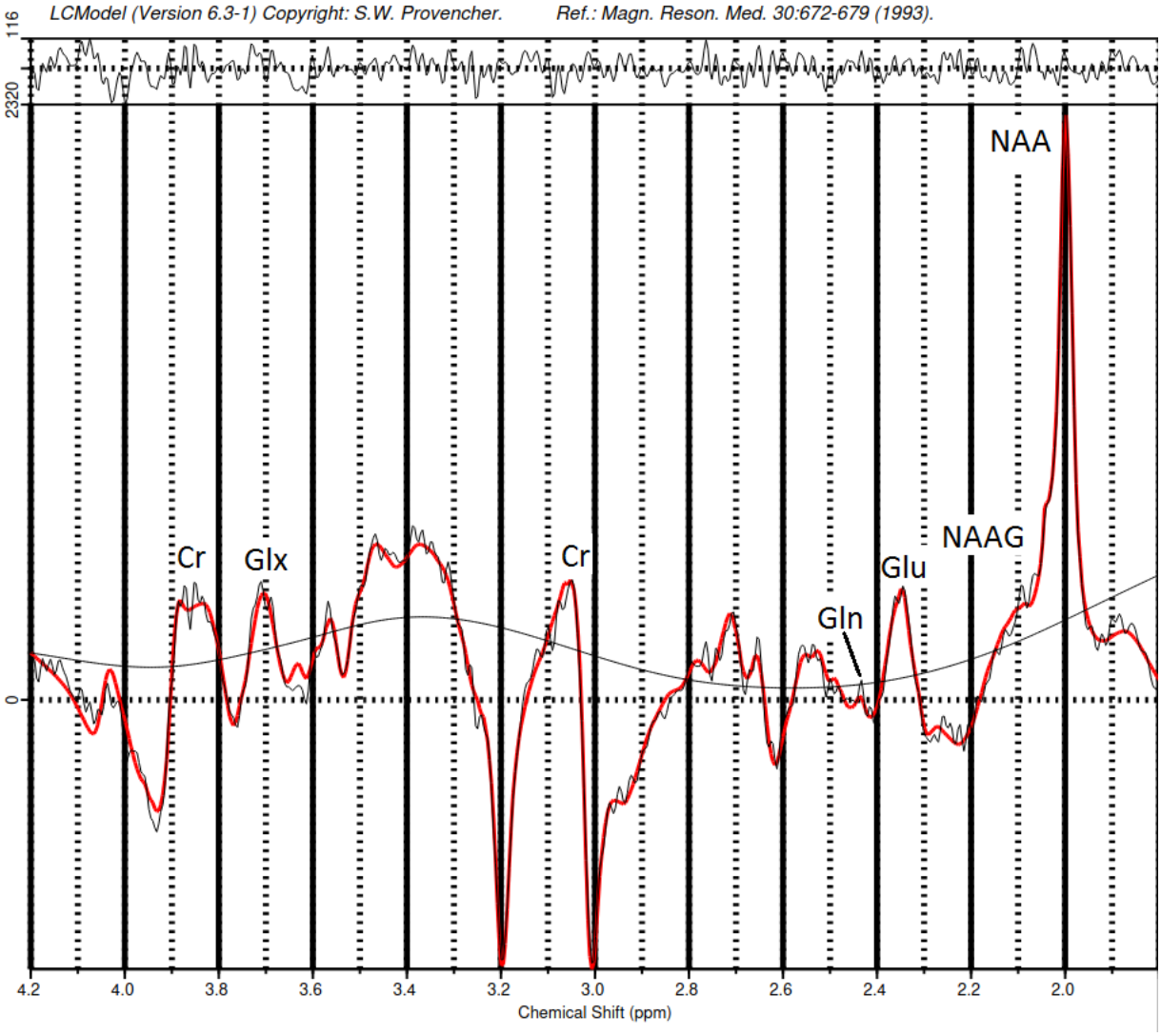

Figure 3.3: Example of a fit spectrum (red curve) by LCModel of a measured NMR spectrum (black curve) from 4.2 ppm to 1.8 ppm in a voxel in the brain with some of the relevant metabolite signals.

3.4 Analysis

The data were processed and analysed with MATLAB[25]. The metabolic maps of tNAA as a reference, of Glx and of the deuterated group in Glu and Gln, Glx4, were used for the analysis. Every subject was repeateadly measured with the same measurement sequence and for every repetition, concentrations were compared both voxelwise and averaged over whole slices. The main indicator used for the quantification of the stability of the results was the coefficient of variation $CV = \sigma/\mu$ with σ being the standard deviation andμ being the arithmetic mean. The standard deviation represents how much the individual concentrations deviate from the

mean,

$$\sigma = \sqrt{\frac{1}{N}\sum_{i=1}^{N}(x_i - \mu)^2} \tag{3.1}$$

with

$$\mu = \frac{1}{N}\sum_{i=1}^{N} x_i. \tag{3.2}$$

The CV of a probability distribution is a dimensionless indicator for the dispersion of the distribution given in % and shows how much the data of the set fluctuate without taking into account the absolute value of the concentration. The lower the CV of the extracted metabolites concentration, the more consistently can the method quantify the actual concentration in the brain. Even though different metabolites in the brain have different concentration ranges, the coefficient of variation is always a meaningful indicator for the stability of the results. In tNAA there should be almost no fluctuation over time as the tNAA concentration is very stable over time, since it produces a strong and consistent signal both in WM and GM.

3.5 Linear Fitting

After ingestion of deuterated glucose substrate, the signal caused by the deuterated groups will not be picked up in the receiver coil anymore as it is only able to pick up proton resonances. Over time, more glucose will be metabolized into deuterated Glu and deuterated Gln (deuterated Glx), which means that their deuterated group will not have a resonance effect at the usual resonance frequency in the magnetic field and will not be picked up by the receiver coil, as if Glx concentrations were decreasing.

The signal caused by the Glx4 group will decrease after each measurement as more Glx will be deuterated through the metabolism of deuterated glucose. To quantify the decrease, Glx4 concentrations in a single voxel over all repetitions were compared and a linear fit function calculated by linear regression in MATLAB was used to estimate the trend of concentrations. Applied to every voxel, the decline of the Glx4 concentrations throughout the brain was mapped in linear fit maps where every voxel contains the linear coefficient of the fit function. The slope of the linear function in every voxel mapped on every slice gives information on the metabolic rate of the deuterated metabolites. This does not imply that a linear model is assumed for the metabolism, instead it is used to indicate how well the decay of deuterated metabolites can be observed in ^{1}H-MRS in 3T.

Metabolites whose concentrations remain constant have little to no slope since their concentrations are only determined by random fluctuations and noise. The quality of the linear fit function is quantified with two statistical indicators, namely the P-value and the R-value. The P-value can take a value between 0 and 1 and is used to interpret the statistical significance of a result. The p-value is the probability of getting a sample statistic given that a certain null hypothesis is true. Our null hypothesis in this case is that after ingestion of the deuterated glucose substrate no change in Glx or Lac concentrations will be observed. The alternative hypothesis is that the ingestion of a deuterated glucose substrate will cause a variation in Glx or Lac concentrations. If the p-value is larger than the threshold of 5% we can not reject the null hypothesis as it would mean that at least 5% of the data points of the sample would confirm the statistics described by the null hypothesis. If the p-value is lower than the threshold of 5% we can reject the null hypothesis, indicating a correlation between the measured data and the alternative hypothesis. This is due to the fact that more than 95% of the data points match the statistics described by the alternative hypothesis, which is strong evidence for the alternative hypothesis being true. Thus if $p < 0.05$ we can assume that the slope in a voxel is not random but is due to the hypothesis being the decay in concentrations after the labeling of metabolites with deuterium. The R-value can take a value between -1 and 1 and describes how strongly the data points correlate with the slope. The closer the R-value is to the extreme points -1 and 1, the stronger does the slope correlate with the data in the voxel, i.e. the better does the linear function follow the trend of the data. An R-value of ± 1 means perfect correlation i.e. all the data points are on the linear function and an R-value of 0 describes no correlation with the data, i.e. all the data points are randomly distributed. A negative R-value in a voxel means that concentrations decrease over time and a positive R-value indicates increasing concentrations over time.

LCModel does not calculate absolute concentrations, instead the amplitudes extracted during the fitting process are given in arbitray units and are thus not indicative for the actual concentrations. Nevertheless the concentrations in the brain correlate with these arbitrary units over time, which means that a decrease of 25% in A.U. corresponds to a decrease of 25% in the actual concentrations. As a reference, the average concentration for Glu is 8 mM/L, the average concentration of Gln is 2 mM/L and the average concentration of tNAA is 10 mM/L. As Glu and Gln are combined to Glx, their average concentration is assumed to be 10 mM/L [27]. These are taken as the starting concentrations for the linear fit function, to put the slopes of Glx concentrations over time into perspective.

3.6 Lactate signal simulation

Since Glucose can be metabolized non-oxidatively through the lactic acid cycle, DMI is also used to track in-vivo lactate concentrations in the brain. Prior to being used in clinical studies with cancer patients, the ability of the MRSI sequence to detect the lactate signal was evaluated by simulating it in the spectrum instead. After the generation of the spectra, a single lactate NMR signal was added to the measured spectrum. This signal can be seen in Fig. 3.4. The measured NMR spectrum in a voxel and the NMR spectrum before and after the lactate signal has been added can be seen in Fig. 3.5. Afterwards, LCModel was able to extract the amplitude of the lactate signal, allowing for the generation of metabolic maps for the simulated lactate concentrations. For the measurements without the ingestion of deuterated glucose, the simulated lactate was simulated as a constant signal and in line with other metabolic concentrations such as tNAA. For the measurements with deuterated glucose, the amplitude of the simulated lactate signal was decreased for every repetition during the measurement session by 15%, which should simulate the metabolism of deuterated lactate. By analysing the metabolic maps, the ability to consistently detect the simulated Lactate signal could be quantified. While a decrease of 90% after an hour is way above what we would be measuring in a brain, it was used to evaluate how well the lactate concentrations can be fitted below a certain signal strength.

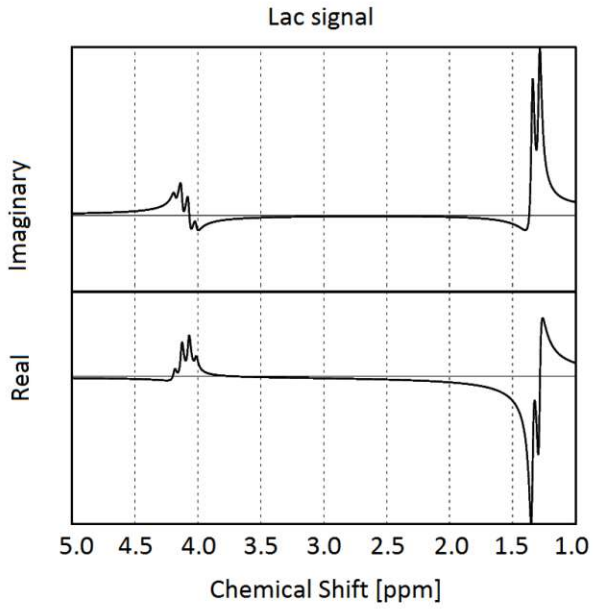

Figure 3.4: Lactate signal used for the simulation with the doublet resonance at 1.31 ppm and the quadruplet resonance at 4.10 ppm.

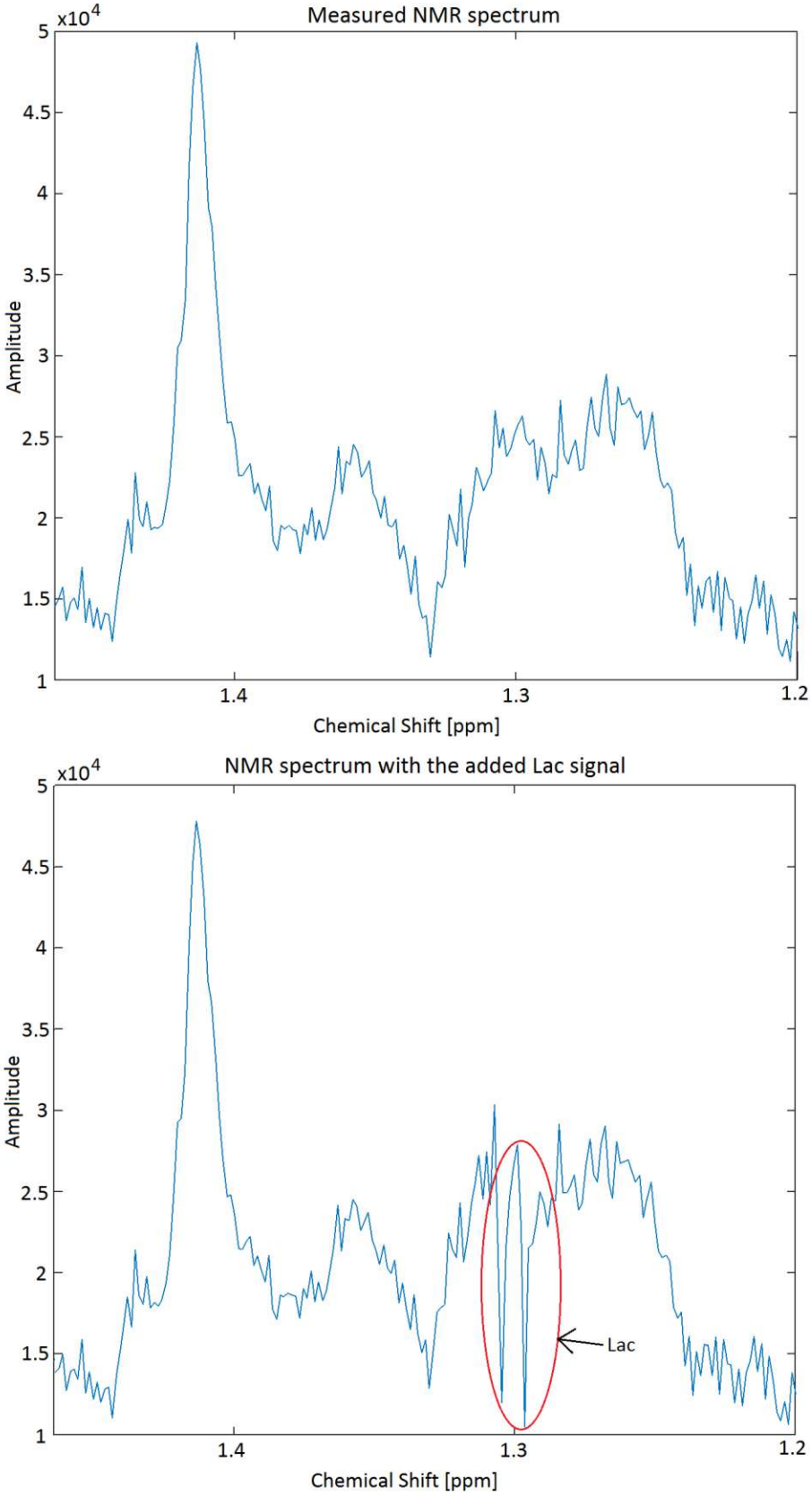

Figure 3.5: Measured spectrum before (top) and after (bottom) the addition of the doublet lactate resonance at 1.31 ppm. The resonance at 1.4 ppm originates from a lipid signal.

The lactate resonance at 1.31 ppm is mostly covered by strong lipid (fat) signals so it is hard to directly detect them in the spectrum. To supress lipid signals, L2-lipid regularization has been applied [28]. This can reduce lipid signals to a minimum, however they are still noticeable as can be seen in Fig. 3.5 which interferes with LCModel's detection and fitting capability of the lactate signal. Further it is not clear, how this L2-lipid regularization can affect the simulated lactate signal. Even though the signal was simulated to be constant, it could not be identified reliably in all voxels. Stronger simulated lactate signals corresponding to concentrations of around 10 mM/L, which is the order of magnitude of lactate concentrations in patients with brain tumors [18], can be fit more reliably. A method used to further increase the sensibility towards lactate signals is the use of subtraction spectra.

3.6.1 Subtraction spectra used for lactate fitting

A major problem when fitting lactate signals is the presence of dominating lipid signals that are in the same chemical shift range as the lactate signal. Even though L2-regularization is applied prior to the fitting process, lipid signals can't be fully suppressed which makes fitting a lot harder. To further increase the quality of the fitting of lactate signals, subsequent spectra of measurements after the first repetition will be subtracted from the inital measurement before the lactate concentration can be extracted from the spectrum. As lipid signals stay relatively constant, they cancel each other out in subsequent spectra. However the lactate signal is simulated to be weaker in every repetition which means that the subsequent subtraction spectrum will have a slightly larger lactate signal, as less of the lactate signal is subtracted from the inital signal in every repetition. While the lactate signal is simulated to decrease over time, the signal strength in the subtraction spectrum will grow for every repetition. That is because the difference between the intial spectrum and spectrum of repeated measurements will become less over time, thus the lactate peak in the subtraction spectrum will become stronger. The other metabolite resonance signals that remain constant over time, like lipid signals, will cancel each other out and cannot be fitted anymore. In theory, subtraction spectra can also be used to detect and to fit deuterated Glx signals as they are also decreasing over time. This has not yet been implemented. The fitting range for these metabolic maps has been increased to 1 ppm to 8.5 ppm with a gap between 4.2 ppm and 7 ppm. An additional inverted lactate signal with a resonance at 8 ppm is used as a reference signal for the fitting process in the subtraction spectra. The inverted lactate signal basis as well as its fit by LCModel in the spectrum with the increased fitting range can be seen in Fig. 3.6 on the left while the simulated lactate signal with the resonance at 1.31 ppm can be seen on the right.

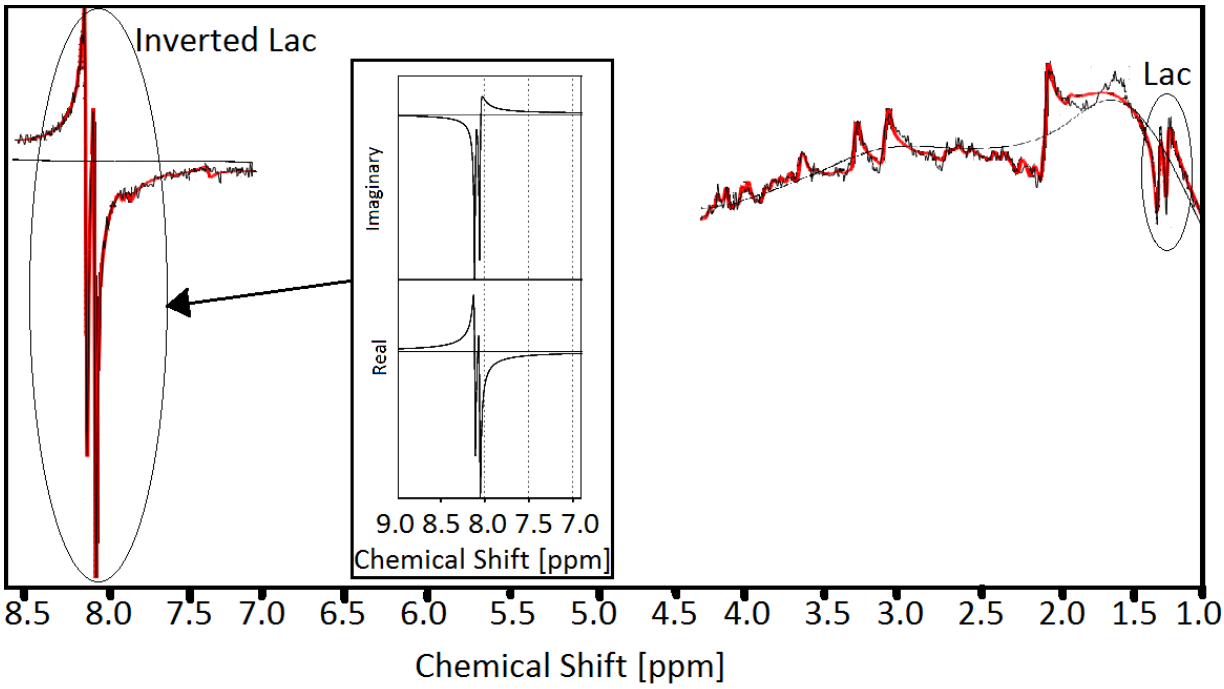

Figure 3.6: Fit spectrum with increased fitting range from 1 ppm to 8 ppm and a gap between 4.2 ppm and 7 ppm including the inverted lactate resonance at 8 ppm shown in the gap. The lactate resonance at 1.31 ppm on the right is about as strong as the signal of tNAA while the inverted lactate is simulated to be about 4 times stronger. The amplitude is in arbitrary units.

3.7 Experimental Setup

3.7.1 Stability of the measurement sequence

As a reference for the stability of the results, 5 measurement sessions with 5 healthy subjects took place. In 4 measurement sessions, every subject was scanned 5 consecutive times with an MRSI sequence with a spectral bandwidth of 1030 Hz, a resolution of $32\times32\times19$ voxels, 258/516 (resampled) spectral points. Every measurement block has taken 3:30 min. In one measurement session the subject was scanned 7 consecutive times with an MRSI sequence with a spectral bandwidth of 1325 Hz, a resolution of $32\times32\times21$ voxels, 588/1176 (resampled) spectral points and a measurement time of 4:18 min. During the reference measurements, the subjects were not given ^{2}H labeled glucose prior to the measurement session, thus Glx concentrations in the brain were expected to be constant over the entire measurement session. Apart from the usual fluctuations in the brain, tNAA and Glx concentrations were assumed to be constant over time. Between the MRSI sequence blocks, an autoalign sequence was applied to reposition the VOI to compensate for movements during the measurement. The stability of the results was evaluated afterwards with the CV and by using linear regression to estimate the trend in tNAA and Glx

concentrations over time. Concentrations were compared and analysed with the CV over all repetitions both voxelwise and averaged over the whole slice. The voxelwise comparison and the CV is important for mapping of Glx concentrations as it gives information on how reliable high resolution maps of concentrations can be created from the MRSI data. The slicewise averaged data is indicative for the overall temporal stability in metabolite concentrations over time as the spatial information is lost but large scale trends are more visible when averaged over local fluctuations. In particular the stability of the Glx4 signal was independently analysed to see how well the signal can be identified compared to the non-deuterated groups of Glx.

3.7.2 Measurement sessions using ^{2}H labeled glucose

To see the metabolic behaviour in the brain after ingestion of a deuterated [6,6'-2H2]-glucose substrate, 5 subjects were scanned after having ingested a deuterated glucose substrate. These subjects were scanned 14 consecutive times with an MRSI sequence with a spectral bandwidth of 1325 Hz, a resolution of $32 \times 32 \times 21$ voxels, 588/1176 (resampled) spectral points and a measurement time of 4:18 min. During the MRSI sequence, a Navigator sequence [9] was used to detect head movements in real time. The VOI was then continuously updated according to the Navigator scans to follow the head position changes. As the signal amplitude of the Glx4 signals were declining over time, Glx concentrations extracted by LCModel were modeled using linear regression to see how distinctive the variation in concentrations over the whole measurement session would be. These linear fits of concentrations over time were applied both voxelwise to map local variances in metabolic rate as well as on the slicewise averaged concentrations. These two approaches can be used to detect the overall decrease in concentrations as well as local differences, for example between white matter and grey matter.

3.7.3 Stability of a constant lactate signal

Lactate can also be labeled and quantified by using DMI. However, before applying the method in clinical studies with patients, the detection capability and stability of lactate signals in the brain with the MRSI sequence was evaluated with a simulated lactate signal. A constant lactate signal (Fig 3.6) was simulated and added to the in vivo spectra of the reference measurements in every voxel in the VOI. Then, LCModel was able to fit the spectrum with the added lactate signal. Unlike in the reference measurements and the DMI measurements, the fitting range was increased to 1 ppm to 4.2 ppm with an additional fitting range between 7 ppm and 8 ppm for the inverted reference lactate signal. Afterwards, the lactate concentrations extracted by LCModel were analysed and the stability was evaluated with the CV. Further, the lactate concentrations over time were modeled using linear regression. As the simulated signal is constant, little to

no variation in concentration should be detected over time.

3.7.4 Detection capability of a decaying lactate signal

Not only do the lactate concentrations have to be consistent when the simulated lactate signal is constant, a decaying lactate signal, as it would be measured in dynamic DMI in a cancer patients brain, has to be detectable as well. For this goal, a lactate signal at 1.31 ppm with decreasing strength was simulated into the spectra of measurement data with 7 repetitions. As the decay rate with which the signal is decaying is known, we can compare it afterwards with the average decay rate of the extracted concentrations. The lactate signal in Fig. 3.4 was scaled to be as strong as the average tNAA signal in the brain for the first repetition and every other repetition the scaling was reduced by 15%. As the simulated signal becomes weaker, the FWHM of the resonance peak increases and the quality of the metabolic maps decreases accordingly. The goal of this experiment was to determine up to which simulated concentration the lactate signal can be reliably detected and fitted by LCModel.

3.7.5 Fitting of simulated lactate signals in subtraction spectra

Additionally to fitting the decaying lactate signal directly from the spectra, they were fitted from the subtraction spectra as well. The subtraction spectra were generated during the reconstruction process of the same data sets as the ones used in 3.7.4 to allow for a direct comparison of the fitting quality. This means that the simulated lactate signal decay rate as well as the initial lactate signal strength are the same as in 3.7.4.

Chapter 4

Results

For the evaluation of the stability, a quality control mask was used to exclude certain voxels that have either insufficient SNR or a FWHM that is too broad to contain the signal in the voxel in k-space. Voxels were removed mostly in the lower frontal lobe of the brain above the nasal cavity and along the border of the skull where unwanted artifacts lead to low SNR and higher fluctuations. The slices selected for the analysis can be seen in Fig. 4.1. The lowest slice is slice number 7 while the highest slice is number 14. Concentrations in voxels below slice 7 and above slice 14 are more affected by unwanted artifacts which is why they were not taken into consideration. On average about 55-60% of the voxels have been taken into consideration for the analysis.

Section 4.1 contains the results of the stability of the reference measurement sessions with the MRSI sequence used without ingestion of any substrate. Stability of Glx and tNAA concentrations were analysed by comparing the metabolic maps for every repeated measurement. This reflects the MRSI sequence's ability to reliably quantify assumed constant concentrations with a high spatial resolution. After having shown the temporal and spatial stability of the MRSI sequence, it was used for the ^{1}H-DMI measurement sequence for which the results can be found in Section 4.2. The measurement sessions have taken place after the ingestion of deuterated glucose and the 3D-FID-MRSI sequence was the method used to image and quantify the deuterated Glx concentrations. Lastly, in Section 4.3 we will analyse the stability of the simulated lactate signal as well as the detection capability of the software for different simulated lactate signal strengths.

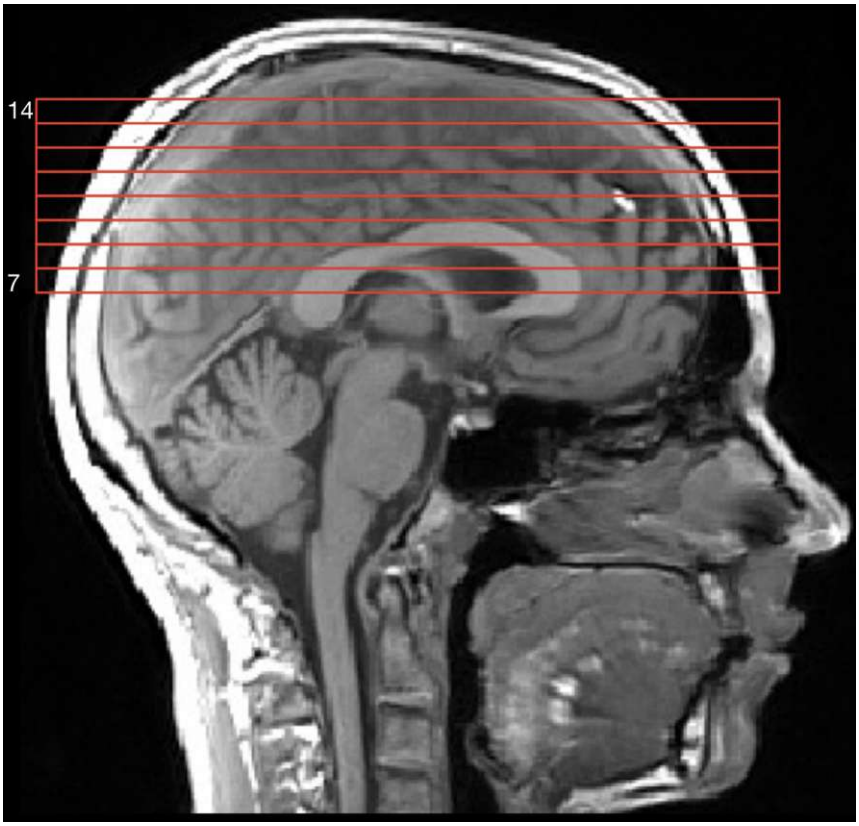

Figure 4.1: T1-weighted image of the brain in the sagittal plane with the size and position of slices 7 to 14 in the brain.

4.1 Reference measurements with the MRSI sequence

In the reference measurement sessions the MRSI sequence's ability to consistently detect quasi constant concentrations of metabolites in a healthy subject's brain was tested. The coefficients of variation of the concentrations of a metabolite over all measurement sequence repetitions were analysed both voxelwise and averaged over an entire slice. On the one hand, a voxelwise analysis gives more insight into the spatial stability of the measurement sequence. Assuming a perfectly still brain, this can give information on how well the signal can be localised in a single voxel in repeated measurements. On the other hand averaging concentrations over an entire slice will neglect local fluctuations of metabolite concentrations which gives more information about the overall trend in concentrations over time.

To improve the spatial resolution, an autoalign sequence was applied before every MRSI sequence repetition. The measured volume is thus realigned with a T1-weighted map of the brain before every MRSI sequence to compensate for movements of the head between the measurement sequence repetitions. However, during the measurement sequence no real-time motion correction algorithms were used and thus small movements of the head have lead to stronger fluctuations in single voxels as the precise localisation of the signals has become more difficult. This can explain the increased voxelwise CV for certain metabolites shown in Table 4.1.

Taking a closer look at the voxelwise stability, we have the voxelwise CV of tNAA and Glx concentrations mapped in four central slices of one subject's brain in Fig. 4.2. This is further quantified in Fig. 4.3. where the CV's in every slice are averaged over the whole slice. This was done for all 5 subjects of the reference measurements with the CV's of tNAA, Glx and Glx4 concentrations. In order to see how consistently the Glx4 signal can be detected, it was separated from the Glx signal and measured independently. In Fig. 4.3. we can see that the Glx4 signal has a slightly higher voxelwise CV than the Glx signal.

The CV of slicewise concentrations averaged over the VOI for different metabolites for every subject can be found in Table 4.2. The concentrations of tNAA and Glx in 5 different test subjects were consistently in the same concentration range with the CV of tNAA being on average per slice around 3% while the CV of Glx being around 4% and the CV of Glx4 is slightly higher at about 4.5%.

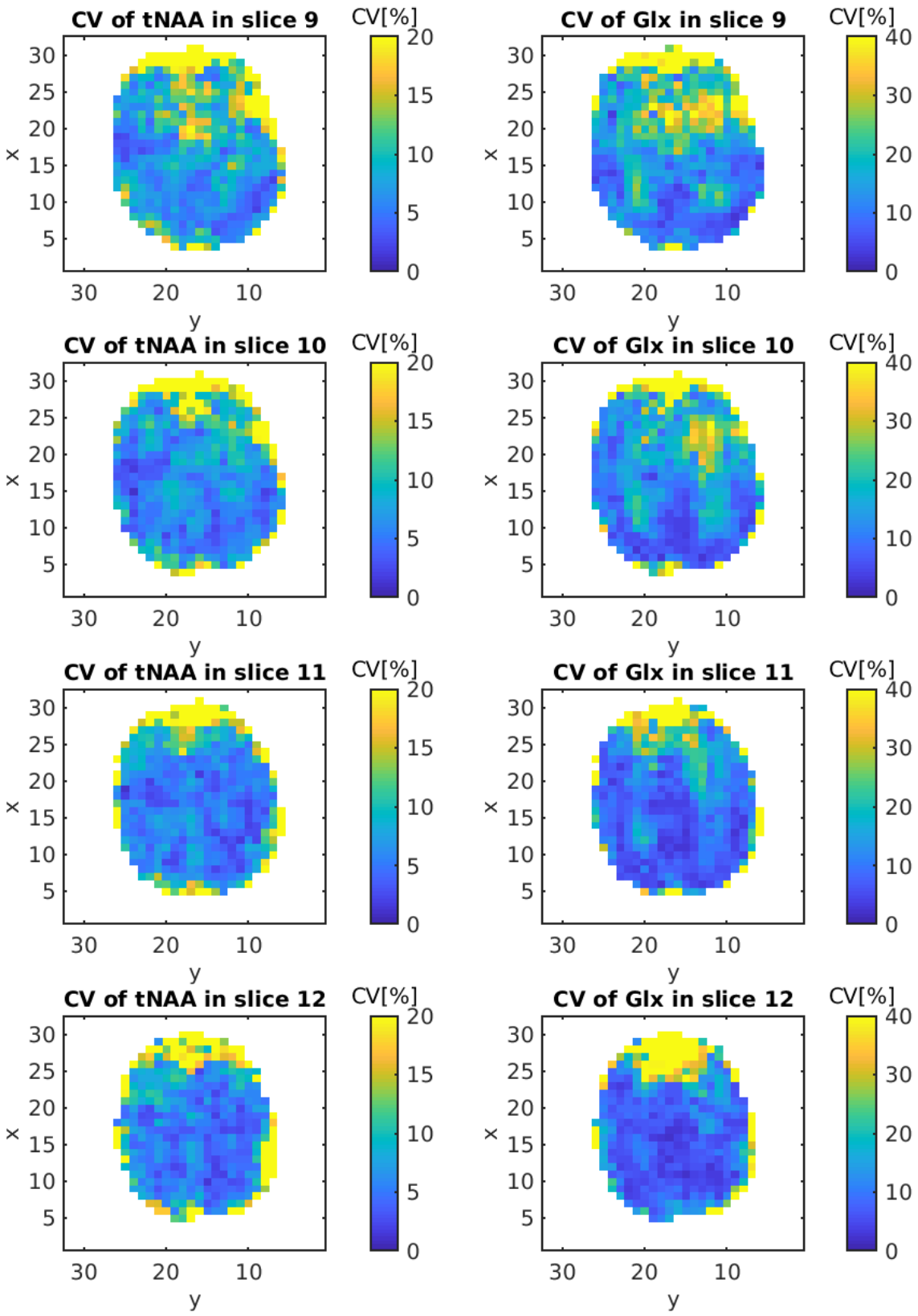

Figure 4.2: Voxelwise CV of tNAA and of Glx in four transversal slices in the central region of one subject's brain.

Subject	CV of tNAA [%]	CV of Glx [%]	CV of Glx4 [%]
1	7.33 ± 0.73	11.19 ± 0.84	16.27 ± 1.67
2	5.65 ± 1.32	10.11 ± 2.33	13.27 ± 3.17
3	10.21 ± 0.79	16.85 ± 1.96	19.15 ± 2.34
4	7.90 ± 1.39	11.95 ± 0.97	14.97 ± 1.12
5	8.39 ± 0.75	13.89 ± 1.69	18.56 ± 2.46

Table 4.1: Voxelwise CV averaged over all slices 7 to 14 (Fig 4.1).

Subject	CV of tNAA [%]	CV of Glx [%]	CV of Glx4 [%]
1	3.21 ± 0.41	4.48 ± 0.91	5.22 ± 0.71
2	3.56 ± 0.59	4.12 ± 1.06	4.28 ± 1.08
3	3.05 ± 0.62	3.80 ± 0.82	5.06 ± 0.80
4	2.71 ± 0.52	3.19 ± 0.48	3.69 ± 0.69
5	3.14 ± 0.51	4.04 ± 0.55	4.49 ± 0.66

Table 4.2: Slicewise averaged CV averaged over all slices 7 to 14 (Fig 4.1).

The average CV of all subjects of the concentrations of Glx/Glx4 averaged over a slice is 3.92%/4.54% and the voxelwise CV of Glx/Glx4 is on average 12.79%/16.44%. Thus, the CV of concentrations averaged over the slice of Glx4 is on average 11.58% higher than the CV of Glx and the voxelwise CV of Glx4 is 28.53% higher than the voxelwise CV of Glx.

The high voxelwise CV of Glx and Glx4 is due to local variations in metabolic activity and the lack of a real-time motion correction algorithm like the Navigator during the measurement session. This reduces the MRSI sequence's ability to localise signals with such high resolution. As these reference measurements were made prior to the DMI measurements, the Navigator was not yet ready to be implemented in the reference measurement session. As we will see in the next part, the Navigator [9] was able to further reduce the CV and thus increase the voxelwise stability during the DMI measurements.

To quantify the trend in concentrations over all repetitions, a linear fit function was used in every voxel. The linear coefficient of the fit function is mapped in voxels in slices of the brain for tNAA and Glx in Fig. 4.4 and Fig. 4.5 respectively. For quantification of the quality of the linear fit, statistical indicators such as the P-value and the R-value are also mapped in the same slices. As these concentrations are mostly fluctuating because of noise, we would not expect them to correlate and thus slopes as well the R-values should be centered around 0. The p-values of the linear fit function for tNAA and Glx are both largely above the threshhold for statistical significance of p = 0.05, which means that the slopes in most voxels cannot be linked to an actual decay but represent normal fluctuations of metabolites in a healthy brain. Both in

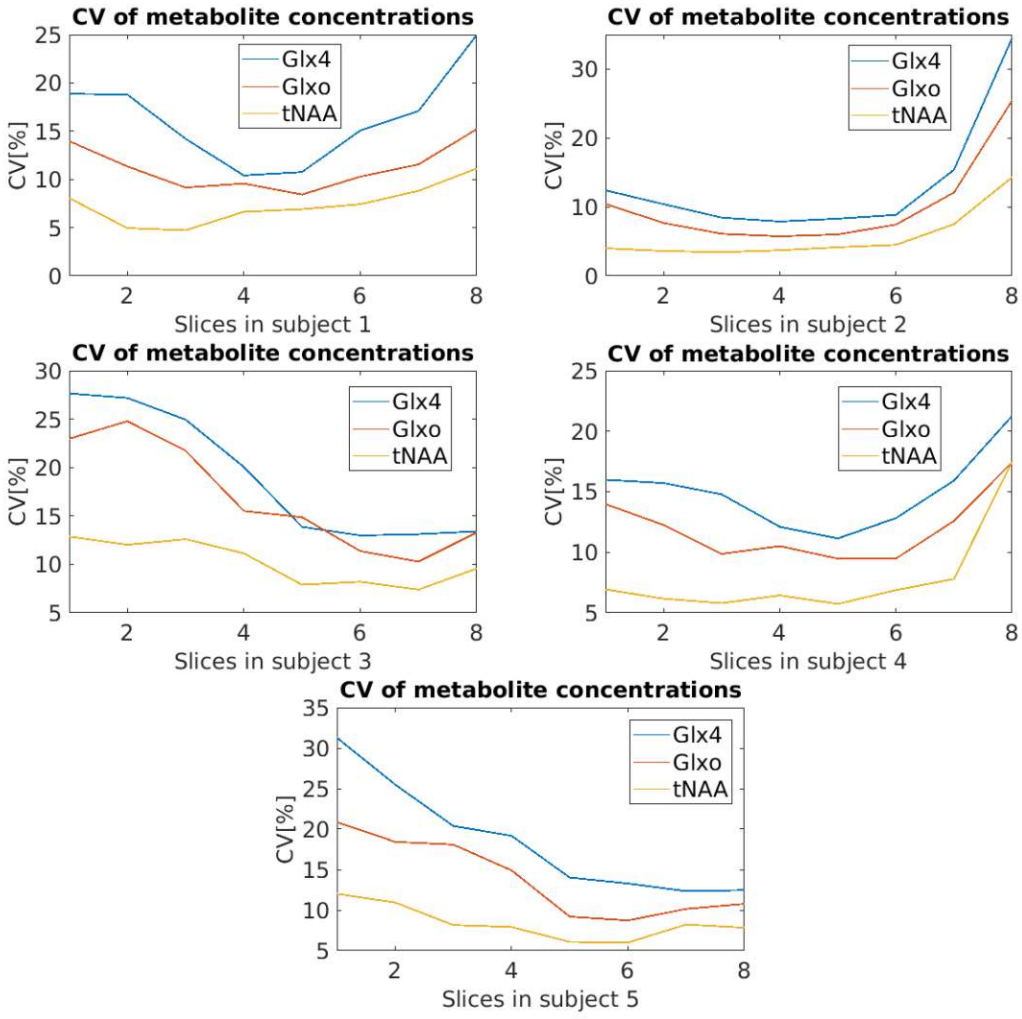

Figure 4.3: Voxelwise CVs of tNAA, Glx and Glx4 depicted in Fig. 4.2. averaged over each transversal slice in the central region of the brain from slice 7 to 14 in all 5 subjects.

Fig. 4.4 and Fig. 4.5 there is no apparent difference between GM and WM and the measured concentrations in every voxel fluctuate on the order of magnitude of μM/min, for both tNAA and Glx.

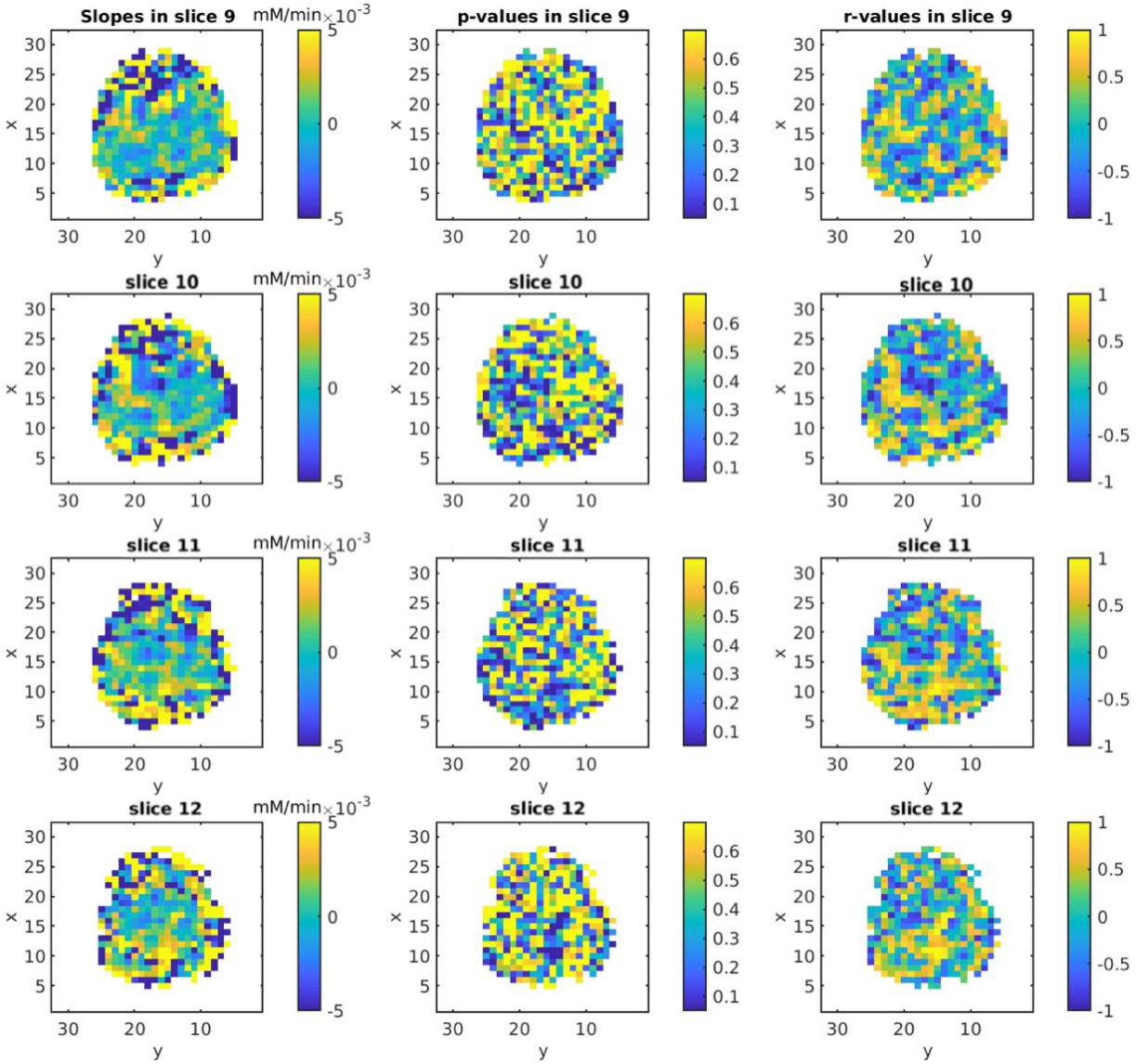

Figure 4.4: Slope of linear fit function of tNAA(left column), its P-value(center column) and its R-value(right) in all voxels of four transversal slices in the central region of one subject's brain.

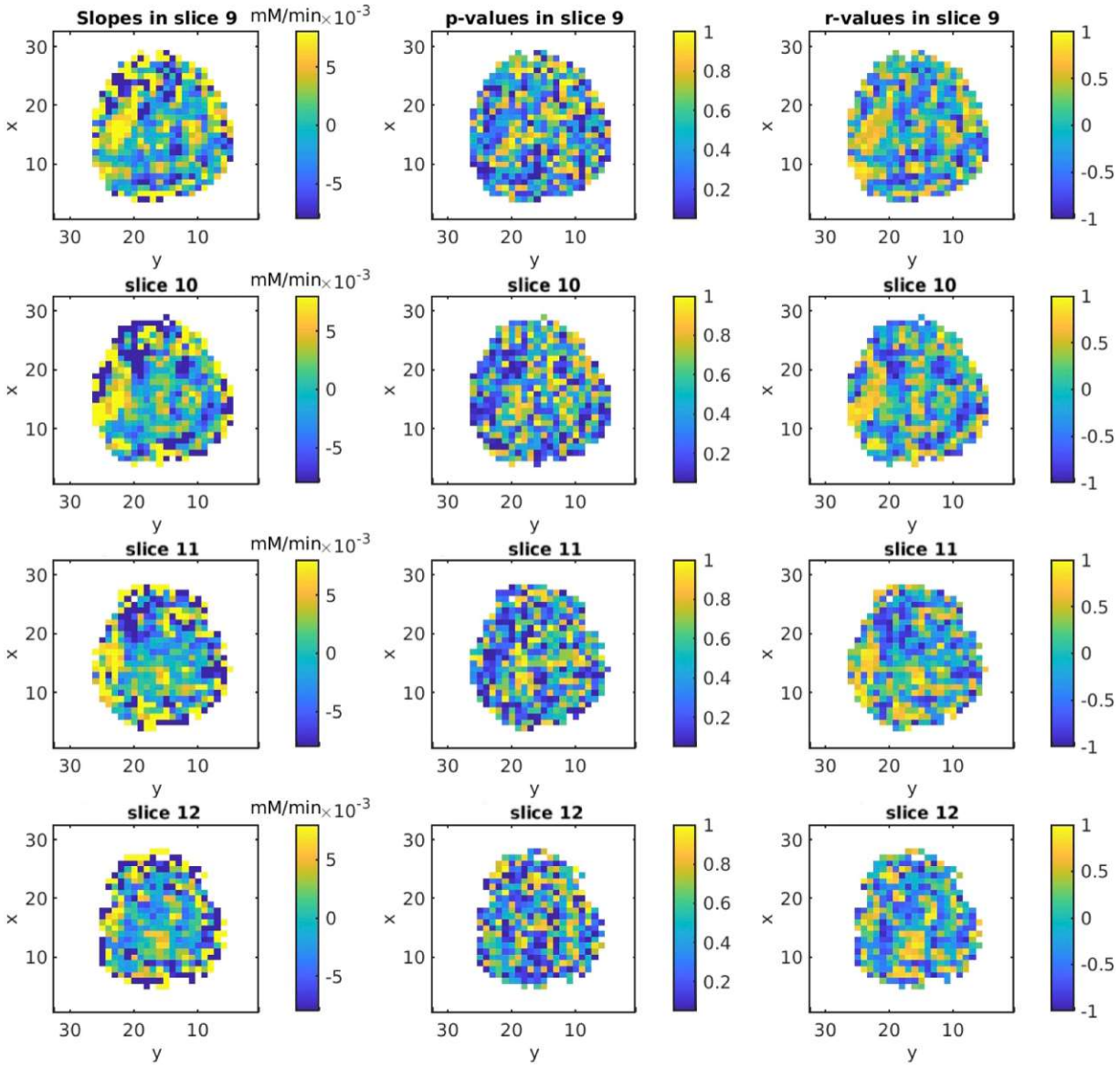

Figure 4.5: Slope of linear fit function of Glx(left), its P-value(center) and its R-value(right) in all voxels of four transversal slices in the central region of one subject's brain.

4.2 Stability of deuterium metabolic imaging results

4.2.1 Stability of tNAA concentrations

For the DMI measurements there was an increased amount of repetitions compared to the reference measurements and the vNAV sequence was used during the measurements, which allowed for a further reduction of the coefficent of variation in both voxelwise and slicewise averaged concentrations over time. Voxelwise comparison means that the concentrations of a metabolite in a same voxel are compared over all repetitions and the CV can be mapped on every voxel, which can be seen in Fig. 4.6. Compared to the reference measurements, the voxelwise CV mapped on the slices is significantly lower, which can be seen when comparing the scales of Fig. 4.2 and Fig. 4.6.

Slicewise comparison means that concentrations have been averaged over the slice for all repetitions and subsequently the CV has been taken from the set of averaged concentrations. This yields a lower CV since local fluctuations do not affect the slicewise averaged concentrations as much, however it also gives more precise information of the overall trend in concentrations and the temporal stability of the measurement sequence. The voxelwise CV can quantify the spatial stability and how consistently the acquired signal can be associated to a location in the brain. The slicewise and voxelwise CV of tNAA concentrations in all subjects can be found in Table 4.3. The CV of slicewise averaged concentrations per slice can be seen in Fig. 4.7. The CV of the concentrations of tNAA show that the results are consistently in the same concentration range with the average CV per slice in most subjects being below 2%.

The linear coefficients (slopes) of the fit function that estimate the trend of tNAA concentrations over time in a voxel along with their P-value and their R-value are mapped on the central slices of a subject's brain in Fig. 4.8. Most slopes in the brain slice are between $\pm 2 \times 10^{-1} \mu$M/min which is a decay of about 0.002% of the average tNAA concentration of 10 mM/L in the brain. The center and right column indicate the relatively low correlation with the fit function, which means that the slopes represent mostly uncorrelated fluctuations of tNAA concentrations due to noise. The distribution of tNAA slopes in slice 11 from Fig. 4.8 can be seen in Fig. 4.9.

This histogram clearly shows that the slope of tNAA concentrations, i.e. the decrease of tNAA concentrations over time, is centered around 0 with most slopes being between -4×10^{-4} and 4×10^{-4}. This confirms the results seen in the left column of Fig 4.8, showing the concentration decrease per voxel, and in the right column of Fig. 4.9 we can see that there is a

low correlation between the fit function and the concentrations, as the r-value of the function is mostly between -0.5 and 0.5 throughout all slices.

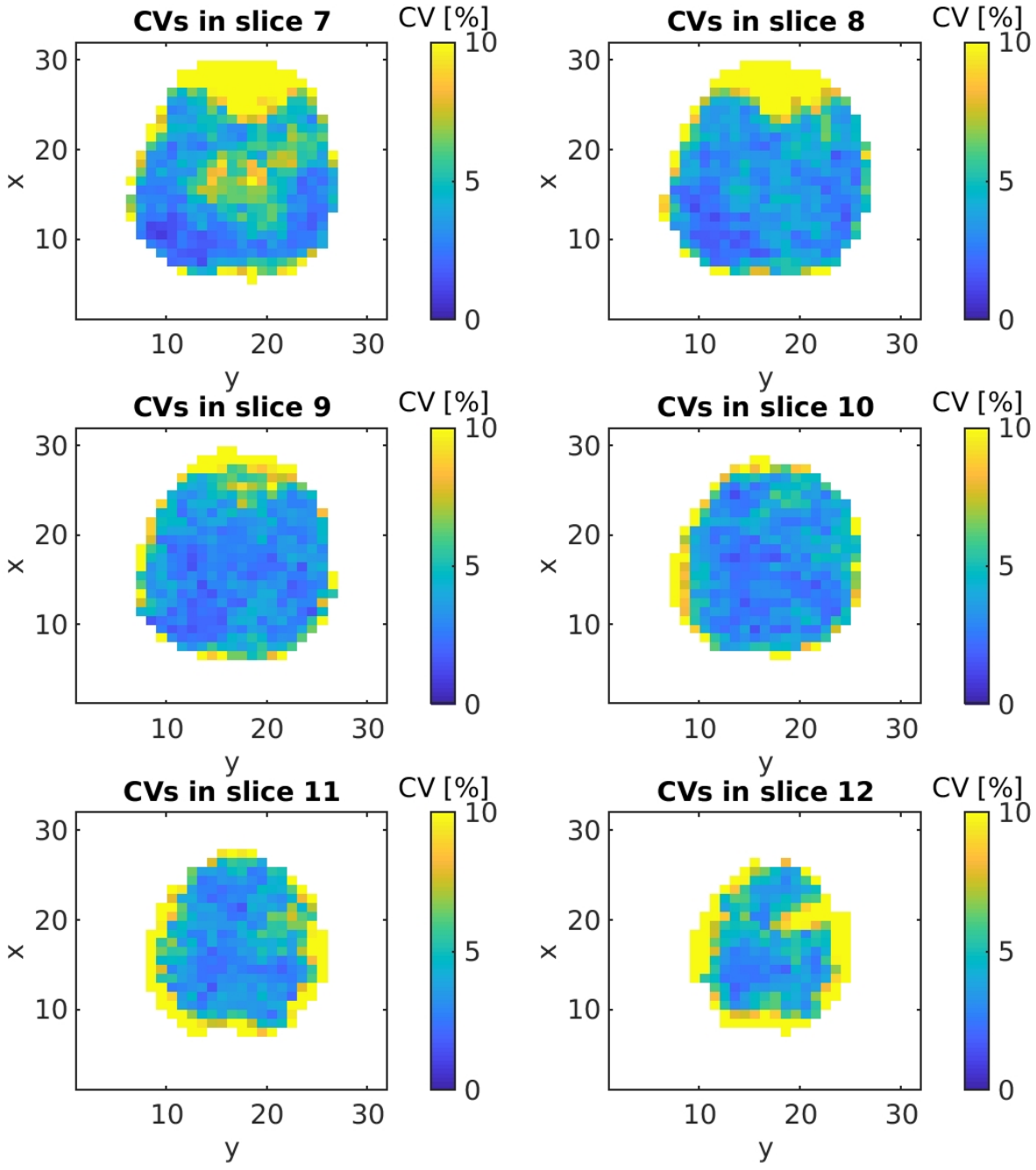

Figure 4.6: Voxelwise CV of tNAA concentrations in the central transversal slices of the brain of a subjects during the DMI measurements with 14 repetitions and with the Navigator correction algorithm turned on. Notice the scale compared to Fig. 4.2 which is halfed, which means that the range of CV throughout the slice is significantly lower, indicating a substantially increase of spatial stability with the Navigator sequence.

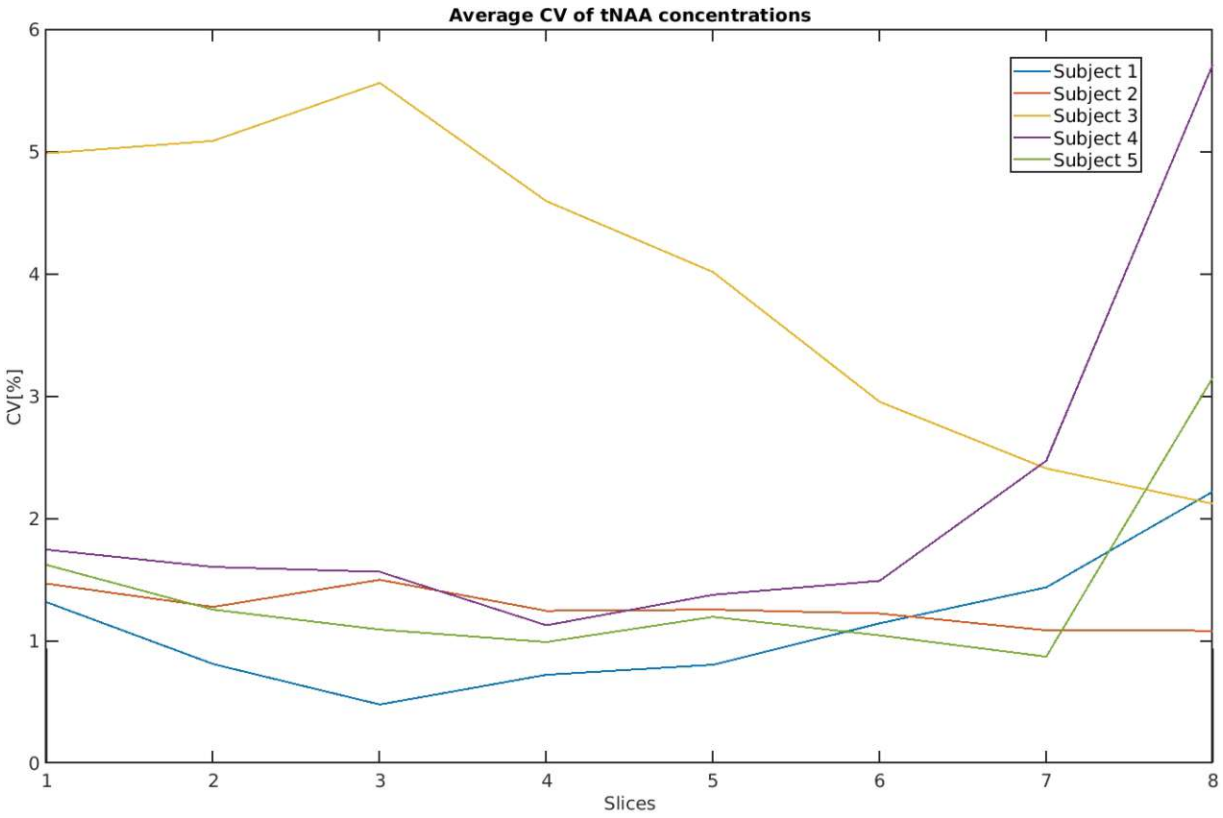

Figure 4.7: CV of tNAA concentrations that were averaged over the transversal slices 7 to 14 in all 5 subjects. The increased average CV for subject 3 can be explained by a possible malfunction of the vNav sequence or increased agitation of the subject during the measurements session, as the slicewise CV is in the order of magnitude of the CV in the reference measurements (Table 4.2), where no vNav sequence was used.

Subject	Slicewise CV [%]	Voxelwise CV [%]
Subject 1	1.12 ± 0.19	2.87 ± 0.61
Subject 2	1.27 ± 0.15	4.69 ± 0.97
Subject 3	3.51 ± 0.46	4.35 ± 1.55
Subject 4	2.14 ± 0.52	4.04 ± 0.77
Subject 5	1.40 ± 0.26	4.18 ± 0.71

Table 4.3: CV of tNAA concentrations averaged over a slice and voxelwise over 14 repetitions averaged over all slices 7 to 14 (Fig 4.1) in all subjects.

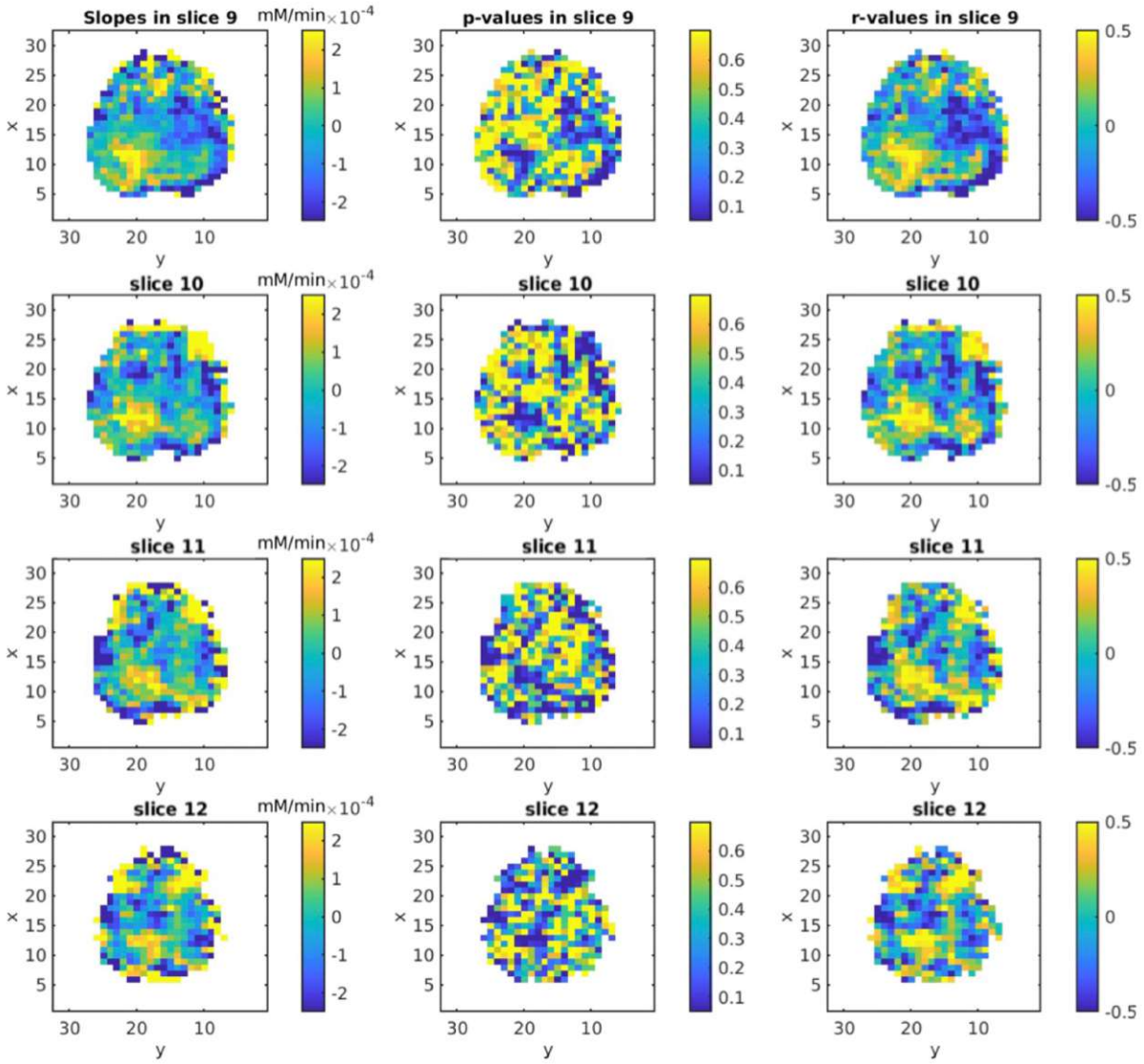

Figure 4.8: Slope of linear fit function of tNAA concentrations, its P-value and its R-value in all voxels of slices in the central region of one subject's brain.

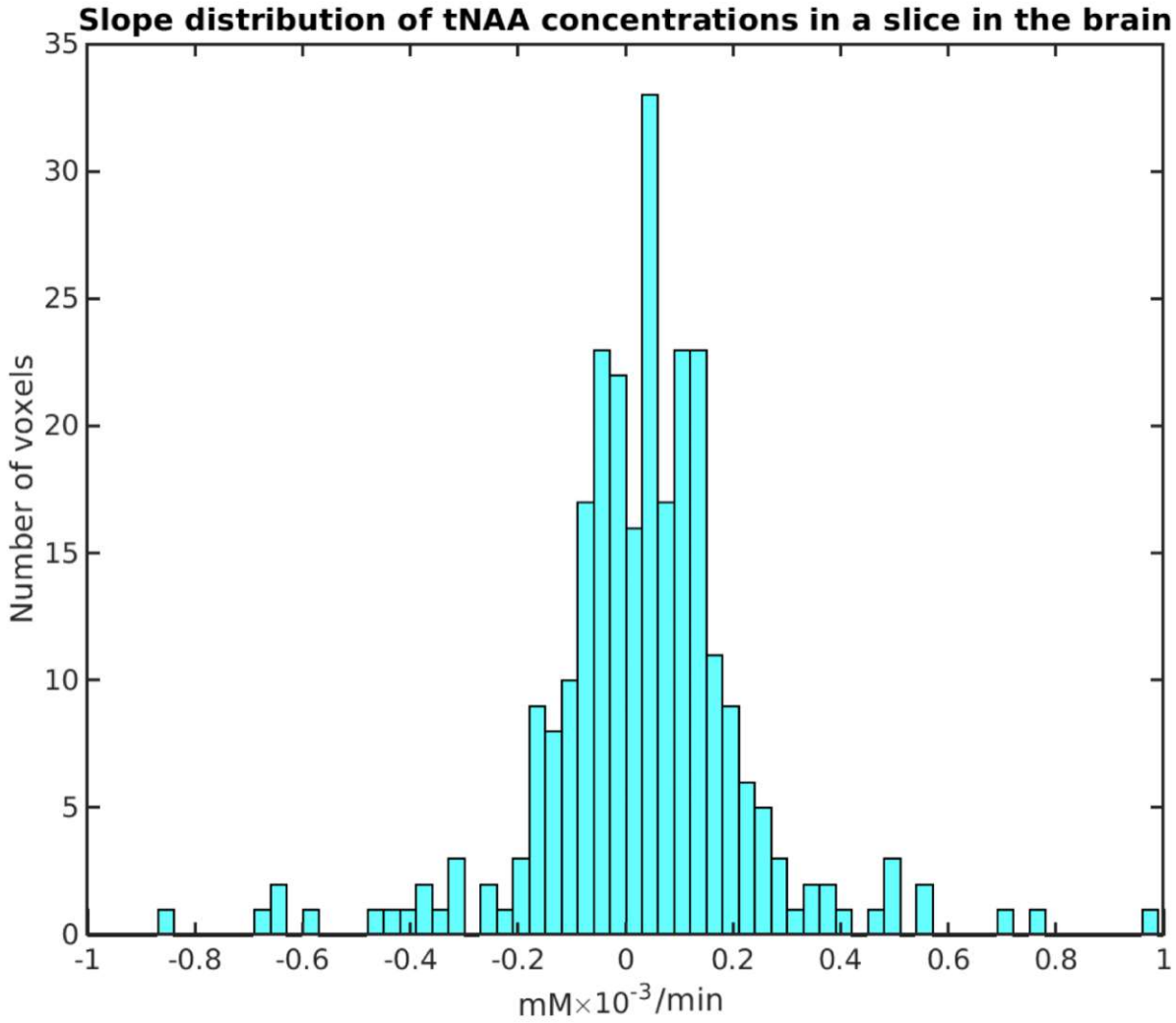

Figure 4.9: Distribution of the calculated tNAA concentration decay rates in all voxels in a central transversal slice of the brain.

4.2.2 Variation of Glx concentrations

After having shown that the measurement sequence can deliver consistent results for constant concentrations, we will further inspect the Glx concentrations which have been deuterated and are thus decreasing over time. A starting concentration for Glx of 10 mM/L was assumed, with the starting concentration of Glu being 8mM and the starting concentration of Gln being 2mM, which are standard concentrations in a healthy brain[27].

Comparison of a slice in the brain at the beginning of the measurement and after the 14th repetition show that the measured concentrations of Glx are significantly lower at the end of the session. These metabolic maps along with T1-weighted maps of a brain slice can be seen in Fig. 4.10. In Fig. 4.11 we can see the slopes of the linear fit functions describing the decay of non-labeled Glx concentrations in slices of one subject's brain in mM/min on the left and the ^2H-labeled Glx concentrations on the right. The slope of the linear function that describes the trend of the ^2H-labeled Glx concentration in a single voxel over time shows a clear decline throughout most of the slice. A comparison of the slopes in WM and GM can be found in Fig. 4.12. The slope distribution of ^2H-labeled Glx concentrations in slice 11 from Fig. 4.11 is represented by the histogram in Fig. 4.13, which clearly shows the overall negative tendency of ^2H-labeled Glx concentration decay being centered at around -0.05 mM/min. The slopes in voxels in WM are less steep than the slopes in GM and in slices located higher we have an overall stronger decrease in Glx concentrations.

To put these slopes into perspective, Fig 4.14 and Fig. 4.15 show the ^2H-labeled Glx concentrations averaged over the VOI for every repetition of the measurement sequence for every subject in WM and GM respectively. Using linear regression, the decrease in Glx concentrations was estimated with the slope of the fit function. As we can see, the average concentrations of deuterated Glx over the entire VOI are declining for all 5 subjects with GM showing a stronger decline of ^2H-labeled Glx signal than WM. The slopes in voxels in WM over the VOI are on average 39.4$\pm$8.5% less than in voxels in GM.

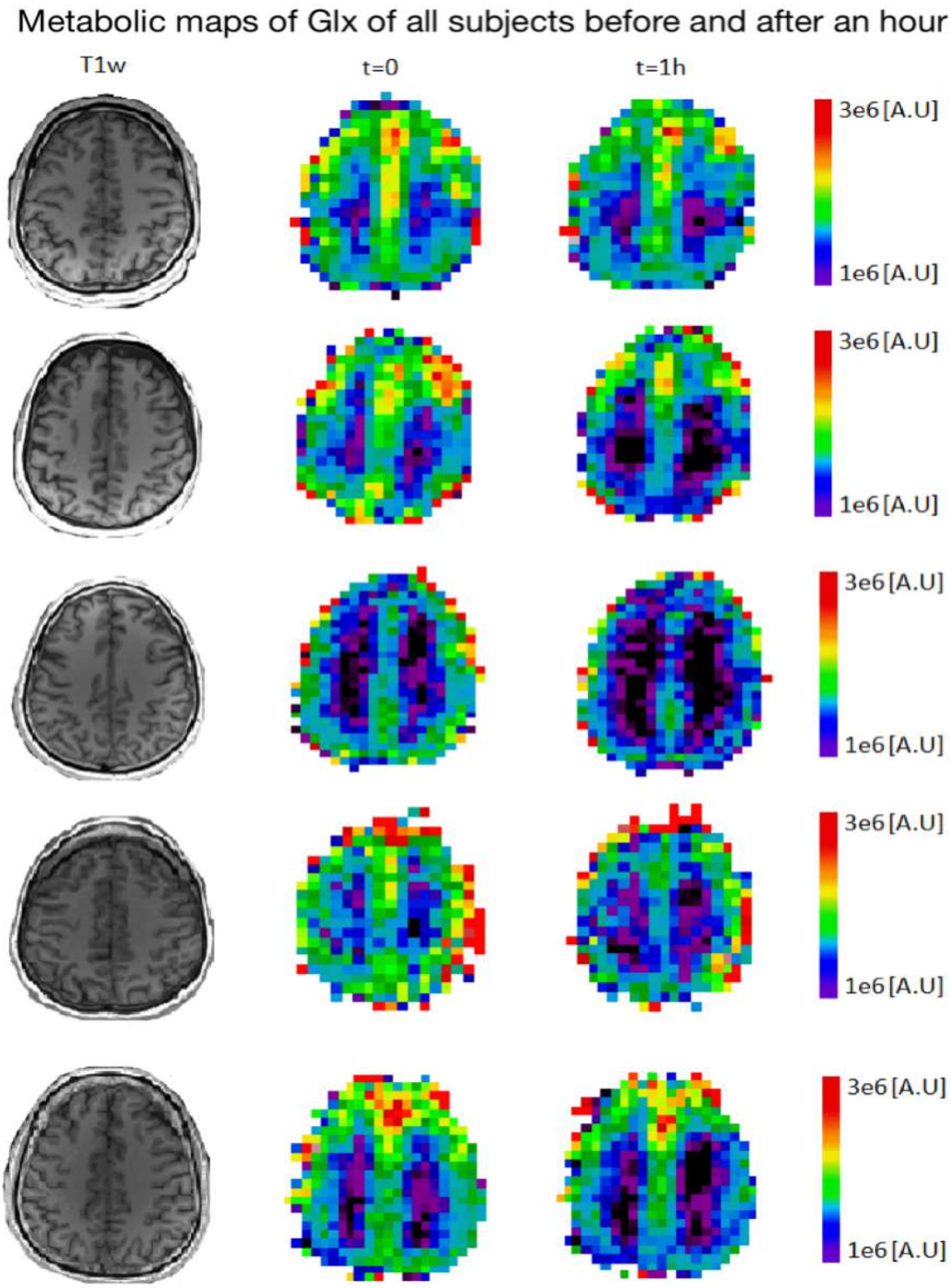

Figure 4.10: T1-weighted image and metabolic maps of ^{2}H labeled Glx of all subjects (1 to 5 from top to bottom) at the beginning of the measurement session and at the end of the measurement session.

In all subjects the ^2H-labeled Glx concentration show a steady decrease over the measurement session with the least decrease in WM being -7.83% and the strongest decrease in WM being -15.10% from the starting concentration. The average decrease of concentrations averaged over WM in the VOI is $-10.13\% \pm 1.36\%$. In GM the average Glx concentration decay in the VOI ranges from -10.84% to -23.4% with the average decrease being $-14.18\% \pm 2.35\%$. This means that the deuterated glucose substrate has been metabolized into Glu and Gln which translates in the decrease of Glx concentrations. On average, the metabolic rate i.e. the slope of Glx concentrations in the higher slices of the brain are higher then in the lower slices and Glx concentration decay is increased in GM compared to WM. Further, same subjects have similar metabolic rates in different slices of the brain, which means that subjects with high metabolic rate in the lower slices also tend to have a high metabolic rate in the upper slices. The decay rate of Glx concentrations averaged over the VOI as well as the concentration decrease after one hour in WM and GM can be found in Table 4.4 and Table 4.5 respectively.

To put the concentrations of ^2H-labeled Glx over time further into perspective, the average ratio of ^2H-labeled concentrations ([Glx]) to tNAA concentrations ([tNAA]) of all subjects over all repetitions can be seen in Fig. 4.15. As tNAA concentrations were very consistent throughout the DMI measurements, the ratio of decaying Glx concentrations to tNAA concentrations emphasizes the decay further than the Glx concentrations by themselves and does not require any assumptions on the absolute concentrations in the brain, even though they were assumed to have on average the same concentration in the beginning. The ratio of [Glx]:[tNAA] at the beginning of the measurement session compared to the ratio at the end shows that concentrations of Glx have decreased by an average of 20% compared to concentrations of tNAA which is clearly below the normal fluctuation of concentrations quantified by the CV. The ratio of Glx concentrations to tNAA concentrations at every repetition of the measurement sequence during the measurement session can be seen in Table 4.6.

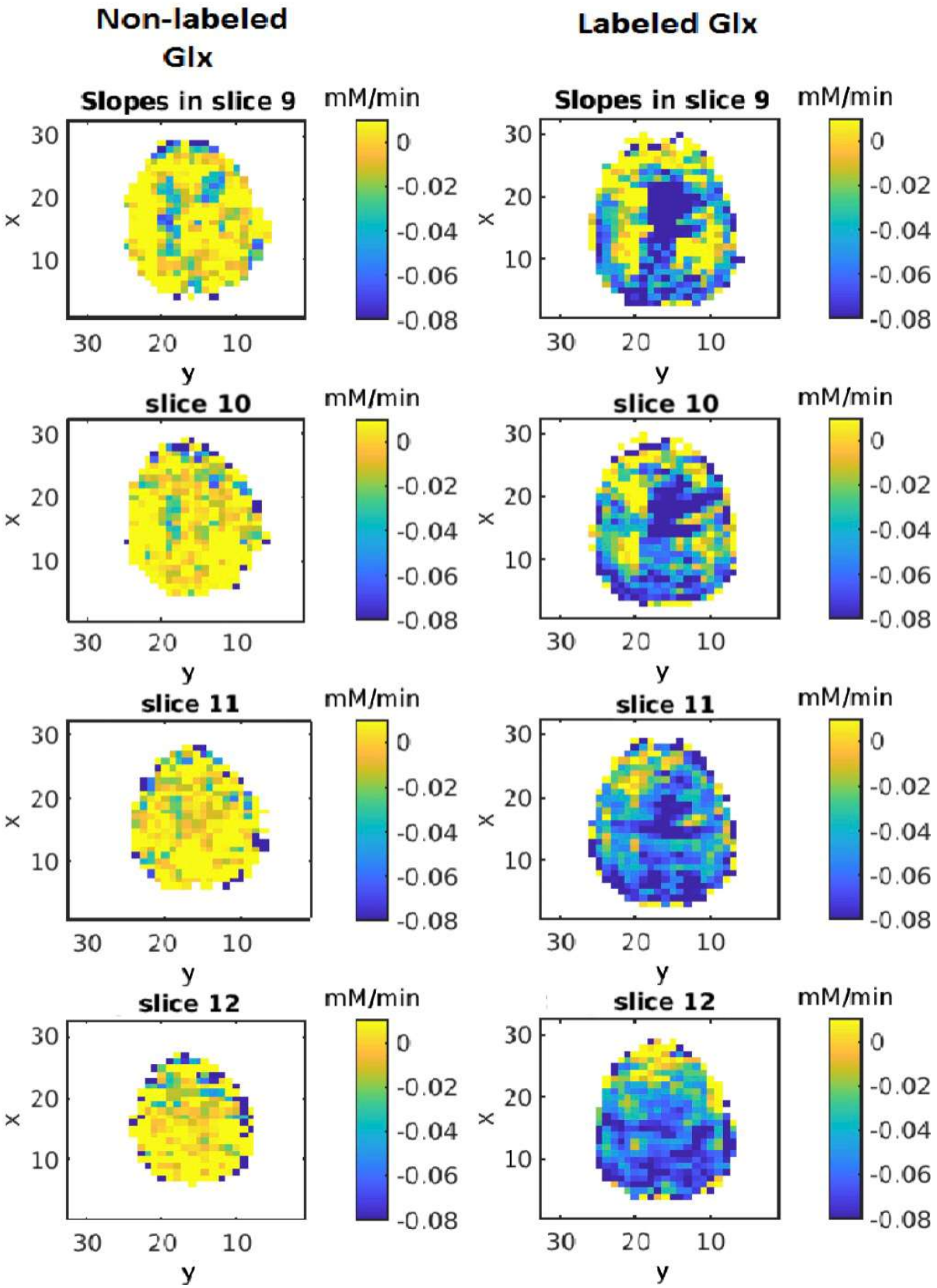

Figure 4.11: Slope of linear fit function of non-labeled Glx (left) and ^2H-labeled Glx4 (right) concentrations in all voxels of slices in the central region of one subject's brain.

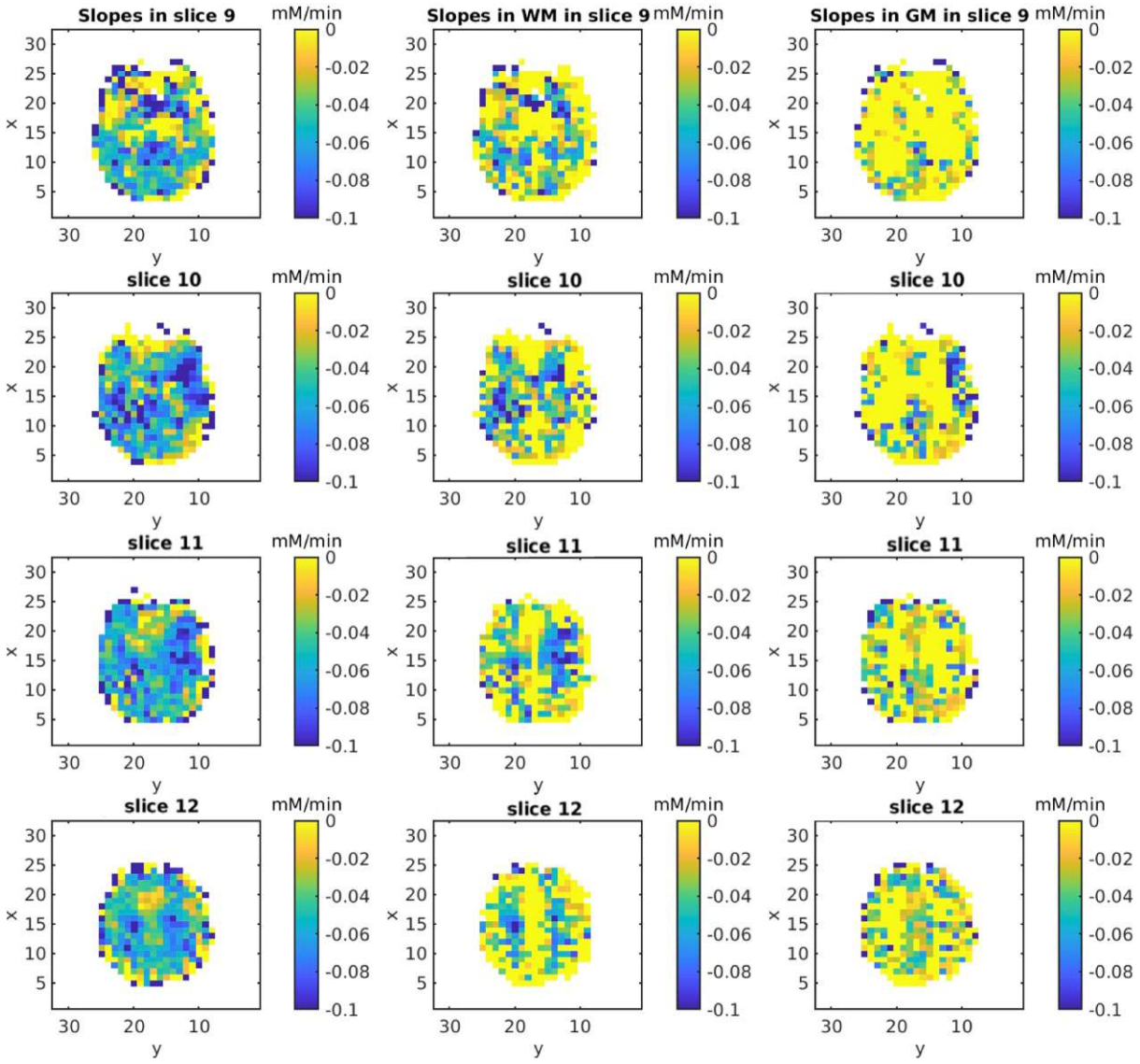

Figure 4.12: Slope of linear fits of Glx4 concentrations over time in entire transversal slices (left) and with non-zero slopes only in WM (middle) and in GM (right).

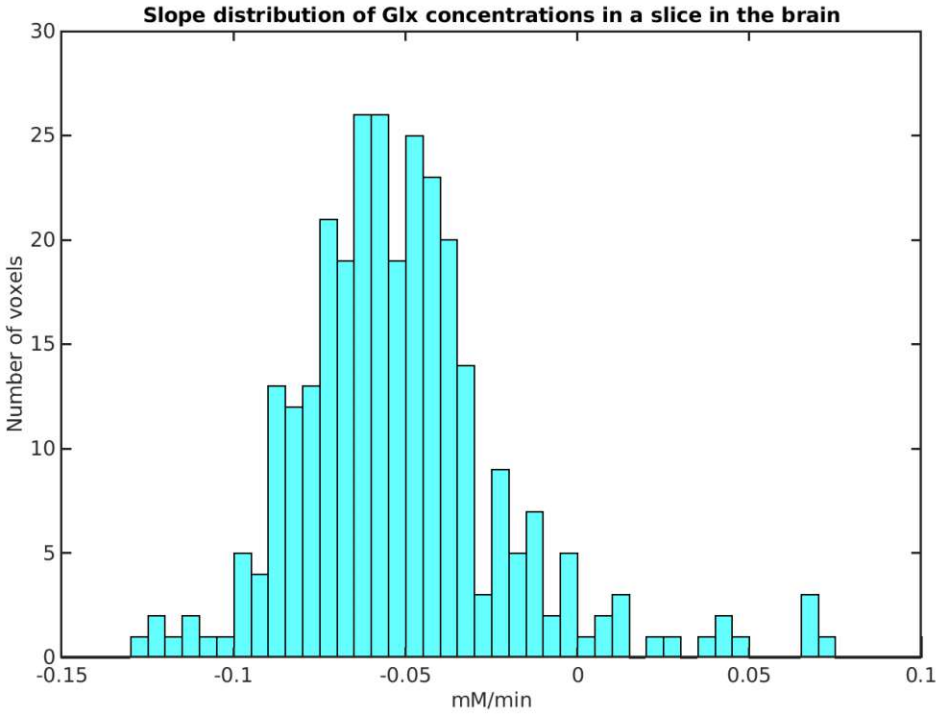

Figure 4.13: Distribution of the calculated Glx concentration decay rates in all voxels in a central transversal slice of the brain. Note the different range of decay rates compared to the decay rates of tNAA in Fig. 4.9.

Subject	Average slope in WM [mM/min]	Δ [%/h]	Δ [mM/h]
Subject 1	-0.015	-9.03	-0.903
Subject 2	-0.013	-7.83	-0.783
Subject 3	-0.018	-10.84	-1.084
Subject 4	-0.025	-15.10	-1.505
Subject 5	-0.013	-7.83	-0.783

Table 4.4: Decrease of Glx concentrations in all subjects on average in WM the VOI per min and over the full 1 hour session in absolute concentrations in mM/L and in relative concentrations in %.

Subject	Average slope in GM [mM/min]	Δ [%/h]	Δ [mM/h]
Subject 1	-0.018	-10.84	-1.084
Subject 2	-0.018	-10.84	-1.084
Subject 3	-0.022	-13.24	-1.324
Subject 4	-0.039	-23.4	-2.348
Subject 5	-0.021	-12.6	-1.264

Table 4.5: Decrease of Glx concentrations in all subjects on average in GM the VOI per min and over the full 1 hour session in absolute concentrations in mM/L and in relative concentrations in %.

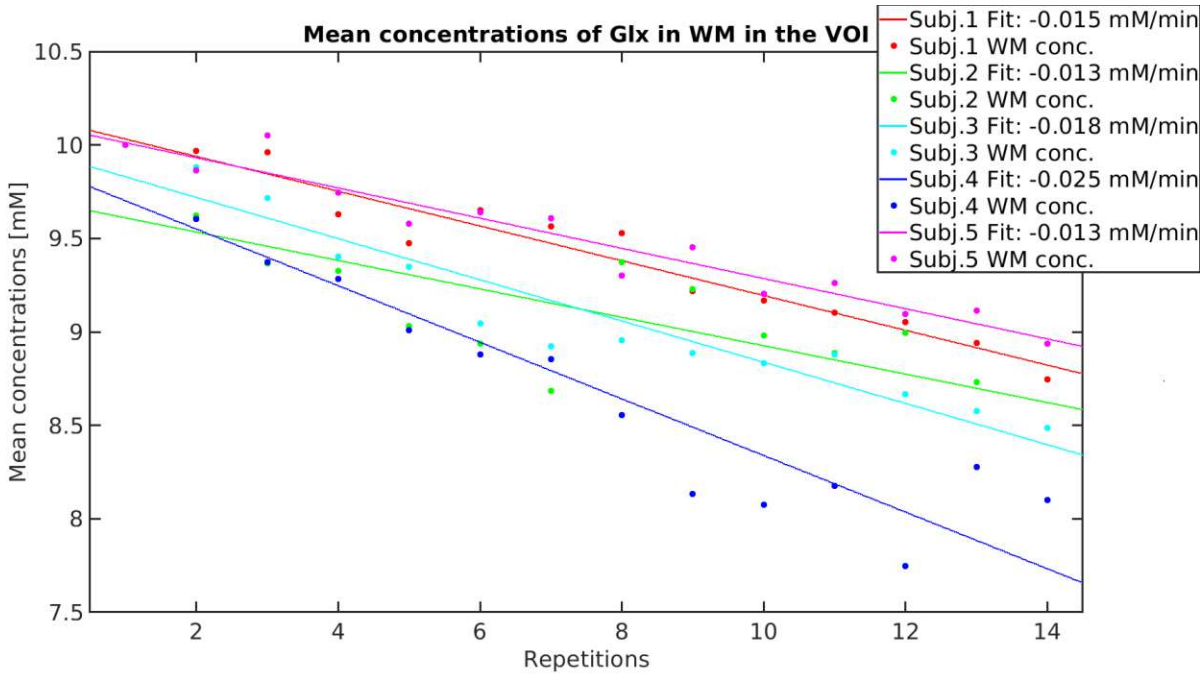

Figure 4.14: Concentrations of Glx in WM averaged over the VOI for every repetition in all 5 subjects.

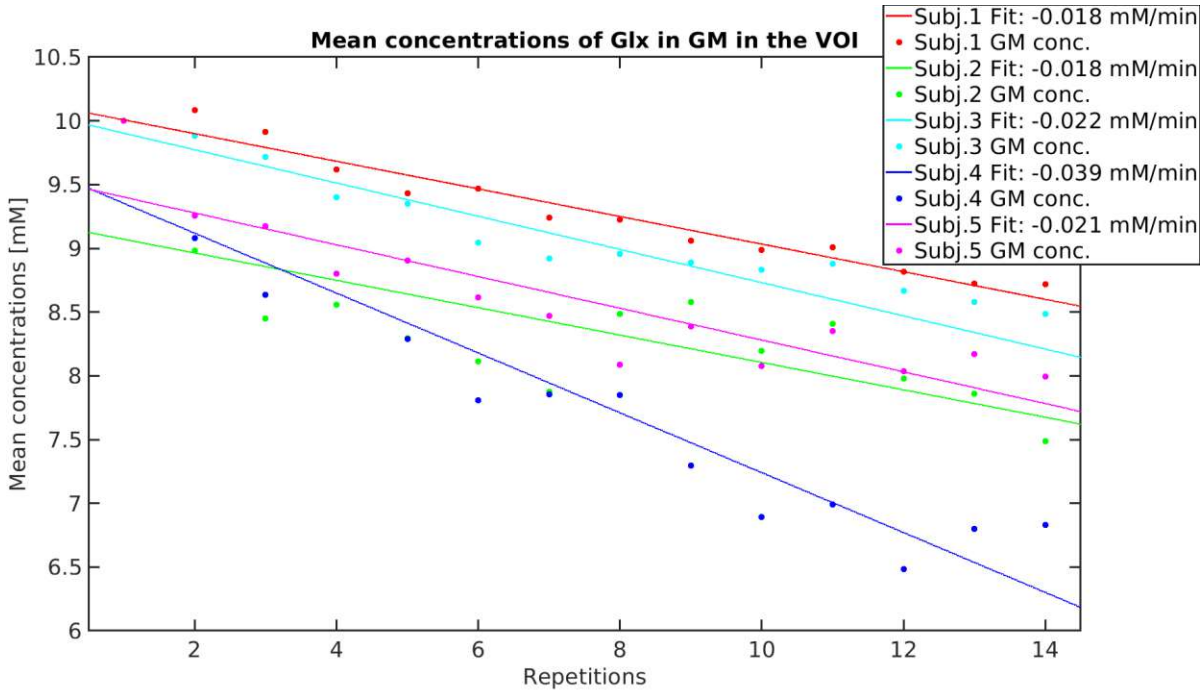

Figure 4.15: Concentrations of Glx in GM averaged over the VOI for every repetition in all 5 subjects.

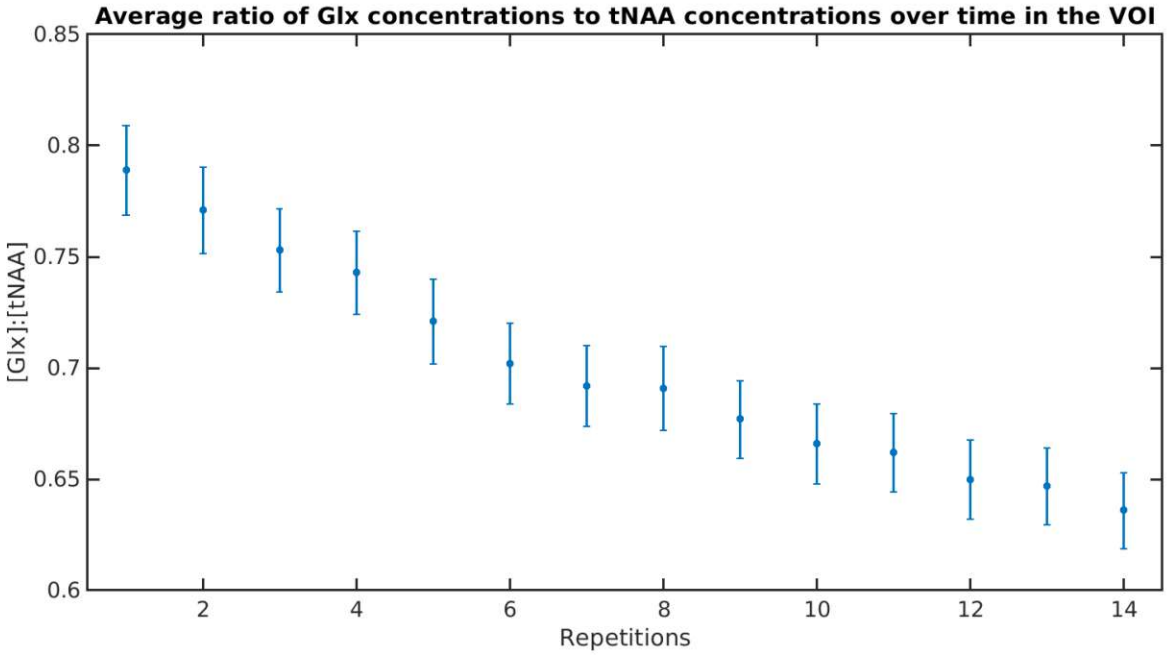

Figure 4.16: Average ratio of Glx to tNAA in the VOI averaged over all subjects (Table 4.6).

[Glx]:[tNAA]	0.789	0.771	0.753	0.743	0.721	0.702	0.692
σ	0.075	0.073	0.070	0.070	0.071	0.068	0.068
t[min]	4.3	8.6	12.9	17.2	21.5	25.8	30.1
[Glx]:[tNAA]	0.691	0.677	0.666	0.662	0.650	0.647	0.636
σ	0.071	0.065	0.067	0.066	0.066	0.065	0.064
t[min]	34.4	38.7	43	47.3	51.6	55.9	60.2

Table 4.6: Ratio of Glx to tNAA concentrations and its standard deviation σ averaged over the VOI of all subjects at equidistant timepoints over an hour which correspond to the data plotted in Fig. 4.16.

Slice	Lac signal strength	7	8	9	10	11	12	13	14	Mean over VOI
CV [%]	200% of tNAA	1.41	1.06	0.91	0.94	1.07	1.24	0.90	1.39	1.24±0.14
CV [%]	100% of tNAA	2.47	2.19	2.67	3.98	4.20	4.46	4.80	4.38	3.64±0.36

Table 4.7: Slicewise CV for different Lac signal strengths.

Slice	Lac signal strength	7	8	9	10	11	12	13	14	Mean over VOI
CV [%]	200% of tNAA	1.46	1.44	1.45	1.46	1.41	1.48	1.55	1.66	1.48±0.03
CV [%]	100% of tNAA	5.17	4.82	5.13	5.90	5.54	6.62	6.76	6.26	5.77±0.26

Table 4.8: Voxelwise CV averaged over the slice for different Lac signal strengths.

4.3 Lactate signal simulation

4.3.1 Simulation of a constant signal

The constant signal was simulated into the measurement data from Subject 5 in the reference measurements. For every repetition, the same signal was been added into the spectrum and the detectability of the same signal in different spectra was evaluated by analysing the lactate concentration maps over time. The strength of the signal was chosen to be as strong as the signal from tNAA. The position of the lactate resonance at 1.31 ppm is usually covered by lipid signals that cover the entire lactate signal, which is why LCModel could not accurately fit the lactate signal in all voxels in all repetitions. The CV of the lactate signal is consistently low as it can be seen in Fig. 4.17. If the lactate signal can be fitted, then the extracted concentration is relatively constant, with a voxelwise CV that is mostly below 3%. During the processing, L2-regularization was applied to supress these lipid signals, however as it is on the same chemical shift range, the lactate signal can also be affected by this L2-regularization. The CV of slicewise and voxelwise averaged concentrations can be found in Table 4.7 and 4.8 respectively.

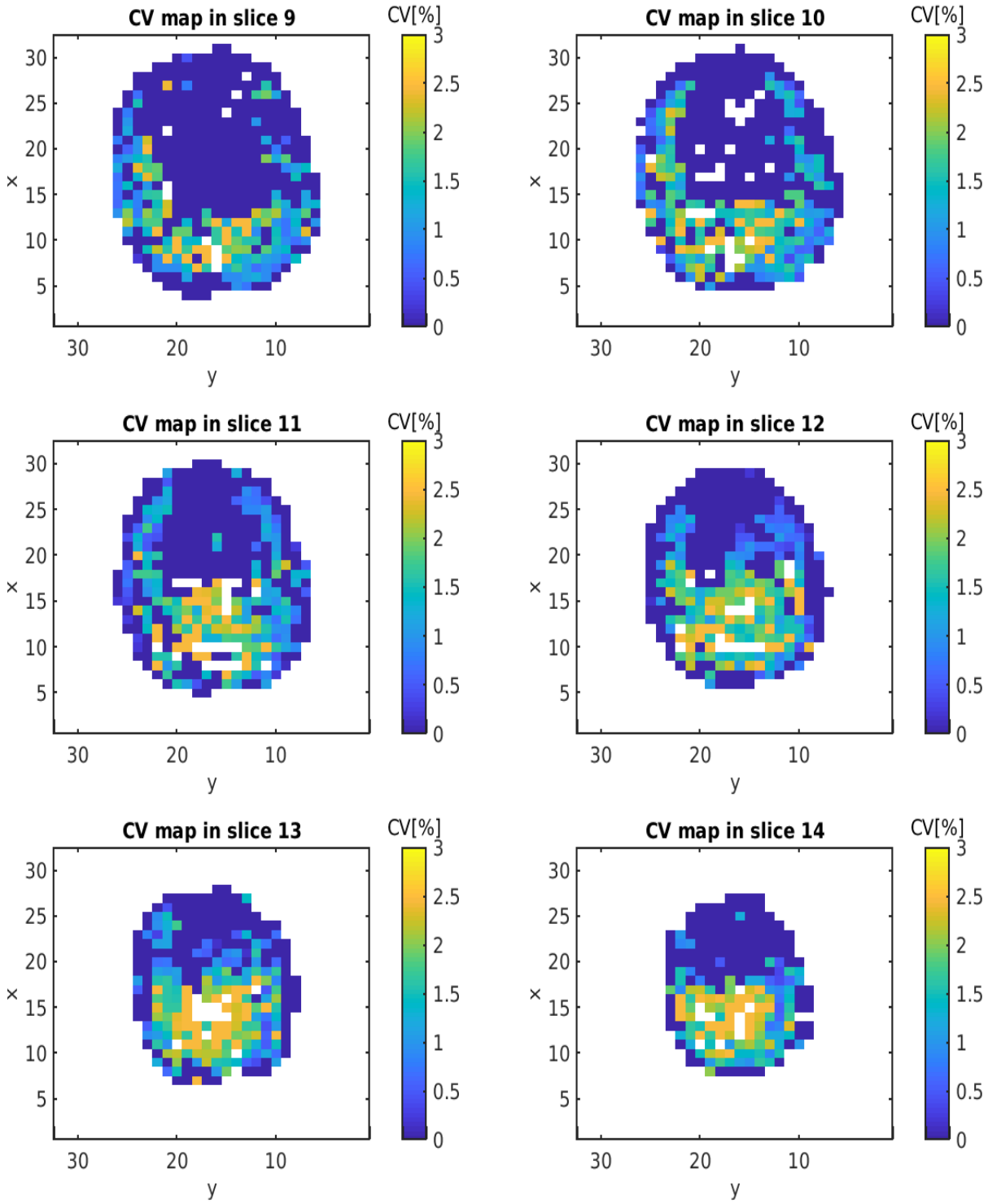

Figure 4.17: CV map of lactate concentrations simulated at twice the strength of the tNAA signal.

4.3.2 Simulation of a decaying signal

To simulate the behaviour of deuterated lactate in the brain, the lactate signal's strength was then simulated with a decreasing strength of 15% for every repetition. The inital strength of the lactate signal was chosen to be at the same level as the signal from tNAA. The lactate signal simulated into the spectrum with different strengths can be seen in Fig. 4.18. The spectra with the Lactate fit at different signal strengths can be seen in Fig. 4.19. The lactate signal was simulated from 100% to 10% of the strength of the constant tNAA signal. The peak of the signal in c) simulated at 10% of the tNAA signal is very small and barely distinguishable from the surrounding noise. Even though LCModel can fit a signal, it has a very high FWHM of 44% and would not be included in the analysis anymore as it is not a reliable signal and would be insufficient for the quality control mask. For lactate signals that are weaker than 10% of the signal strength of tNAA, very few voxels can be used for a reliable fit. As the average tNAA concentration in the brain is at about 10 mM/L, this would correspond to lactate concentrations of around 1 mM/L, which is a normal concentration in a healthy brain. In tumor tissue, lactate concentrations are around 10 mM/L [29] which would correspond to about the same strength as in the fit signal in a) in Fig. 4.19. As the ratio of Glx to Lac is used for imaging of anaerobic respiration in the brain, the contrast would be increased even further, as Lac would have increased concentrations and Glx would have reduced concentrations in tumor tissue.

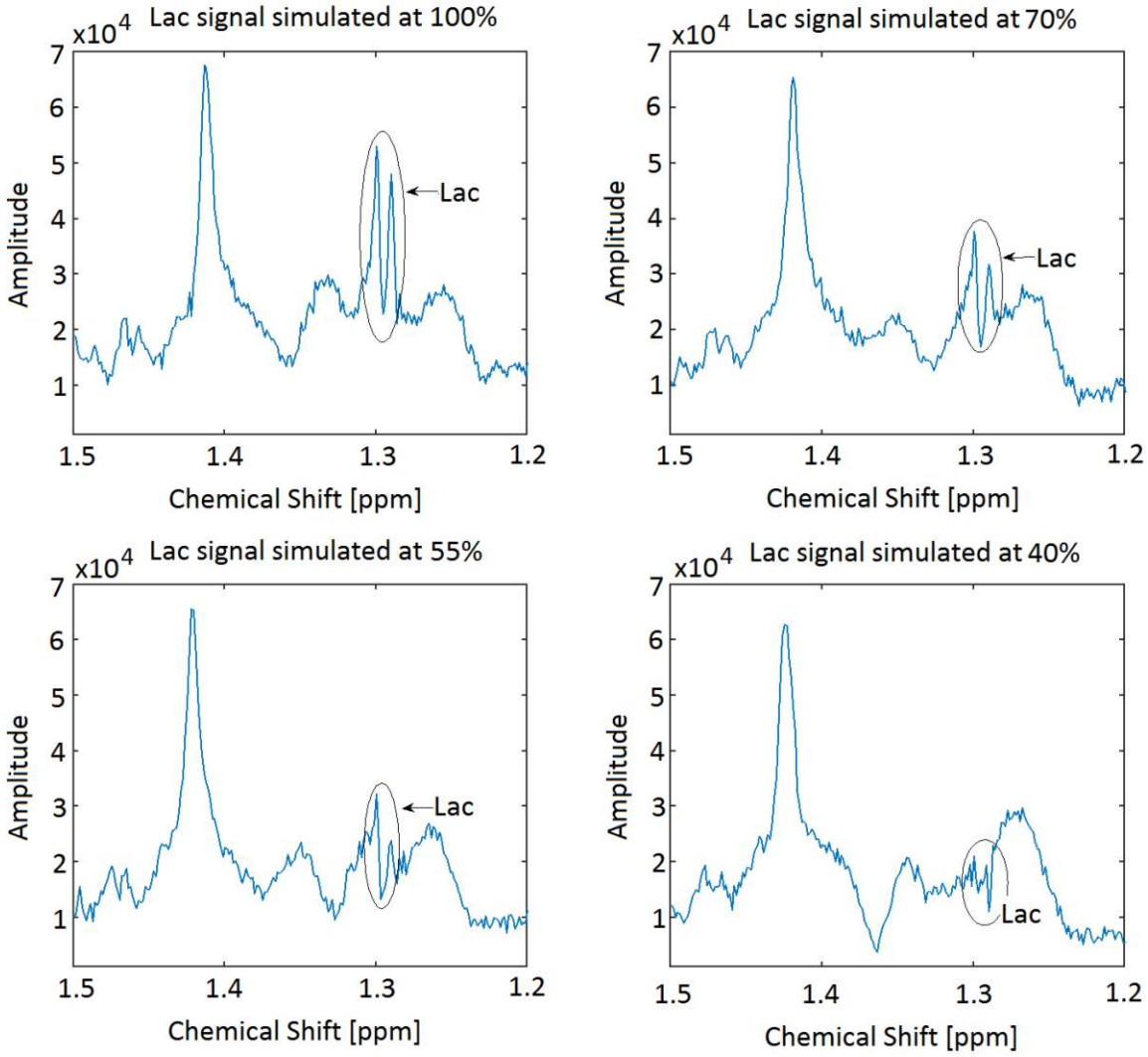

Figure 4.18: Decaying Lactate signal added into the spectra with decreasing intensity corresponding to 100% of the inital tNAA signal down to 40% of the initial tNAA signal strength. The peak at 1.4 ppm originates from a lipid signal.

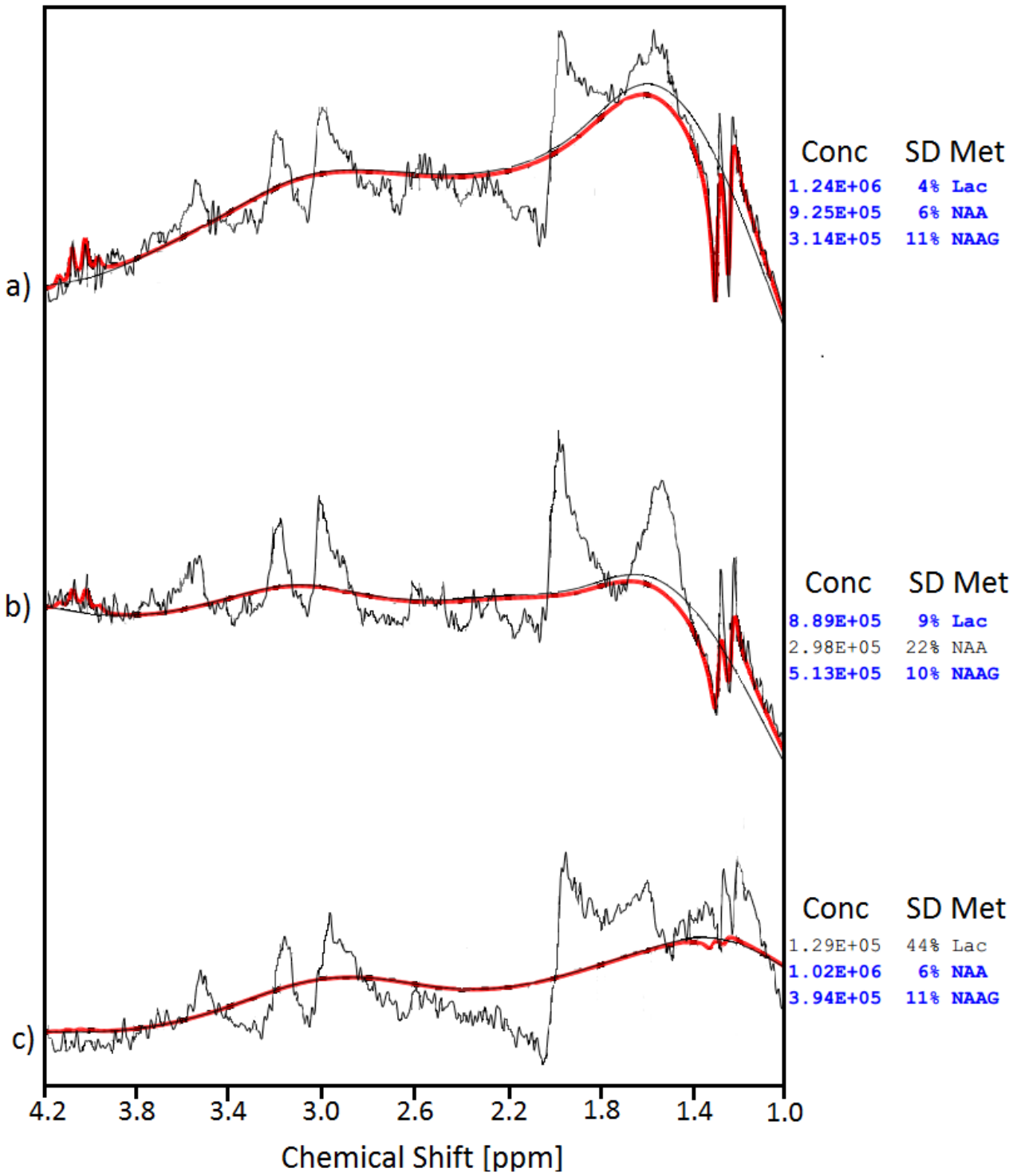

Figure 4.19: Decaying Lactate signal in the fit spectra from 1 ppm to 4.2 ppm with a simulated signal strength corresponding to a) 100% , b) 70% and c) 10% of the tNAA signal. The FWHM of the lactate resonance peak is in a) 4%, b) 9% and c) 44% and the extracted lactate concentration is in a) 1.24×10^6 (100% of tNAA), b) 8.89×10^5 (71% of tNAA) and c) 1.29×10^5 (10% of tNAA).

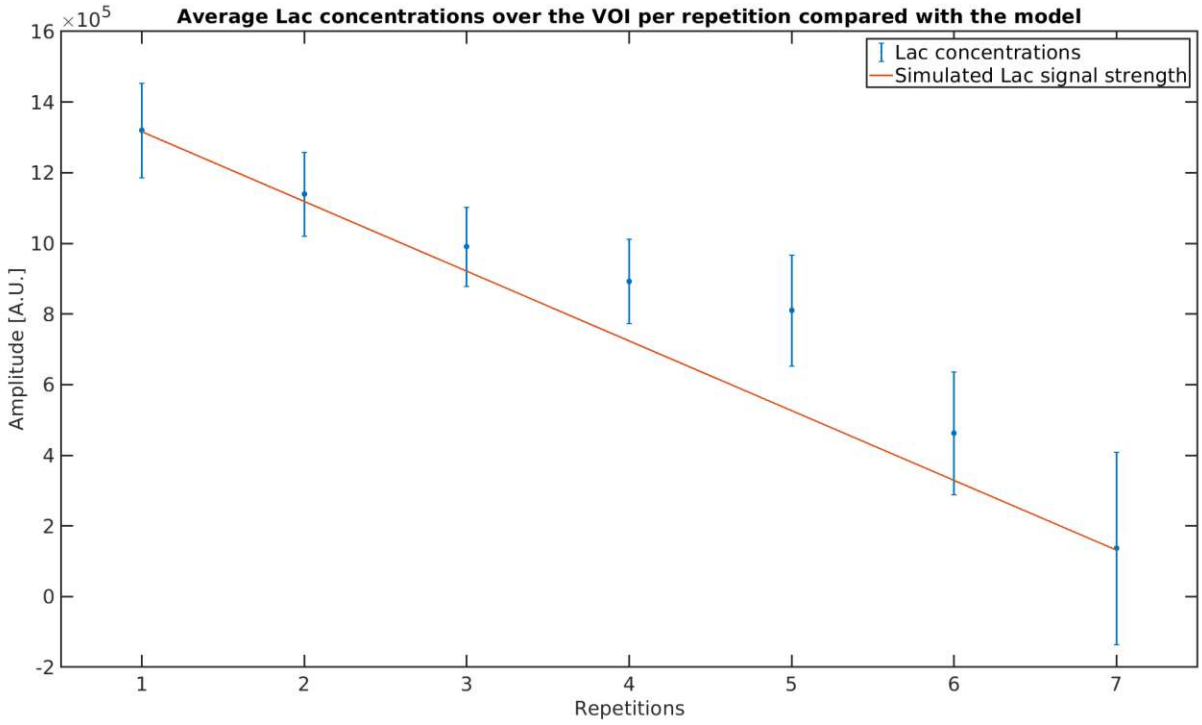

Figure 4.20: Average Lac concentrations in the VOI with decaying simulated Lac signal strength, repetition 1 had a Lac signal strength equal to the tNAA signal while repetition 7 had a Lac signal with a simulated strength of 10% of the tNAA signal.

After having excluded voxels with insufficient SNR and a FWHM, that is too broad, with a quality control mask, the lactate concentrations in the brain were averaged over the VOI and the decay of concentrations with decreasing simulated lactate signal strength for every repetition can be seen in Fig. 4.20. The orange curve represents the modeled decay of 15% per repetition. As it can be seen, the error becomes increasingly large as the concentrations become smaller, which is due to the fact that less voxels have sufficient signal to be fitted by LCModel and thus the fluctuation is higher. The signal simulated after 7 repetitions corresponds to a concentration that is about 10% of the concentration simulated at the beginning or around 1 mM/L. The averaged concentrations as well as the absolute and relative error of the lactate concentrations can be found in Table 4.9.

4.3.3 Improvements through the use of subtraction spectra

Before fitting the metabolites, the spectrum in every voxel for every repetition was subtracted from the spectrum from the initial measurement, such that every spectrum represents the difference compared to the initial state. This reduces the lipid signals significantly and allows the fitting of lactate in more voxels of the brain. The metabolic maps for similarly scaled lactate

Repetition	1	2	3	4	5	6	7
Signal[%]	100	85	70	55	40	25	10
Conc[A.U]	1.32×10^6	1.14×10^6	9.91×10^5	8.93×10^5	8.10×10^5	4.63×10^5	1.37×10^5
Err[A.U]	1.34×10^5	1.19×10^5	1.12×10^5	1.20×10^5	1.57×10^5	1.74×10^5	2.73×10^5
Rel. Err[%]	10.15	10.43	10.30	13.43	19.38	37.58	199.20

Table 4.9: Lac signal strength decaying over 7 repetitions from 100% of the tNAA signal to 10% of the tNAA signal. Variation of the extracted Lac concentrations in arbitrary units (A.U.) along with the error in the same arbitrary unit and the relative error compared to the concentration. Graphically represented in Fig. 4.20.

signals in a central slice of the brain fitted with and without the use of subtraction spectra can be seen in Fig. 4.21. Next to the metabolic map is the corresponding spectrum in a voxel in the represented slice.

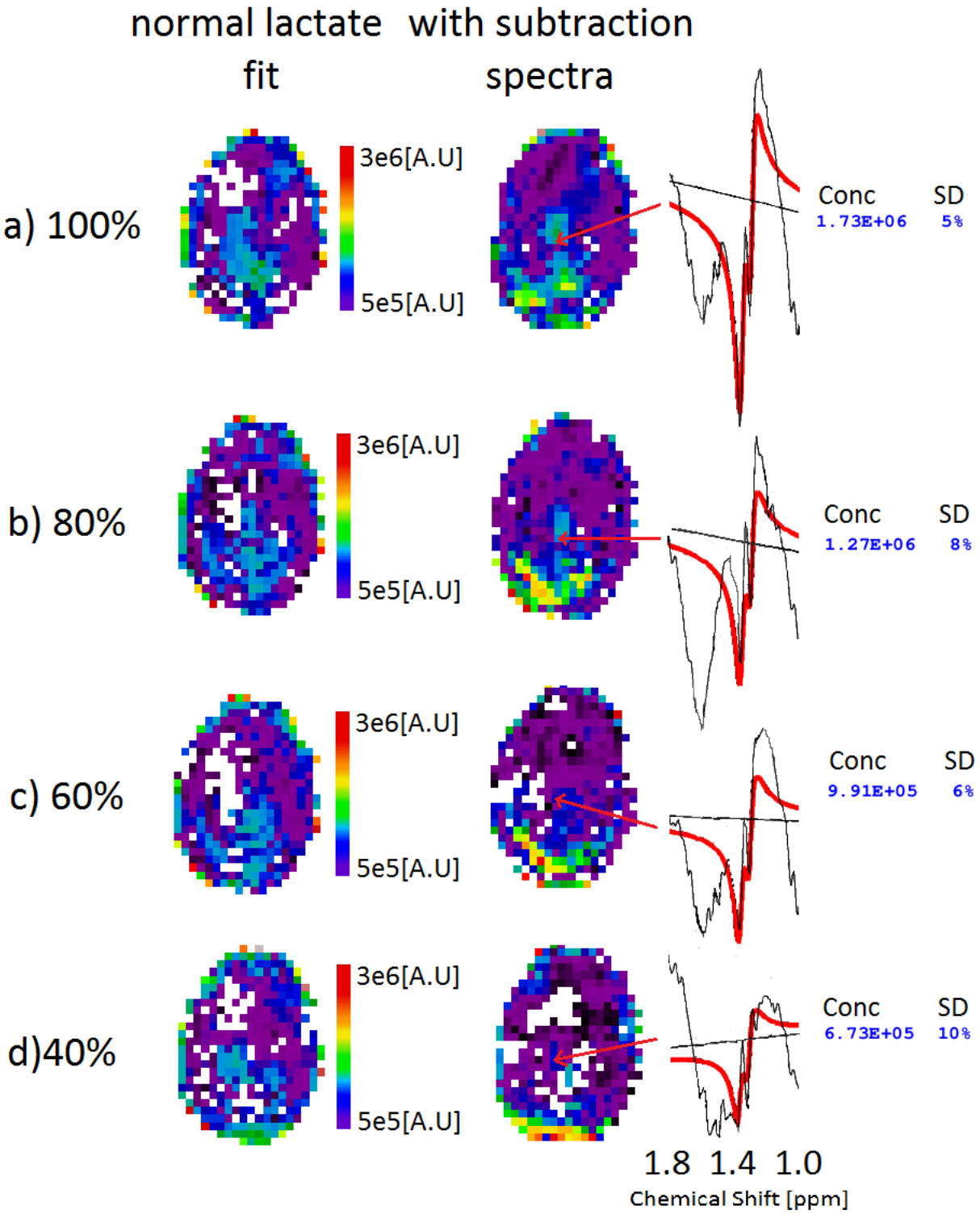

Figure 4.21: Metabolic maps of lactate for differently scaled simulated signal strengths relative to tNAA a) 100%, b) 80%, c) 60% and d) 40% of the tNAA resonance signal obtained through normal fitting on the left and through the use of subtraction spectra on the right. Next to the metabolic maps is a fit spectrum in a central voxel of the represented slice along with the extracted concentration and FWHM of the signal.

Chapter 5

Discussion

In this thesis, a 3D-FID-MRSI sequence was used in a 3T scanner for a dynamic method that is able to quantify and localize glucose uptake and its downstream metabolism in the brain. Metabolites that are part of the glucose metabolism in the brain, e.g. Gln, Glu and Lac were labeled through deuterium nuclei that were metabolized from an orally administered deuterated [6,6'-$^{2}H_2$]-glucose substrate over time. The current gold standard for metabolic imaging used in clinics is FDG-PET, which uses the radiotracer FDG to detect and image anomalies of glucose metabolism in the brain. This method is an alternative to PET that does not require ionizing radiation that can be implemented in regular MR scanners, as it uses standard ^{1}H-MRS. Further, unlike FDG-PET, it can be used to track the metabolism of glucose follow-up products as well.

As ^{2}H nuclei are not detectable by the ^{1}H coil in the MR scanner, passing on of the label to Glx leads to a decrease in Glx signals from the deuterated group (Glx4) over time. The combination of the 3D-FID-MRSI sequence with spatial encoding using CRT can be used to obtain 3D metabolic maps of Glx. In this dynamic setting, the same VOI in the brain was repeatedly measured with the same MRSI sequence in order to detect changes in concentrations of these labeled metabolites over time. Voxelwise comparison of these concentrations for every repeated measurement allowed us to detect a decrease in concentrations with a distinctive difference in GM and WM.

While the overall Glx concentration decay is clearly visible over entire slices, voxelwise decay is more susceptible to local variations and noise. A slight distinction between grey and white matter can be made, as grey matter has an increased metabolic rate of glucose. However with the current spatial resolution, voxelwise coefficients of variation are still high and cannot be used to precisely locate metabolic anomalies. This can be improved by more precise,

real-time motion correction that can be implemented with CRT acquisition patterns. Use of a camera in combination with a tracker placed in the subjects mouth can be used to recreate and compensate movements of the head in real-time and is the subject of current studies at the HFMRC. Further, increasing SNR leads to an improved spatial resolution as metabolic signals will be extracted from the spectrum more reliably. Repeated MRSI scans with assumed constant concentrations of metabolites can be used to improve SNR in 3T. By averaging the noise of multiple repeated MRSI scans, noise can be identified and further supressed, thus increasing the detection sensitivity for metabolites that vary in lower concentrations or that are harder to detect in the spectrum. In particular these are j-coupled metabolites with multiplet resonance signals such as Glutamate, Glutamine or Lactate, which all play an important role in metabolic and neuronal activity in the brain. Additional higher-order shimming as well as dynamic shim updates during the MRSI sequence can further reduce inhomogeneities in the scanner field which will also enhance SNR.

These results are in line with current studies with ^{1}H-MRSI involving deuterium labeled metabolites in 7T MR[3, 21], however 3T scanners are more widely available which increases the potential for further research. In the recently published study [21] a similar method was applied in 7T and they found the decrease in Glu concentrations in WM and GM over 100 minutes to be 15% and 18% respectively. In this study, the decrease of the combined concentrations of Glu and Gln in WM and GM over 60 minutes is 10% and 14% respectively. As there is no apparent slowdown in the decrease of Glx4 concentrations towards the end, it has to be assumed that concentrations would further decrease with more measurements. With field strengths of 7T, labeled Glu can be identified more accurately and with a lower CV in WM and GM [3] and in 3T it is not possible to accurately distinguish Glu from Gln. However, Glu and Gln have different roles in brain metabolism while also being both in the glutamate–glutamine neurotransmitter cycle[1], thus their metabolic behaviour is intertwined. It is unclear whether the difference to the decay of labeled metabolites in 7T studies stems from the individual detection of labeled Glu compared to the detection of Glx. To further understand their individual roles, it is necessary to independently detect the labeling over time of Glu and Gln both in WM and GM, which proves to be difficult in 3T as their signals partially overlap. Nevertheless, it was shown that the changes in Glx4 concentrations are related to the deuterium labeling through deuterated glucose given prior to the measurements, as the decrease in slicewise averaged Glx4 concentrations is clearly above the usual fluctuations in the brain.

Thus the used method can be utilized for quantifying and imaging deuterated metabolite concentrations in vivo with a ^{1}H-MRS in a 3T scanner. This more affordable approach does not

require the expensive radioactive FDG substrate used in PET or a scanner built specifically for ^{2}H-MRS that is used for the direct detection of deuterium nuclei. Instead it can indirectly track deuterated metabolites and can reveal metabolic processes such as the glucose metabolism in the brain by using standard radiofrequency coils and ^{1}H-MRS. Neurotransmitters present in sufficiently high concentrations in the brain can be deuterated and its concentration levels can be mapped over time in a dynamic method, this sequence can be used to identify the metabolic anomalies that go along with most brain disorders such as Alzheimer's disease[2]. Further, since the signal of deuterated nuclei is indirectly picked up in ^{1}H-MRS, all the other non-deuterated metabolites can simultaneously be measured and quantified. The use of ^{1}H-MRS to quantify deuterated metabolites indirectly is difficult because of the strong influence of water and lipid signals that have large resonances in a similar chemical shift range and overshadow most other signals. Thus, these lipid and water signals have to be suppressed in order to reveal the weaker metabolic signals.

5.1 Limitations

The quality of the reference measurements and the obtained stability of the sequence could have been optimized with the vNav sequence that was only used in the measurement sessions with ^{2}H-labeled Glx. This does not allow for a comparison in an undisturbed setting with real-time movement correction and constant concentrations of metabolites. Also an increased number of repetitions of the measurement sequence per session could have quantified the stability more precisely. The number of measurement repetitions in the reference measurement sessions (5 and 7 repetitions) could have been as high as in the measurement session with the ^{2}H compounds (14 repetitions). Then the stability of Glx concentrations in the reference measurements could have been directly compared to the measurements with labeled Glx. The number of subjects was relatively low and even though it was shown that the method works in principle, the statistical analysis of the results is very limited.

5.2 Comparison with DMI and ^{13}C MRS

The indirect detection of ^{2}H using ^{1}H-MRS offers many advantages compared to deuterium metabolic imaging using ^{2}H-MRS. Simultaneously to the indirect detection of deuterated compounds, standard ^{1}H-MRS can still detect all other metabolites present in the brain. No further hardware modifications are necessary for the implementation of the method in a standard ^{1}H MR scanner. DMI uses ^{2}H MRS to detect deuterium nuclei in biological compounds. With a

very low natural abundancy of 0.0115%, ^{2}H signals are very weak in endogenous biological tissue[30]. Unlike with ^{1}H-MRS, where water and fat signals have to be suppressed, it is not necessary in DMI as the proportion of ^{2}H nuclei is very low in water and lipid tissue. Thus the direct detection of ^{2}H compounds in DMI offers a higher contrast compared to the indirect detection method presented in this thesis, as there are no other dominant resonance signals with ^{2}H-MRS that would overlap with the Glx resonance. In most studies using DMI similar results to those in this thesis have been found. The results of the study with a 11.7 T scanner[4] have come to the conclusion that the concentrations of labeled Glx were higher in GM and lower in regions that contain mostly cerebrospinal fluid. Similar to the results of this thesis, a study evaluating DMI in 9.4T[31] has come to the conclusion that Glx is metabolized more rapidly in GM. They also concluded that glucose uptake in GM is initially higher than in WM but decreases faster in GM than in WM. In another study that will be further described in the next paragraph, DMI and hyperpolarized ^{13}C-MRI (^{13}C-HPMRI) was compared in 3T[32], they could not distinguish GM from WM from the results in DMI. This may be because of a relatively low spatial resolution of their MRSI matrix of $10\times10\times10$. Quantitative comparison with other studies is difficult, as DMI as well as the method used in this thesis are relatively new methods and most studies offer more qualitative results.

Another method used for non-invasive imaging of glucose metabolism in the brain is ^{13}C-MRI. This method makes use of the properties of the stable isotope Carbon-13, which, unlike Carbon-12, has a non-zero spin and is thus detectable using NMR. After ingestion of a ^{13}C-labeled compound such as [1-^{13}C]-glucose, the compound is rapidly metabolized in the brain like regular glucose and can be detected either directly using ^{13}C NMR or indirectly using ^{1}H-[^{13}C]-NMR. A comparison of direct and incdirect detection can be found in[33]. Using dynamic nuclear polarization(DNP), the nuclear spins polarization can be increased. This enables a much larger proportion of the spins in bulk matter to be used for imaging, thus increasing the SNR achieved in ^{13}C-MRI. An improved method based on DNP using hyperpolarization is used to further increase the polarization of the ^{13}C-labeled compound[1]. The relaxation times T1 of ^{13}C nuclei are around 1500 ms, making them more interesting for hyperpolarization. This approach is called Hyperpolarized Carbon-13 Magnetic Resonance Spectroscopic Imaging (HP ^{13}C-MRSI) and is mostly used in combination with [1-^{1}3C]pyruvate for imaging of brain metabolism[34]. This compound plays an important role in glycolysis and is thus part of both the lactic acid cycle which yields lactate as an end product and the TCA cycle which is characterized by the metabolism of Glx. Due to the hyperpolarization of the ^{13}C-labeled compound, the ^{13}C-MRI has to be performed immediately after injection of the compound, as the polarization will quickly disappear within minutes after injection[32].

This was done in the recently published study[32] where HP ^{13}C-MRSI with [1-^{1}3C]pyruvate was compared to DMI with [6,6'-2H2]-glucose in 3T. These two methods can be used to investigate different aspects of glucose metabolism. The results of dynamic DMI started one to two hours after ingestion of the glucose substrate and have shown an increase in ^{2}H-Glx concentrations after 12 repeated measurements over an hour up to 3.0 mM/L. Both methods can be used to image the ratio from oxidative to reductive metabolism in the brain, however they are also used to probe alternative metabolic pathways. While the results obtained through DMI favored the oxidative metabolism into ^{2}H-Glx over the reductive metabolism into ^{2}H-Lac, the results from ^{13}C-HPMRI favored the reductive metabolism into ^{13}C-Lac over the oxidative metabolism into ^{13}C-bicarbonate. Overall, they found that with ^{13}C-MRI a higher SNR and higher spatial and spectral resolution could be obtained during the measurements, however the method is limited to a few minutes after injection of [1-^{1}3C]pyruvate as the uptake is significantly quicker than [6,6'-2H2]-glucose uptake. With DMI measurements over an hour they were able to increase the sensitivity of the results compared to ^{13}C-HPMRI. While they were able to identify differences in metabolism between GM and WM with ^{13}C-HPMRI in 3T, they were unable to distinguish metabolism in GM and WM using DMI in 3T. Both ^{13}C-HPMRI and DMI require hardware modifications in the scanner and ^{13}C-HPMRI also requires additional hyperpolarization equipment and pharmacy preperation. Both methods are complementary as they describe different aspects of glucose metabolism.

5.3 Outlook

Research with DMI or ^{1}H MRS using ^{2}H labeled compounds in 3T is still scarce, but the method is a promising alternative to FDG-PET as most studies have shown the potential of deuterium labeled compounds for imaging. With advancements made towards the higher resolution imaging and more stable and more robust data acquisition methods, MRSI has the potential of application in more dynamic methods.

Another application of the MRSI sequence in a dynamic setting is functional MRSI (fMRSI), which is a dynamic method where repeated measurements of the brain can be used to identify neuronal activity in the brain through metabolite concentrations. This method shows potential for clinical use and has been used to investigate activity in the visual cortex with visual stimuli [35] and activity in the motor cortex when subjects were asked to execute different finger tapping movements [36]. Visual stimuli as well as finger tapping has led to an increase

in Glutamate and Lactate concentrations in the respective cortex in the order of magnitude of 10^{-4} mM/L. These studies were made in 7T MR scanners, which inherently have higher SNR and can thus detect smaller variations in metabolite concentrations. Further developments in motion and shim correction methods can lead to a higher voxelwise stability of the method, which is required for a more precise localisation of metabolic behaviour after stimuli. The advancements in localisation, acquisition and noise suppression techniques in ^1H-MRS can be used to further inspect the variations of metabolic behaviour after perceptual, motor, and cognitive tasks especially in patients with psychiatric disorders[37]. Especially as Glu is the major excitatory neurotransmitter, responsible for the stimulation of most of the neurons in the brain[37], a stimulation of a certain region of the brain will cause an increase in Glu concentrations in the area.

Chapter 6

Conclusion

The MRSI sequence developed at the High Field Magnetic Resonance Centre can be used to create high-resolution 3D metabolic maps in the brain. Given the required scanning time of a few minutes and a high spatial and temporal stability, the MRSI sequence fulfills all the requirements for the application in dynamic ^1H-MRS deuterium metabolic imaging in a 3T MR scanner.

At timepoints that are just a few minutes apart, the evolution of concentrations of certain metabolites in a volume in the brain can be quantified by repeatedly scanning the brain with the MRSI sequence. In ^1H-MRS DMI, deuterated glucose is ingested prior to the measurement session and by identifying the decay of concentrations of deuterated metabolites at points in space and in time, we were able to not only locate and quantify glucose uptake but also the metabolic rate of its follow-up products namely Glutamine, Glutamate or Lactate relative to other non-deuterated metabolites.

By using acquisition patterns in concentric ring trajectories to reduce the required scanning time, real time motion correction algorithms to maximize spatial stability as well as through highly optimized reconstruction algorithms that can largely suppress unwanted signals from lipid or water sources and substantially increase SNR. The main drawbacks of the weaker magnetic field in 3T scanners can thus be compensated, proving the potential application of 3D-FID-MRSI for dynamic imaging methods in 3T in future clinical applications.

List of Figures

Bibliography

[1] R. A. d Graaf, *In vivo NMR spectroscopy: principles and techniques*. John Wiley & Sons, 2019. DOI: 10.1002/9781119382461.

[2] C. Liguori, A. Stefani, G. Sancesario, G. Sancesario, M. Marciani, and M. Pierantozzi, "CSF lactate levels, τ proteins, cognitive decline: a dynamic relationship in Alzheimer's disease," *Journal of Neurology, Neurosurgery & Psychiatry*, vol. 86, no. 6, pp. 655–659, 2015. DOI: 10.1136/jnnp-2014-308577.

[3] P. Bednařık *et al.*, "Deuterium labeling enables non-invasive 3D proton MR imaging of glucose and neurotransmitter metabolism in the human brain," *Research Square*, 2022. DOI: 10.21203/rs.3.rs-1027370/v1.

[4] D Feyter, H M and Kevin L. Behar and Zachary A. Corbin and Robert K. Fulbright and Peter B. Brown and Scott McIntyre and Terence W. Nixon and Douglas L. Rothman and Robin A. de Graaf, "Deuterium metabolic imaging (dmi) for mri-based 3d mapping of metabolism in vivo," *Science Advances*, vol. 4, no. 8, 2018. DOI: 10.1126/sciadv.aat7314.

[5] NIST. https://physics.nist.gov/cuu/Constants/index.html.

[6] K. Edler, "Spherical Harmonic Detection Coils and Dynamic Preemphasis," *PhD Thesis*, p. 42, 2010. DOI: 10.13140/RG.2.1.4390.1046.

[7] R. Kreis *et al.*, "Terminology and concepts for the characterization of in vivo MR spectroscopy methods and MR spectra: Background and experts' consensus recommendations," *NMR in Biomedicine*, vol. 34, no. 5, 2021. DOI: 10.1002/nbm.4347.

[8] K. Wright, J. Hamilton, N. Griswold Seiberlich, and V. Gulani, "Non-cartesian parallel imaging reconstruction," *J. Magn. Reson. Imaging*, vol. 1040, pp. 1022–1040, 2014. DOI: 10.1002/jmri.24521.

[9] P. Moser *et al.*, "Intra-session and inter-subject variability of 3D-FID-MRSI using single-echo volumetric EPI navigators at 3T," *Magnetic resonance in medicine*, vol. 83, no. 6, pp. 1920–1929, 2020. DOI: 10.1002/mrm.28076.

[10] J. K. Furuyama, N. E. Wilson, and M. A. Thomas, "Spectroscopic imaging using concentrically circular echo-planar trajectories in vivo," *Magnetic resonance in medicine*, vol. 67, no. 6, pp. 1515–1522, 2012. DOI: 10.1002/mrm.23184.

[11] A. Steel *et al.*, "Metabolite-cycled density-weighted concentric rings k-space trajectory (DW-CRT) enables high-resolution 1H magnetic resonance spectroscopic imaging at 3-Tesla," *Scientific reports*, vol. 8, no. 1, pp. 1–10, 2018. DOI: 10.1038/s41598-018-26096-y.

[12] W. Bogner, R. Otazo, and A. Henning, "Accelerated MR spectroscopic imaging—a review of current and emerging techniques," *NMR in Biomedicine*, vol. 34, no. 5, 2021. DOI: 10.1002/nbm.4314.

[13] A. A. Maudsley *et al.*, "Advanced magnetic resonance spectroscopic neuroimaging: Experts' consensus recommendations," *NMR in Biomedicine*, vol. 34, no. 5, 2021. DOI: 10.1002/nbm.4309.

[14] W. Jiang, M. Lustig, and P. E. Larson, "Concentric rings K-space trajectory for hyperpolarized 13C MR spectroscopic imaging," *Magnetic resonance in medicine*, vol. 75, no. 1, pp. 19–31, 2016. DOI: 10.1002/mrm.25577.

[15] S. Provencher, *LCModel(Version 6.3.1)*. http://s-provencher.com/lcmodel.shtml, 2021.

[16] L. Hingerl *et al.*, "Clinical high-resolution 3D-MR spectroscopic imaging of the human brain at 7 T," *Investigative radiology*, vol. 55, no. 4, pp. 239–248, 2020. DOI: 10.1097/RLI.0000000000000626.

[17] L. J. Rich *et al.*, "1H magnetic resonance spectroscopy of 2H-to-1H exchange quantifies the dynamics of cellular metabolism in vivo," *Nature biomedical engineering*, vol. 4, no. 3, pp. 335–342, 2020. DOI: 10.1038/s41551-019-0499-8.

[18] K. G. d l Cruz-López, L. J. Castro-Muñoz, D. O. Reyes-Hernández, A. Garcıa-Carrancá, and J. Manzo-Merino, "Lactate in the regulation of tumor microenvironment and therapeutic approaches," *Frontiers in oncology*, vol. 9, p. 1143, 2019. DOI: 10.3389/fonc.2019.01143.

[19] W. H. Koppenol, P. L. Bounds, and C. V. Dang, "Otto Warburg's contributions to current concepts of cancer metabolism," *Nature Reviews Cancer*, vol. 11, no. 5, pp. 325–337, 2011. DOI: 10.1038/nrc3038.

[20] Radiologykey.com. https://radiologykey.com/imaging-of-tumour-metabolism-18-fdg-pet.

[21] A. T. Cember *et al.*, "Integrating 1H MRS and deuterium labeled glucose for mapping the dynamics of neural metabolism in humans," *NeuroImage*, vol. 251, no. 118977, 2022. DOI: 10.1016/j.neuroimage.2022.118977.

[22] B. Strasser *et al.*, "Coil combination of multichannel MRSI data at 7 T: MUSICAL," *NMR in Biomedicine*, vol. 26, no. 12, pp. 1796–1805, 2013. DOI: 10.3390/molecules26133896.

[23] R. J. Ogg, R. Kingsley, and J. S. Taylor, "WET, a T1-and B1-insensitive water-suppression method for in vivo localized 1H NMR spectroscopy," *Journal of Magnetic Resonance, Series B*, vol. 104, no. 1, pp. 1–10, 1994. DOI: 10.1006/jmrb.1994.1048.

[24] F. S. Foundation, *Bash*. Boston, MA: Free Software Foundation, 2021.

[25] MATLAB, *Version 9.3 (R2017b)*. Natick, Massachusetts: The MathWorks Inc., 2017.

[26] Y. P. Du, D. L. Parker, W. L. Davis, and G. Cao, "Reduction of partial-volume artifacts with zero-filled interpolation in three-dimensional MR angiography," *Journal of Magnetic Resonance Imaging*, vol. 4, no. 5, pp. 733–741, 1994. DOI: 10.1002/jmri.1880040517.

[27] G. Hangel *et al.*, "Inter-subject stability and regional concentration estimates of 3D-FID-MRSI in the human brain at 7 T," *NMR in Biomedicine*, vol. 34, no. 12, 2021. DOI: 10.1002/nbm.4596.

[28] B. Bilgic, B. Gagoski, T. Kok, and E. Adalsteinsson, "Lipid suppression in CSI with spatial priors and highly undersampled peripheral k-space," *Magnetic resonance in medicine*, vol. 69, no. 6, pp. 1501–1511, 2013. DOI: 10.1002/mrm.24399.

[29] D. M. Brizel *et al.*, "Elevated tumor lactate concentrations predict for an increased risk of metastases in head-and-neck cancer," *International Journal of Radiation Oncology* Biology* Physics*, vol. 51, no. 2, pp. 349–353, 2001. DOI: 10.1016/S0360-3016(01)01630-3.

[30] M. Straathof, A. E. Meerwaldt, H. M. De Feyter, R. A. de Graaf, and R. M. Dijkhuizen, "Deuterium metabolic imaging of the healthy and diseased brain," *Neuroscience*, vol. 474, pp. 94–99, 2021. DOI: 10.1016/j.neuroscience.2021.01.023.

[31] L. Ruhm *et al.*, "Deuterium metabolic imaging in the human brain at 9.4 tesla with high spatial and temporal resolution," *NeuroImage*, vol. 244, no. 118639, 2021. DOI: 10.1016/j.neuroimage.2021.118639.

[32] J. D. Kaggie *et al.*, "Deuterium metabolic imaging and hyperpolarized 13c-mri of the normal human brain at clinical field strength reveals differential cerebral metabolism," *NeuroImage*, vol. 257, no. 119284, 2022. DOI: 10.1016/j.neuroimage.2022.119284.

[33] H. Chen, H. M. De Feyter, P. B. Brown, D. L. Rothman, S. Cai, and R. A. de Graaf, "Comparison of direct 13c and indirect 1h-[13c] mr detection methods for the study of dynamic metabolic turnover in the human brain," *Journal of Magnetic Resonance*, vol. 283, pp. 33–44, 2017. DOI: 10.1016/j.jmr.2017.08.004.

[34] F. Zaccagna *et al.*, "Hyperpolarized carbon-13 magnetic resonance spectroscopic imaging: A clinical tool for studying tumour metabolism," *The British Journal of Radiology*, vol. 91, no. 1085, 2018. DOI: 10.1259/bjr.20170688.

[35] P. Bednařık *et al.*, "Neurochemical and BOLD responses during neuronal activation measured in the human visual cortex at 7 Tesla," *Journal of Cerebral Blood Flow & Metabolism*, vol. 35, no. 4, pp. 601–610, 2015. DOI: 10.1038/jcbfm.2014.233.

[36] B. Schaller, L. Xin, K. O'Brien, A. W. Magill, and R. Gruetter, "Are glutamate and lactate increases ubiquitous to physiological activation? A 1H functional MR spectroscopy study during motor activation in human brain at 7 Tesla," *Neuroimage*, vol. 93, pp. 138–145, 2014. DOI: 10.1016/j.neuroimage.2014.02.016.

[37] J. A. Stanley and N. Raz, "Functional magnetic resonance spectroscopy: the "new" MRS for cognitive neuroscience and psychiatry research," *Frontiers in psychiatry*, vol. 9, p. 76, 2018. DOI: 10.3389/fpsyt.2018.00076.